ABSTRACT

A COMPREHENSIVE STUDY OF EVOLUTION OF PHOTOSPHERIC MAGNETIC FIELD AND FLOWS ASSOCIATED WITH SOLAR ERUPTIONS

by
Shuo Wang

The rapid, irreversible change of the photospheric magnetic field has been recognized as an important element of the solar flare process. Recent theoretical work has shown that such a change would imply Lorentz force perturbations acting on both the outer solar atmosphere and the solar surface. This research uses vector magnetograms obtained with the Helioseismic and Magnetic Imager on board the Solar Dynamics Observatory to study a number of flares, which range from GOES-class C4 to X5 and occur in four active regions. In all the events, a permanent and rapid change of photospheric magnetic field closely associated with the flare occurrence is found. The change is predominantly in the form of an enhancement of the horizontal magnetic field, which is located around the magnetic polarity inversion line between flare ribbons. The area integral of the field change and the derived Lorentz force change both show a strong correlation with flare magnitude. For seven events associated with coronal mass ejections (CMEs), the CME mass is estimated using the observed CME velocity and the impulse provided by the upward Lorentz force. Furthermore, the flow field vorticity of selected sunspots away from flare kernels in the AR 11158 is calculated using the Differential Affine Velocity Estimator. It is found that some spots exhibit a sharp acceleration of rotation co-temporal with the rapid rising of the soft X-ray flux, and that such rotational disturbance may be driven by the Lorentz-force change in the horizontal direction.

A COMPREHENSIVE STUDY OF EVOLUTION OF PHOTOSPHERIC MAGNETIC FIELD AND FLOWS ASSOCIATED WITH SOLAR ERUPTIONS

by
Shuo Wang

A Dissertation
Submitted to the Faculty of
New Jersey Institute of Technology and
Rutgers, The State University of New Jersey – Newark
in Partial Fulfillment of the Requirements for the Degree of
Doctor of Philosophy in Applied Physics

Federated Physics Department

January 2015

APPROVAL PAGE

A COMPREHENSIVE STUDY OF EVOLUTION OF PHOTOSPHERIC MAGNETIC FIELD AND FLOWS ASSOCIATED WITH SOLAR ERUPTIONS

Shuo Wang

Dr. Chang Liu, Dissertation Co-Advisor — Date
Research Professor of Physics, NJIT

Dr. Haimin Wang, Dissertation Co-Advisor — Date
Distinguished Professor of Physics, Director of Space Weather Research Laboratory, Chief Scientist of Big Bear Solar Observatory, NJIT

Dr. Dale E. Gary, Committee Member — Date
Distinguished Professor of Physics, Director of Owens Valley Solar Array, Interim Director of Big Bear Solar Observatory, NJIT

Dr. Martin Schaden, Committee Member — Date
Associate Professor, Director of Graduate Program in Applied Physics, Rutgers University, Newark

---

Dr. Peter W. Schuck, Committee Member — Date
Research Astrophysicist, NASA Goddard Space Flight Center

BIOGRAPHICAL SKETCH

Author: Shuo Wang

Degree: Doctor of Philosophy

Date: January 2015

Undergraduate and Graduate Education:

- Doctor of Philosophy in Applied Physics,
  New Jersey Institute of Technology, Newark, NJ, 2015
- Master of Science in Astrophysics,
  Beijing Normal University, Beijing, China, 2007
- Bachelor of Science in Astronomy,
  Beijing Normal University, Beijing, China, 2004

Major: Applied Physics

Publications:

Wang, Shuo; Liu, Chang; Deng, Na; Wang, Haimin, "Sudden Photospheric Motion and Sunspot Rotation Associated with the X2.2 Flare on 2011 February 15," *The Astrophysical Journal Letters*, 782, L31, 2014.

Wang, Shuo; Liu, Chang; Wang, Haimin, "The Relationship between the Sudden Change of the Lorentz Force and the Magnitude of Associated Flares," *The Astrophysical Journal Letters*, 757, L5, 2012.

Wang, Shuo; Liu, Chang; Liu, Rui; Deng, Na; Liu, Yang; Wang, Haimin, "Response of the Photospheric Magnetic Field to the X2.2 Flare on 2011 February 15," *The Astrophysical Journal Letters*, 745, L17, 2012.

Wang, Shuo; Liu, Chang; Wang, Haimin, "Study of sunspot motion and flow fields associated with solar flares," *The Physics of Sun and Star Spots, Proceedings of the International Astronomical Union, IAU Symposium,* 273, 412, 2011.

Su, Jiangtao; Jing, Ju; Wang, Shuo; Wiegelmann, Thomas; Wang, Haimin, "Statistical Study of Free Magnetic Energy and Flare Productivity of Solar Active Regions," *The Astrophysical Journal*, 788, 150 , 2014.

Xu, Yan; Jing, Ju; Wang, Shuo; Wang, Haimin, "Comparison of Emission Properties of Two Homologous Flares in AR 11283," *The Astrophysical Journal*, 787, 7, 2014.

Ruan, Guiping; Chen, Yao; Wang, Shuo; Zhang, Hongqi; Li, Gang; Jing, Ju; Su, Jiangtao; Li, Xing; Xu, Haiqing; Du, Guohui; Wang, Haimin, "A Solar Eruption Driven by Rapid Sunspot Rotation," *The Astrophysical Journal*, 784, 165, 2014.

Jing, Ju; Liu, Chang; Lee, Jeongwoo; Wang, Shuo; Wiegelmann, Thomas; Xu, Yan; Wang, Haimin, "Evolution of a Magnetic Flux Rope and its Overlying Arcade Based on Nonlinear Force-free Field Extrapolations," *The Astrophysical Journal Letters*, 784, L13, 2014.

Wang, Haimin; Liu, Chang; Wang, Shuo; Deng, Na; Xu, Yan; Jing, Ju; Cao, Wenda, "Study of Rapid Formation of a delta Sunspot Associated with the 2012 July 2 C7.4 Flare Using High-resolution Observations of the New Solar Telescope," *The Astrophysical Journal Letters*, 774, L24, 2013.

Liu, Chang; Deng, Na; Liu, Rui; Lee, Jeongwoo; Wiegelmann, Thomas; Jing, Ju; Xu, Yan; Wang, Shuo; Wang, Haimin, "Rapid Changes of Photospheric Magnetic Field after Tether-cutting Reconnection and Magnetic Implosion," *The Astrophysical Journal Letters*, 745, L4, 2012.

Liu, Chang; Deng, Na; Liu, Rui; Ugarte-Urra, Ignacio; Wang, Shuo; Wang, Haimin, "A Standard-to-blowout Jet," *The Astrophysical Journal Letters*, 735, L18, 2011.

Liu, Rui; Liu, Chang; Wang, Shuo; Deng, Na; Wang, Haimin, "Sigmoid-to-flux-rope Transition Leading to a Loop-like Coronal Mass Ejection," *The Astrophysical Journal Letters*, 725, L84, 2010.

Presentations:

Wang, Shuo; Liu, Chang; Deng, Na; Liu, Rui; Liu, Yang; Wang, Haimin, "A Comprehensive Study of the Photospheric Magnetic Field Change Associated with Solar Flares," *Dissertation Talk*, American Astronomical Society Solar Physics Division meeting 44, Bozeman, Montana, 2013.

Wang, Shuo; Liu, Chang; Wang, Haimin, "The Photospheric Magnetic Field Change Associated with Solar Flares," *Oral Presentation*, Space Weather Summer School, University of Alabama in Huntsville, Huntsville, Alabama, 2013.

Wang, Shuo; Jing, Ju; Wang, Haimin, "Daily Solar Flares Forecasting at NJIT," *Invited Talk*, the Second Flare-Forecasting Comparison Workshop, NorthWest Research Associates, Inc./CoRA, Boulder, Colorado, 2013.

Wang, Shuo; Liu, Chang; Deng, Na; Wang, Haimin, "Sharp Acceleration of Sunspot Rotation Associated with Flares in NOAA AR 11158," Living With a Star / Solar Dynamics Observatory 2013 Science Workshop, Cambridge, Maryland, 2013.

Wang, Shuo; Liu, Chang; Liu, Rui; Deng, Na; Liu, Yang; Wang, Haimin, "Irreversible Change of Photospheric Magnetic Field: Evidence for Back Reaction of Coronal Field Restructuring," American Astronomical Society meeting 220, Anchorage, Alaska, 2012.

Wang, Shuo; Liu, Chang; Wang, Haimin, "Study of Sunspot Motion and Flow Fields Associated with the 2006 December 13 X3.4 Flare," American Astronomical Society Solar Physics Division meeting 216, Miami, Florida, 2010.

Liu, Chang; Deng, Na; Liu, Rui; Ugarte-Urra, Ignacio; Wang, Shuo; Wang, Haimin, "A Standard-to-blowout Jet," American Astronomical Society, Solar Physics Division meeting 42, Las Cruces, New Mexico, 2011.

To my family

ACKNOWLEDGMENT

First and foremost, I would like to express my special appreciation and thanks to my co-advisor Dr. Haimin Wang for his great mentoring and brilliant research ideas. He supervised my research, provided insightful feedback and direction, and helped me assemble a fantastic dissertation committee. He also provided me generous financial support, so that I can focus on my research. I consider it an honor to be his Ph.D. student.

My sincere gratitude also goes to my co-advisor Dr. Chang Liu. This thesis would not have been possible without his tremendous time and effort. He was always available to render help and support.

It is with immense gratitude that I acknowledge the support and help of Dr. Dale Gary, Dr. Martin Schaden, and Dr. Peter Schuck, for taking time to be my thesis committee members.

I am deeply indebted to the professors and doctors in the solar group: Drs. Na Deng, Ju Jing, Rui Liu, Yan Xu, Wenda Cao, Zhiwei Liu, Jeongwoo Lee, Gregory Fleishman, Gelu Nita, Bin Chen, Jiangtao Su, Guiping Ruan, Yujiang Dou, Changyi Tan, Sung-Hong Park, Yuan Yuan, Yixuan Li, Samuel Tun, and Kyung-guk Min. I enjoyed working with them and learned a lot from them in these years. They helped me not only in my research but also in my personal life. Thanks to my classmates in the solar group: Xin Chen, Zhicheng Zeng, Zhitao Wang, Xiupeng Wang, Shaheda Begum Shaik, Netsuha Kuroda, Dandan Ye, Qi Hao, and Xu Yang. Also to all my friends and colleagues at NJIT.

I wish to thank all the rest of the academic and support staff of the Center for Solar-Terrestrial Research and New Jersey Institute of Technology for providing resources and support. Special thanks to Ms. Christine Oertel and Ms. Cheryl James, the administrative assistants in our center, for assisting me in many ways.

It gives me great pleasure in acknowledging the following organizations for their financial supports: the Solar Physics Division of the American Astronomical Society for traveling funds to attend the 2012 annual conference and the SDO 2013 Science Workshop; the National Science Foundation and the Center for Space Plasma and Aeronomic Research at the University of Alabama in Huntsville for the stipend supporting my travel to the 2013 Space Weather Summer School; the NorthWest Research Associates, Inc. for traveling funds to attend the second flare-forecasting comparison workshop.

Words cannot express how grateful I am to my parents for all of the sacrifices that they have made on my behalf. I would also like to thank all of my friends who supported me to strive towards my goal.

This dissertation was supported by NSF grants AGS 0745744, AGS 0819662, AGS 0839216, AGS 0849453, and AGS 0936665, and by NASA grants NNX08AQ90G, NNX08AJ23G, NNX11AC05G, NNX13AF76G, and NNX13AG13G.

TABLE OF CONTENTS

TABLE OF CONTENTS
(Continued)

Chapter **Page**

LIST OF TABLES

LIST OF FIGURES

Figure **Page**

LIST OF FIGURES
(Continued)

Figure **Page**

LIST OF FIGURES
(Continued)

Figure **Page**

LIST OF FIGURES
(Continued)

Figure **Page**

LIST OF FIGURES
(Continued)

Figure **Page**

LIST OF FIGURES
(Continued)

Figure **Page**

CHAPTER 1

INTRODUCTION

1.1 Living with the Sun

The Sun is the closest star to the Earth. As the center of the solar system, it provides energy to all its planets including the Earth. The solar radiation at the Earth is 1.36 kW m^{-2}, large enough to power everything moving on the Earth. The energy supply from the Sun together with the material on the Earth provide a life-friendly environment for us, the humankind.

1.2 Properties of the Sun

There are over 1.7×10^{11} galaxies in the observable universe. The Sun lies in the Milky Way galaxy which includes $\sim 4 \times 10^{11}$ stars. The Milky Way galaxy is a barred spiral galaxy with the diameter of $\sim 10^5$ light-years. The Sun is located at the Orion-Cygnus Arm, and is $\sim 2.7 \times 10^4$ light-years away from the Galactic Center.

The Hertzprung-Russell diagram shows the relationship between stars' luminosities and spectral types. Most of the stars including the Sun are in the region of the diagonal line of the diagram, and the set of these stars are called the main sequence. The Sun is a G-type main-sequence star based on Harvard spectral classification.

The chemical composition at the photosphere of the Sun can be measured from spectroscopy. The abundance of hydrogen and helium are 74.9% and 23.8% in mass, respectively (Lodders 2003). The remaining 1.3% are heavier elements such as oxygen, carbon, neon, and iron. The hydrogen and helium were formed by Big Bang nucleosynthesis. The metals were produced by stars with larger mass than the Sun before the formation of the Sun.

The Sun-Earth distance can be derived by measuring the distances between the inner planets and Earth with radar. The mean distance from the Earth to the Sun is

1.5×10^8 km. Hence, 1 arcsec on the solar surface is 725 km. The solar mass can be derived by using Newton's law of universal gravitation. It is 2×10^{30} kg.

Emilio et al. (2012) analyzed the SOHO/MDI observation of transits of Mercury to measure the size of the Sun, and they found that the radius of the Sun is 960.1 arcsec, i.e. 6.963×10^5 km.

The effective temperature on the photosphere of the Sun is ~ 5778 K. From the solar irradiance measured by satellites (1.36 kW/m^2), the luminosity of the Sun can then be determined as $\sim 4 \times 10^{26}$ W.

1.3 Evolution of the Sun

The Sun formed from a gravitational collapse of a molecular cloud about 4.6×10^9 years ago (Bonanno et al. 2002). The gravitational condensation increased the pressure and temperature in the core of the Sun, and the hydrogen began to fuse into helium. The energy released from the fusion countered gravitational condensation, and the Sun reached hydrostatic equilibrium. The Sun then reached the G2V position on the Hertzprung-Russell diagram and stayed there until now.

The Sun will stay in its main-sequence stage a total duration of about 10^{10} years, with volume and luminosity slowly increasing (Ribas et al. 2010). The hydrogen in the core is exhausted by this time, and there is a burning hydrogen shell on the edge of the core. The helium core contracts while the burning hydrogen shell expands. The Sun then becomes a red giant. The helium core contraction causes density and temperature to increase, and this can initiate a helium flash. After the flash, the fusion occurs both in the helium core and in the hydrogen shell. When the helium in the core is exhausted, a burning helium shell starts. At this time, there are two concentric burning shells, and the Sun is in its asymptotic giant branch phase. In this phase, the energy released by helium fusion can cause heavy mass ejection, and the mass blown away from the shell can reach 10^{-5} solar mass per year. The fusion

products of helium are carbon and oxygen. The mass of the Sun is not large enough to start carbon fusion, and the two shells disappear when they reach the solar surface. The Sun then reaches its final phase as a fading white dwarf with a composition of carbon and oxygen.

1.4 Structure of the Sun

The Sun is a hot plasma sphere. The surface of the Sun is observable by naked eye, and is called the photosphere. The region below the surface is called the solar interior, while that above the surface is called the solar atmosphere.

1.4.1 Solar Interior

The solar interior is opaque to not only visible light but electromagnetic radiation at all wavelengths. One way to analyze the solar interior is through helioseismology, which is the study of pressure waves passing through the solar interior. Dopplergrams from satellite and ground-based observations are maps of velocity on the photosphere, and contain the wave information used for helioseismology.

The core of the Sun is the part within 0.25 solar radius of the center. It has higher temperature ($\sim 1.6 \times 10^7$K) and higher density (160 g cm^{-3}) compared to other layers of the Sun. Also, it is where nuclear fusion occurs on the Sun. There are two types of fusion. The proton-proton chain reaction accounts for 99% of the solar power and the carbon-nitrogen-oxygen cycle contributes the remaining 1%. Since the Sun is releasing $\sim 4 \times 10^{26}$ W of power, the mass loss in fusion conversion is $\sim 4 \times 10^9$ kg per second. The helium produced by thermonuclear fusion remains with the Sun, while the high-energy gamma rays and neutrinos escape from the Sun. Neutrinos leave the Sun directly without interactions, but, the gamma rays take a long path to get away. Along the random walk path that results from scattering, the energy of the photons decrease. It takes $\sim 10^5$ years for them to reach the solar surface

as mainly visible light. Measurements of solar neutrinos carried out by underground experiments verified the standard solar model (Ahmad et al. 2001).

The radiation zone of the Sun is the layer between 0.25 and 0.7 solar radius. The energy generated in the core is transported outside by radiation in this layer.

The convection zone of the Sun is the layer between the radiation zone and the solar surface. The energy transportation in this layer is dominated by convection according to the Schwarzschild criterion.

The region of transition between the radiation zone and convection zone is called the tachocline. Below the tachocline, the radiation zone and the core rotate together as a rigid body. In contrast, differential rotation is observed in the convection zone.

1.4.2 Solar Atmosphere

The solar photosphere is the visible surface of the Sun with an optical depth of $\frac{2}{3}$. Photons in this layer can escape from the Sun with an average scatter rate less than one. The effective temperature of the photosphere is 5800 K based on the Stefan-Boltzmann law. The density is 0.2 g m^{-3}.

The white-light image of the Sun shows that the photosphere is composed of millions of granules with a diameter of 1–3″. As a result of convection orignating from the interior of the Sun, the central part of granules is bright and has upward movement and high temperature, while the edge is darker and has downward movement and lower temperature. The lifetime of granules is 10–20 minutes.

The bright areas in the edge of granules are called faculae. They are formed due to the concentration of magnetic field and have a higher temperature than their surroundings. Solar faculae are more easily seen close to the limb of the solar disk, as the limb is darker than the central part.

The Doppler map of photosphere shows supergranules with a size over 30″. Supergranules have a mean lifetime of 24 hours. Magnetic field is concentrated on the

edges of the cells to form the supergranular network. The supergranulation pattern is also shown in flow maps derived from a sequence of white-light images.

Sunspots are dark spots appearing on the photosphere. A sunspot is usually composed of a central dark part called the umbra and a surrounding lighter part named the penumbra. The temperature of a typical sunspot is 3800 K, while the temperature of its surrounding is at the photospheric temperature of around 5800 K. The size of sunspots ranges from $0''.02$ to $200''$, and the lifetime is several days to weeks. Sunspots are actually depressions on the photosphere, thus penumbrae look different at different positions of the solar disk due to the Wilson effect. Sunspots are usually in pairs, with the two opposite magnetic polarities containing the same amount of magnetic flux. In each pair, the leading sunspot tends to be closer to the solar equator than the following sunspot, and the angle between the axis linking them and the equator is larger at higher latitude as stated by Joy's law (Hale et al. 1919).

The chromosphere, known as the lower atmosphere of the Sun, is the layer above the photosphere with a height of 2000 km. It emits less light than the photosphere due to its lower density. Thus, it cannot be seen by naked eye except during a total eclipse.

The corona is the upper atmosphere of the Sun. The white-light corona can be seen during the total eclipse. The temperature of this layer is more than 10^6 K. Due to this high temperature, there are emission lines from the highly ionized heavy elements, and the corona is bright in X-rays as well.

1.5 Solar Activities

A solar flare is a sudden energy release that takes place in the atmosphere of the Sun and is often seen as a brightening in multiple wavelengths. It can be classified based on its soft X-ray flux as shown in Table 1.1.

Table 1.1 GOES Soft X-ray Flux Classification of Flares

Classification	GOES Peak Flux at 1–8 Å (W m^{-2})
A	10^{-8} – 10^{-7}
B	10^{-7} – 10^{-6}
C	10^{-6} – 10^{-5}
M	10^{-5} – 10^{-4}
X	$> 10^{-4}$

A coronal mass ejection (CME) is a huge ejection of mass, together with magnetic flux from the corona into space. The average mass ejected is 10^{12} kg, with an average speed of 500 km s^{-1}. CMEs often accompany major solar flares, although not always.

There is an increasing need to understand the impulsive energy release associated with solar flares and CMEs, as human activities are nowadays more and more affected by space weather. Solar eruptions are generally believed to be the consequence of magnetic reconnection occurring in the solar corona (Kopp & Pneuman 1976; Antiochos et al. 1999). However, despite the frequent coincidence of the CME launch, flare emissions (e.g., in white-light and hard X-rays), and sunquakes in the solar interior, the transport of energy and momentum into the interior from the solar atmosphere is far from fully understood.

Several models were proposed to explain CMEs and solar flares. One dominant model focusing on the initiation of a CME is the breakout model introduced by Antiochos et al. (1999). As shown in Figure 1.1, the model involves a multipolar flux system. The preflare state is shown in Figure 1.1(a). There are four flux concentrated regions in the photosphere with opposite polarities to its neighbors. Above the filament (black circle in Figure 2.1(a)), two bundles of magnetic field line in opposite directions are close to each other. According to the breakout model, an initial reconnection occurring at this position triggers the CME. Lynch et al. (2004) showed their result of a high-resolution MHD simulation, and they stated that the simulated evolution of the post-flare loop and ribbons in the chromosphere, under the condition of slow reconnection (i.e., a long-duration flare), agrees with the model.

An alternate model is the tether-cutting model (Moore et al. 2001), which is a bipolar flux system with a sigmoid (S-shaped) configuration on the photosphere. The model is proposed based on observations, and is now backed with many cases of observational evidence such as described in Chapters 2 and 3. The model is illustrated

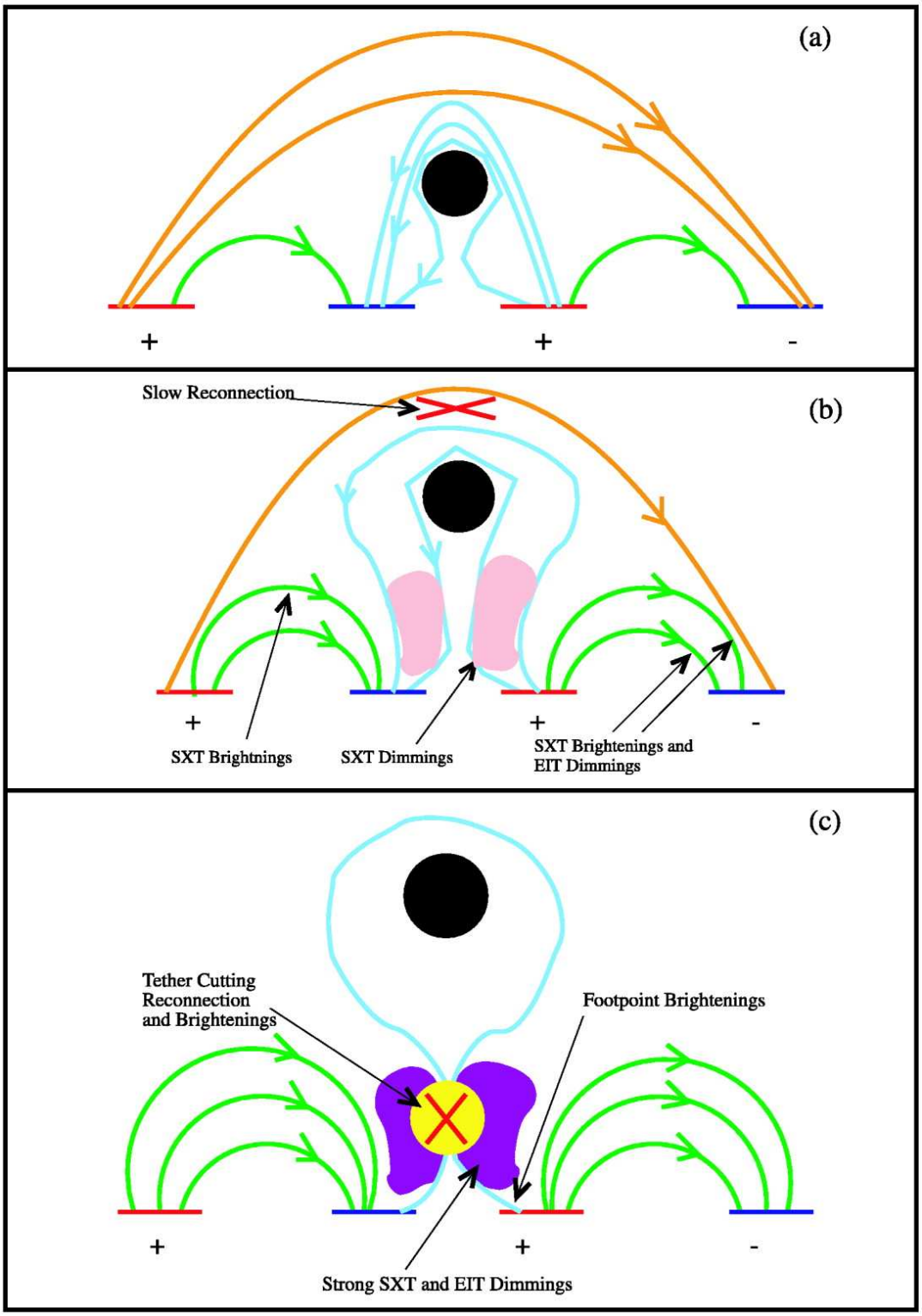

Figure 1.1 Two-dimensional schematic of the breakout model. (a)The initial state of the quadrupolar system before flare. (b)During the slow upward movement of the filament, the magnetic field lines in opposite directions above the filament interact via breakout reconnection. (c) After enough of the reconnection, the confinement above the filament is removed, and the filament explodes out as a CME.
Source: Sterling & Moore (2004).

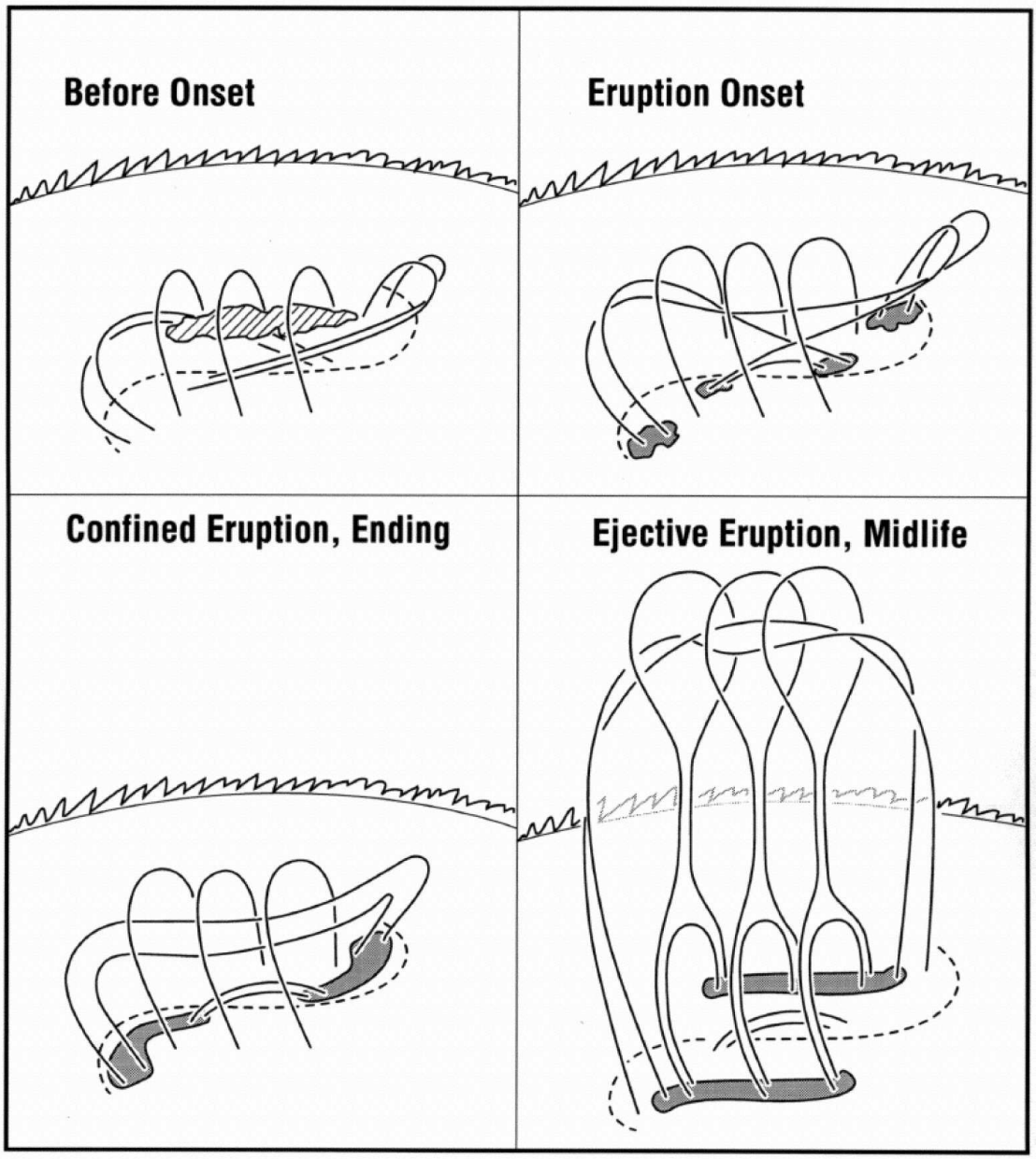

Figure 1.2 Three-dimensional schematic of the tether-cutting model. The explosion is triggered by tether-cutting reconnection below the filament which is shown as diagonally lined feature in the upper left panel. The dashed curve is the polarity inversion line of the Active Region in the photosphere. The solar limb is drawn as ragged arc. The gray areas are ribbons or bright patches at the feet of the reconnected magnetic field lines.
Source: Moore et al. (2001).

in Figure 1.2. The initial state in the upper left panel of Figure 1.2 shows a strong shear under the filament and above the polarity inversion line. The tether-cutting reconnection in this region can trigger a flare(upper right panel of Figure 1.2). The newly formed upper arcade moves up, and may or may not succeed in escaping the sun as a CME (lower panels of Figure 1.2).

It has been known that the long-term evolution of photospheric magnetic field, driven by new flux emergence and surface flows, plays an important role in building up free energy in the corona, and that this free magnetic energy powers flares and CMEs (Priest & Forbes 2002). On the other hand, a short-term variation of the photospheric magnetic field associated with flares has been neglected because photospheric magnetic fields are strongly line-tied to the dense high-β photosphere and thus were thought unlikely to be altered by any flare-related disturbances created in the tenuous low-β corona. Only recently, a back reaction of the coronal magnetic field on the photosphere during the reconfiguration of the coronal magnetic field has been seriously considered from the theoretical point of view. The idea is that the coronal magnetic field should contract inward, as the magnetic energy of the coronal magnetic field decreases after flares and/or CMEs (called "implosion"; Hudson 2000). This may cause the photospheric magnetic field to be oriented more horizontally, resulting in a Lorentz force acting downward on the solar surface (Figure 1.3; Hudson et al. 2008), which is related to a magnetic "McClymont jerk" (McClymont & Fisher 1989; Anwar et al. 1993).

Most recently, Fisher et al. (2012) generalized the work of Hudson et al. (2008) to derive expressions for the Lorentz-force changes in both the vertical and horizontal directions, which are implied by observed changes in photospheric vector magnetic fields that occur over the course of large, eruptive flares. The authors showed that the observed, more horizontal state of the photospheric magnetic field after flares points to an upward Lorentz-force change exerted on the outer solar atmosphere,

which is balanced exactly by an equal and opposite Lorentz-force change acting on the photosphere and the solar interior, as argued by Hudson et al. (2008). The Lorentz force is

$$\mathbf{f}_{\mathrm{L}} = \mathbf{J} \times \mathbf{B}, \tag{1.1}$$

where the current J is given by

$$\mathbf{J} = \bigtriangledown \times \mathbf{B}. \tag{1.2}$$

The expression of the Lorentz force can be rewritten as the following:

$$\mathbf{f}_{\mathrm{L}} = \bigtriangledown \cdot \mathbf{T} = \frac{\partial T_{\mathrm{ij}}}{\partial x_{\mathrm{j}}}, \tag{1.3}$$

where T is the Maxwell stress tensor, and can be written as

$$T_{\mathrm{ij}} = \frac{1}{8\pi}(2B_{\mathrm{i}}B_{\mathrm{j}} - B^2\delta_{\mathrm{ij}}). \tag{1.4}$$

The vertical and horizontal components of the change of the volume-integrated downward Lorentz-force can be quantified as

$$\delta F_{\mathrm{r,interior}} = \frac{1}{8\pi}\int_{\mathrm{A_{ph}}} dA(\delta B_{\mathrm{r}}^2 - \delta B_{\mathrm{h}}^2)\ , \tag{1.5}$$

and

$$\delta \mathbf{F}_{\mathrm{h,interior}} = \frac{1}{4\pi}\int_{\mathrm{A_{ph}}} dA\delta(B_{\mathrm{r}}\mathbf{B}_{\mathrm{h}})\ , \tag{1.6}$$

where A_{ph} is the photospheric region where the changes of the vector field are measured, and B_{r} and $\mathbf{B}_{\mathrm{h}}$ are the radial and horizontal components of $\mathbf{B}$. The authors asserted that the integration of the upward Lorentz-force change over its

change period should produce an upward impulse driving the erupting CMEs, and that the conservation of momentum predicts an equal, but downward-moving impulse applying onto the solar interior, which could be a possible source of acoustic emission of sunquakes as revealed by helioseismic techniques in some flares. Therefore, an observational relationship was suggested to exist among the Lorentz-force change computed from variations in photospheric vector magnetograms, the outward momentum of eruptive CMEs, and the downward momentum in the solar interior possibly reflected in the properties of helioseismic disturbances.

On the observation side, rapid and permanent changes of vector magnetic fields associated with flares were discovered two decades ago (Wang 1992; Wang et al. 1994). Specifically, the transverse field near the flaring magnetic polarity inversion line (PIL) is found to become enhanced substantially and irreversibly over the time duration of the flare, which is also often accompanied by an increase of magnetic shear. A similar trend indicating a more horizontal orientation of the photospheric magnetic field after flares and CMEs has continued to be observed later on in many observations (Wang et al. 2002, 2004b, 2005; Liu et al. 2005; Wang et al. 2007; Jing et al. 2008; Li et al. 2009; Liu et al. 2011), and shows some agreement with recent MHD modeling (Li et al. 2011). Nevertheless, a majority of such studies are unavoidably hampered by the obvious limitations, ground-based observations (e.g., seeing variation and the limited number of spectral positions in the observed magnetic-sensitive line), probably because of which mixed results were also reported (Ambastha et al. 1993; Hagyard et al. 1999; Chen et al. 1994; Li et al. 2000a,b).

On the other hand, flare-related variations in the line-of-sight (LOS) component of photospheric magnetic field have been clearly recognized (e.g., Wang et al. 2002; Spirock et al. 2002; Yurchyshyn et al. 2004; Sudol & Harvey 2005; Wang 2006; Wang & Liu 2010; Petrie & Sudol 2010). In particular, the feature of unbalanced flux evolution of opposite polarities could provide indirect evidence for the more horizontal

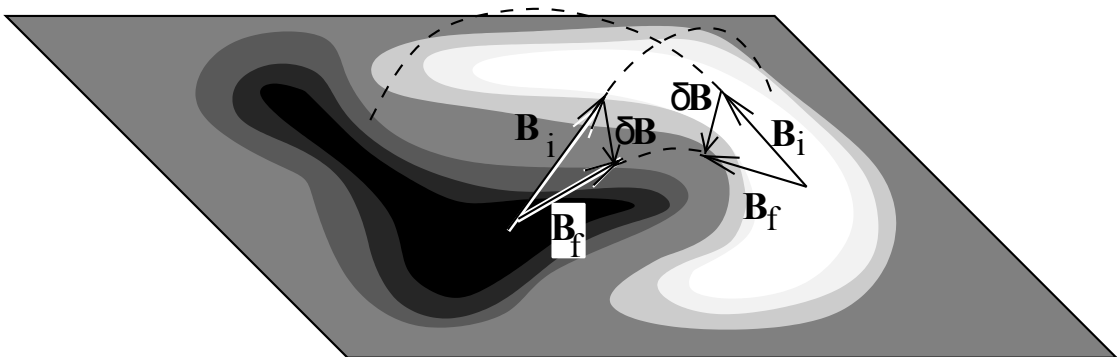

Figure 1.3 The schematic of how the initial photospheric magnetic field vectors B_i, is tilted by δB due to coronal restructuring during a solar eruption such as a flare/CME. The coronal field is shown as dashed lines. The final photospheric magnetic field vectors B_f are inclined to be more horizontal.
Source: Hudson et al. (2008).

orientation of photospheric fields after flares/CMEs (Wang & Liu 2010). However, it is noted that the changes of the LOS field alone cannot provide complete understanding of the field restructuring (Hudson 2011).

It is notable that vector magnetic field data have been made available with the Helioseismic and Magnetic Imager (HMI) instrument (Schou et al. 2012) on board the newly launched Solar Dynamics Observatory (SDO). Its unprecedented observing capabilities give a favorable opportunity to finally resolve many uncertainties regarding the evolution of photospheric magnetic field in relation to flares/CMEs. I took advantage of this new observational capability to study the evolution of magnetic fields and velocity fields to understand the mechanics of solar eruption events and the dynamics of the flaring process.

CHAPTER 2

RESPONSE OF THE PHOTOSPHERIC MAGNETIC FIELD TO THE X2.2 FLARE ON 2011 FEBRUARY 15

This chapter[1] is a case study of the sudden photospheric horizontal magnetic field enhancement during the X2.2 flare on 2011 February 15. It is well known that the long-term evolution of the photospheric magnetic field plays an important role in building up free energy to power solar eruptions. Observations, despite being controversial, have also revealed a rapid and permanent variation of the photospheric magnetic field in response to the coronal magnetic field restructuring during the eruption. The Helioseismic and Magnetic Imager instrument (HMI) on board the newly launched *SDO*produces seeing-free full-disk vector magnetograms at consistently high resolution and high cadence, which finally makes possible an unambiguous and comprehensive study of this important back-reaction process. In this study, we present a near disk-center, *GOES*-class X2.2 flare, which occurred in NOAA AR 11158 on 2011 February 15. Using the magnetic field measurements made by HMI, we obtained the first solid evidence of a rapid (in about 30 minutes) and irreversible enhancement in the horizontal magnetic field at the flaring magnetic PIL by a magnitude of $\sim$30%. It is also shown that the photospheric field becomes more sheared and more inclined. This field evolution is unequivocally associated with the flare occurrence in this sigmoidal active region, with the enhancement area located in between the two chromospheric flare ribbons and the initial conjugate hard X-ray footpoints. These results strongly corroborate our previous conjecture that the photospheric magnetic field near the PIL must become more horizontal after

[1]This chapter is based on the following paper:
Wang, Shuo; Liu, Chang; Liu, Rui; Deng, Na; Liu, Yang; Wang, Haimin, The Astrophysical Journal Letters, 745, L17, 2012.

eruptions, which could be related to the newly formed low-lying fields resulted from the tether-cutting reconnection.

2.1 Introduction

In this chapter, we investigate a near disk-center X2.2 flare on 2011 February 15, which provides the first solid evidence of the enhancement in the horizontal field at the flaring PIL using the seeing-free HMI data. We will discuss the implications of such a change in the context of magnetic reconnection model for flares.

2.2 Observations and Data Reduction

The HMI instrument obtains filtergrams in six polarization states at six wavelengths along the Fe I 6173 Å spectral line to compute Stokes parameters $I\ Q\ U\ V$, which are then reduced with the HMI science data processing pipeline to (1) retrieve the vector magnetic field using the Very Fast Inversion of the Stokes Vector (VFISV) algorithm (Borrero et al. 2011) based on the Milne-Eddington approximation, (2) resolve the 180° azimuthal ambiguity using the "minimum energy" method (Metcalf 1994; Leka et al. 2009). As of the time of this writing, only AR11158 processed data have been released by the HMI team. For our study, we use the product of vector magnetograms projected and remapped to heliographic coordinates, with a spatial resolution of ∼1" and a cadence of 12 minutes.

The temporal and spatial relationship between the change of the photospheric fields and flare energy release can provide important clues concerning the eruption mechanism. The evolution of the flare hard X-ray (HXR) emission was entirely registered by the *Reuven Ramaty High Energy Solar Spectroscopic Imager* (*RHESSI*;Lin et al. 2002). PIXON images (Hurford et al. 2002) in the 35–100 keV energy range showing the flare footpoints were reconstructed using the front segments of detectors 2–8 with 16–32 s integration time throughout the event. To provide the

chromospheric and coronal context, we also used Hα images taken by the Solar Optical Telescope (SOT; Tsuneta et al. 2008) on board *Hinode*, and EUV images made by the Atmospheric Imaging Assembly (AIA; Lemen et al. 2012) on board *SDO*.

2.3 Results

The $\beta\gamma\delta$ region NOAA 11158 was located close to the disk center (S21°, W21°) when the 2011 February 15 X2.2 flare started at 01:44 UT, peaked at 01:56 UT, and ended at 02:06 UT in *GOES* 1–8 Å flux. The flare was initiated at the center of the active region, where opposite magnetic flux concentrations underwent a counterclockwise rotation-like motion possibly resulting in highly sheared fields along the PIL (Li et al. 2011; Sun et al. 2012). By monitoring the evolution of horizontal field, a compact region R along the PIL (enclosed by the white bordered line) is readily identified to show a pronounced enhancement of horizontal field strength $B_h = \sqrt{B_x^2 + B_y^2}$ after the flare (cf. Figures 2.1 (a) and (b)). Close temporal association of this field change with flare emissions and its permanence relative to the flare duration are demonstrated in Figure 2.2(a) covering a period spanning 10 hrs, in which we find that $\langle B_h \rangle$ at the region R increases by ∼30% from ∼1300 G to ∼1700 G in ∼30 minutes. This rapid evolution ensues from the beginning of the flare at 01:44 UT, with the change-over time cotemporal with the rapid rising of soft X-ray flux and peaking of HXR emissions. To further characterize the properties of magnetic field, we calculate magnetic shear $\tilde{S}$, weighted shear angle $\mathring{S}$, and magnetic inclination angle φ. Here $\tilde{S}$ is defined as the product of field strength and shear angle $\tilde{S} = B \cdot \theta$ (Wang et al. 1994; Wang 2006; Jing et al. 2008), where $B = |\boldsymbol{B}|$, $\theta = \cos^{-1}(\boldsymbol{B} \cdot \boldsymbol{B}_p)/(BB_p)$, and the subscript p represents the potential field. The weighted shear angle of a region of interest with n pixels is then $\mathring{S} = \sum_i \tilde{S}_i / \sum_i B_i$, where i=1,2,...n. The inclination angle φ relative to the horizontal plane is $\varphi = \tan^{-1}(|B_v|/(B_x^2 + B_y^2)^{1/2})$. From the results shown in Figures 2.2(b)–(d), it can be clearly seen that all of $\langle \tilde{S} \rangle$, $\mathring{S}$, and $\langle \varphi \rangle$ exhibit an

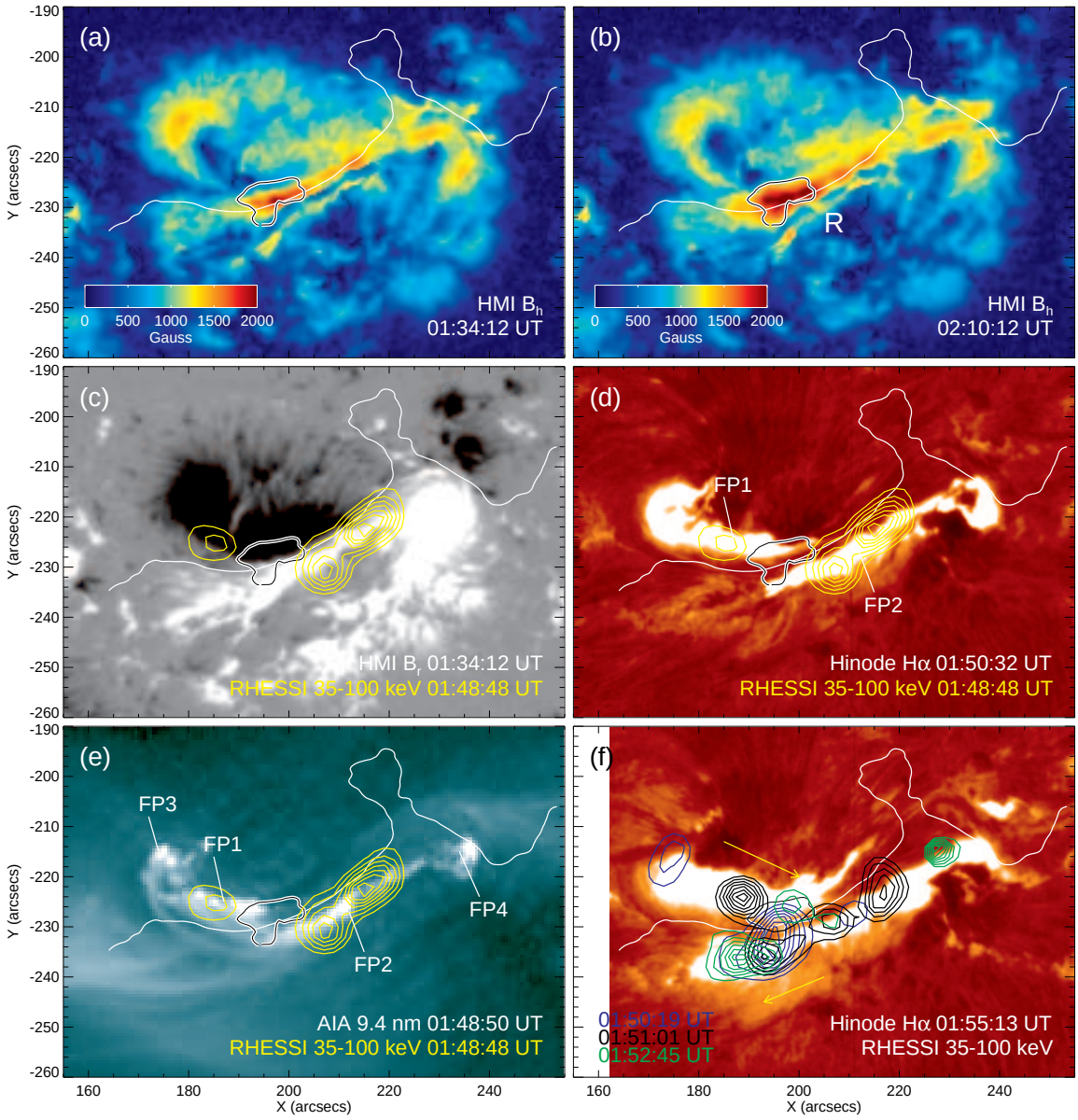

Figure 2.1 Pre- (a) and post-flare (b) HMI B_h maps revealing the enhancement of horizontal field in a region R at the PIL (white line) as enclosed by the white bordered line, which is defined based on the smoothed difference image of B_h. A preflare B_v map in (c) (scaled at ± 1 kG), the first available *Hinode*/SOT Hα image in (d), an AIA 94 Å image at the flare onset in (e), and an Hα image at the flare peak time in (f) are overplotted with contours (30%–90% of the maximum flux) denoting *RHESSI* PIXON images. The arrows in (f) indicate the direction of motion of the main HXR footpoints, as well as that of the chromospheric ribbons besides their separation.

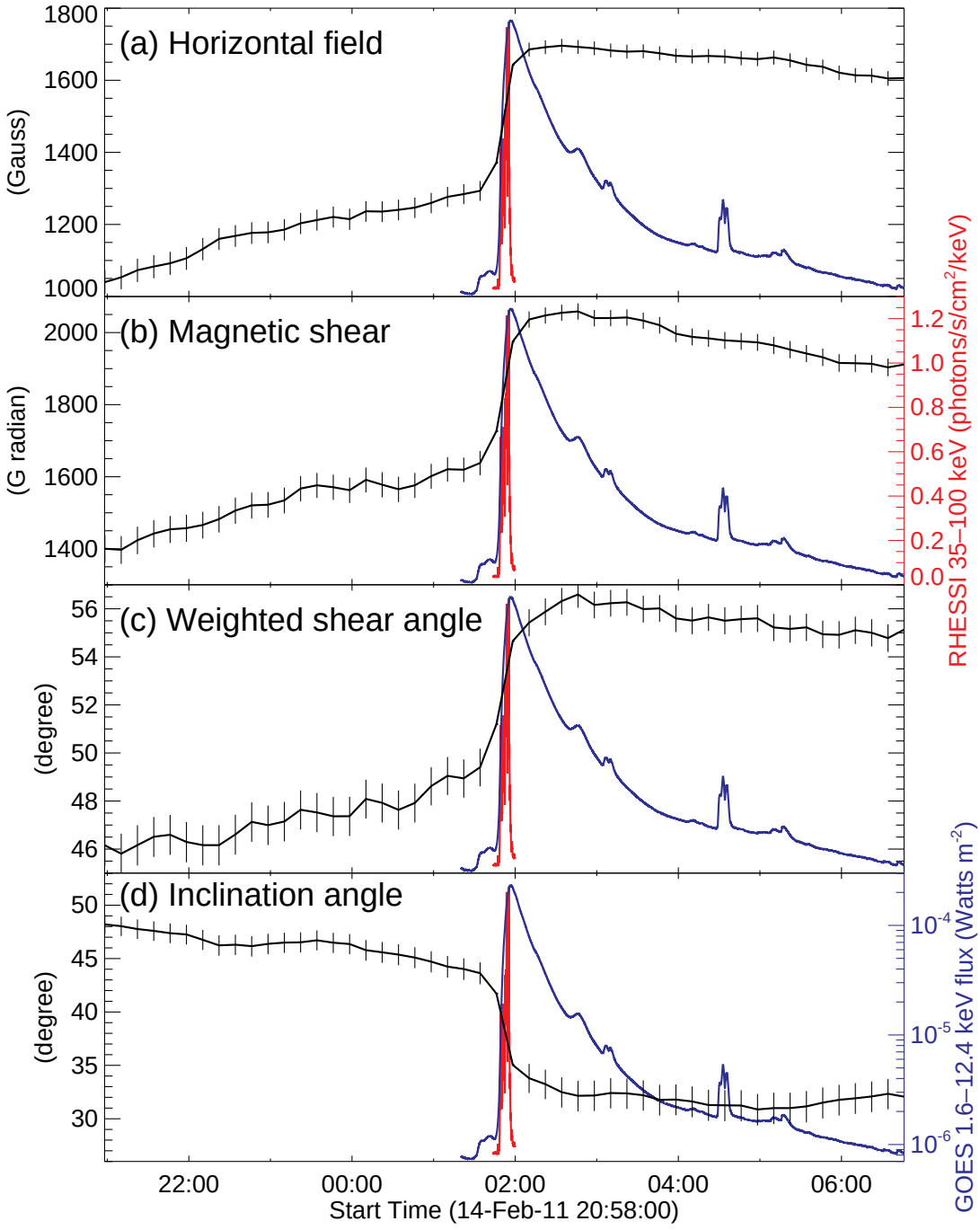

Figure 2.2 Temporal evolution of various magnetic properties of the region R enclosed by the white bordered line in Figure 2.1, in comparison with the light curves of *RHESSI* HXR flux in the 35–100 keV energy range (red) and *GOES* flux in 1–8 Å (blue). The vertical error bars indicate 3σ level. See § 2.3 for details.

abrupt change in the field strength, inclination angle, and azimuthal angle by about 400 G radian, 7°, and −10°, respectively, within the same transition time as $\langle B_h \rangle$ upon the flare occurrence. Please note that in order to demonstrate that the rapid changes are very significant compared to variations seen in the long-term evolution, we plot the $3\sigma_{pre}$ ($3\sigma_{pos}$) as error bars in Figure 2.2, where σ_{pre} (σ_{pos}) is derived from the linear fit of the temporal evolution of each quantity in the preflare (postflare) state. Corroborating our previous studies (Wang & Liu 2010, and references therein), the above rapid developments evidenced by the unambiguous HMI observation strongly suggest a more horizontal and sheared state of the photospheric magnetic field at the region R after the flare. We note that although the increase of $\tilde{S}$ and $\mathring{S}$ seems contrary to the relaxation of nonpotentiality as required to energize eruptions, it has been demonstrated using field extrapolations that the increase is localized and both $\tilde{S}$ and $\mathring{S}$ decrease above a certain height (Jing et al. 2008; Sun et al. 2012; Liu et al. 2012). The magnetic free energy in the 3-D volume is reduced after the flare.

On the spatial relationship between the field change and flare emissions, the region R lies between the earliest conjugate HXR footpoint sources at ∼01:49 UT (Figure 2.1(c)) and the ends of the double J-shaped flare ribbons (Figure 2.1(d)). Intriguingly, AIA 94 Å images show two extra footpoint-like flare brightenings FP3 and FP4 at the two far ends of the flaring PIL (Figure 2.1(e)). Co-spatial HXR emissions at FP3 and FP4 were observed few minutes later (Figure 2.1(f)), and the motion of HXR footpoints as well as the evolution of chromospheric ribbons generally proceed in such a manner as to reduce the magnetic shear, along the PIL (illustrated by the arrows in Figure 2.1(f)) as reported in eruptive sigmoids (e.g., Ji et al. 2008). These lead us to a picture as we schematically illustrate in Figure 2.3, where the flare could be triggered by the tether-cutting reconnection (Moore et al. 1995, 2001) between the two sets of sigmoidal loops FP3–FP2 and FP4–FP1 as clearly discernible in EUV images, which results in the J-shaped flare ribbons (also see Schrijver et al.

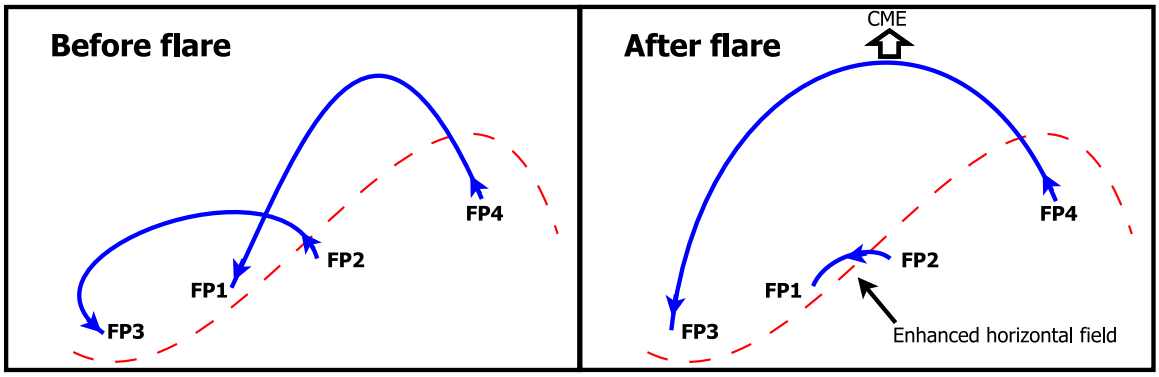

Figure 2.3 Schematic picture interpreting our observations based on the model of Moore et al. (2001). Two sigmoidal loops FP3–FP2 and FP4–FP1 in the preflare state (left panel) reconnect to create a large-scale erupting loop FP3–FP4 escaping as a CME and smaller loop FP1–FP2 lying close to the surface contributing to the detected surface magnetic field change (right panel). For clarity, overlying arcade fields and their reconnection leading to flare ribbons are omitted.

2011). The reconnected large-scale fields FP3–FP4 could erupt outward to become the halo CME associated with this flare, and the newly formed smaller loops FP1–FP2 lying close to the surface could then account for the enhanced B_h at the region R. Such a reconnection of two current-carrying loops would also effectively lead the current path to move downward closer to the surface, which can explain the increase of $\tilde{S}$ and $\mathring{S}$ (Melrose 1997). Alternatively, increase of the magnetic nonpotentiality at and near the surface could result from the newly emerging, sheared magnetic flux (Jing et al. 2008), which could occur after the relaxation of fields above the surface due to the flare energy release. It is worth mentioning that the region R at the PIL is between flare ribbons/kernels at opposite polarities, hence the observed field changes cannot be attributed to flare emissions (Patterson & Zirin 1981; Qiu & Gary 2003). Detailed investigation of the flare HXR emission in further relation to the coronal field dynamics is out of the scope of the current study and will be presented in a subsequent publication.

2.4 Summary and Discussion

We have used the unprecedented SDO/HMI vector field observations to analyze the changes of the photospheric magnetic field associated with the first X-class flare in the solar cycle 24, with the aid of images of flare emissions in multiple wavelengths. Main results are as follows.

1. A compact region R along the flaring PIL shows a rapid and permanent enhancement of $\langle B_h \rangle$ by 400 G ($\sim$30% of the preflare magnitude) within about 30 minutes, which has a close temporal relationship with the flare HXR emission. Meanwhile, the nonpotentiality represented by magnetic shear also exhibits a pronounced increase near the surface.

2. The initial HXR sources FP1 and FP2 as well as the double J-shaped flare ribbons are at the two ends of the region R lying at the central of this sigmoidal

active region. Two additional flare footpoints FP3 and FP4 are clearly seen in the hot 94 Å channel, located at the far ends of the sigmoid. We suggest that the tether-cutting reconnection (Moore et al. 2001) between the loops FP3–FP2 and FP4–FP1 produces the short and low-lying loops FP1–FP2, which could explain the enhanced B_h as well as $\tilde{S}$ and $\mathring{S}$ at the region R (Melrose 1997). The detected enhancement of nonpotentiality on the surface could also be due to the newly emerging, sheared fields (Jing et al. 2008).

In summary, the HMI observations presented in this study constitute the first solid evidence of flare-induced changes of the photospheric magnetic field, which strongly endorses our previous results using ground-based vector magnetograms subject to seeing variation (Wang & Liu 2010, and references therein). The unambiguously observed enhancement of horizontal field on the surface strongly suggests that the photospheric magnetic field could respond to the coronal field restructuring by tilting toward the surface (i.e., toward a more horizontal state) near the PIL, and that this development may be due to the tether-cutting reconnection producing the flare. This view is also well in line with the recent theoretical development (Hudson et al. 2008; Fisher et al. 2012), where the back reaction on the solar surface resulting from the coronal field evolution as required by the energy release is quantitatively assessed. Further systematic studies of flare-related magnetic field change, especially when aided with extrapolation models, are promising to provide further insight into the relationship between the surface field change and coronal magnetic reconnection (e.g., Sun et al. 2012; Liu et al. 2012).

CHAPTER 3

THE RELATIONSHIP BETWEEN THE SUDDEN CHANGE OF THE LORENTZ FORCE AND THE MAGNITUDE OF ASSOCIATED FLARES

In this chapter[1], a statistical study is presented regarding the sudden photospheric horizontal magnetic field enhancement during major flares and the corresponding change of vertical Lorentz force. The rapid and irreversible change of photospheric magnetic fields associated with flares has been confirmed by many recent studies. These studies showed that the photospheric magnetic fields respond to coronal field restructuring and turn to a more horizontal state near the magnetic polarity inversion line (PIL) after eruptions. Recent theoretical work has shown that the change in the Lorentz force associated with a magnetic eruption will lead to such a field configuration at the photosphere. The Helioseismic Magnetic Imager has been providing unprecedented full-disk vector magnetograms covering the rising phase of the solar cycle 24. In this study, we analyze 18 flares in four active regions, with GOES X-ray class ranging from C4.7 to X5.4. We find that there are permanent and rapid changes of magnetic field around the flaring PIL, the most notable of which is the increase of the transverse magnetic field. The changes of fields integrated over the area and the derived change of Lorentz force both show a strong correlation with flare magnitude. It is the first time that such magnetic field changes have been observed even for C-class flares. Furthermore, for seven events with associated CMEs, we use an estimate of the impulse provided by the Lorentz force, plus the observed CME velocity, to estimate the CME mass. We find that if the time scale of the back reaction is short, i.e., in the order of 10 s, the derived values of CME mass ($\sim 10^{15}$g) generally agree with those reported in literature.

[1]This chapter is based on the following paper:
Wang, Shuo; Liu, Chang; Wang, Haimin, The Astrophysical Journal Letters, 757, L5, 2012.

3.1 Introduction

Solar flares have been understood as an energy release process due to magnetic reconnections in the solar corona (Kopp & Pneuman 1976). The magnetic fields in the solar corona are anchored in the dense photosphere. Historically, the photospheric magnetic fields were assumed to be unaffected by flares on short time scales because of high mass density there. Of course their long-term evolution is well known to play an important role in storing the energy and triggering the flares.

Wang (1992) and Wang et al. (1994) were the first to show observational evidence of flare-related rapid/irrevisible change of photospheric magnetic fields based on ground-based vector magnetograms. The most striking but controversial finding at that time was the increase of magnetic shear along the magnetic polarity inversion line (PIL). Using line-of-sight magnetograms of SOHO/MDI, Kosovichev & Zharkova (2001) found that some irreversible variations of magnetic field in the lower solar atmosphere happened very rapidly in the vicinity of PILs at the beginning of the flare of 2000 July 14. Wang et al. (2002) analyzed the observed photospheric magnetic flux evolution across 6 X-class flares, and found significant permanent changes associated with all the events. After surveying 15 X-class flares, Sudol & Harvey (2005) concluded that the change in the line-of-sight (LOS) magnetic field always occurs during X-class flares. Wang (2006) noticed that when an active region is away from the disk center, the reconnected low-lying fields would cause an apparent increase of the flux in the polarity toward the limb and a decrease in the polarity closer to the disk center.

Until the launch of SDO, these studies were very limited due to the paucity of continuous/consistent high-quality vector magnetogram series. With a nearly continuous coverage over the entire solar disk, vector magnetograms are being obtained from the Helioseismic and Magnetic Imager (HMI; Schou et al. 2012) on board the Solar Dynamics Observatory (SDO), making possible extensive studies that

achieve a fundamental physical understanding of the observations. A number of recent papers using HMI data have all pointed to the same conclusion that photospheric magnetic fields turn more horizontal immediately after flares and that magnetic shear increases at surface but relaxes in the corona as described in chapter 2 (Wang et al. 2012b; Sun et al. 2012; Liu et al. 2012). In chapter 2, we found a rapid (in about 30 minutes) and irreversible enhancement in the horizontal magnetic field at the flaring magnetic PIL by a magnitude of $\sim 30\%$ associated with the X2.2 flare on 2011 February 15. Petrie (2013) has analyzed the magnetic field evolution and Lorentz forces in the X2.2 flare on 2011 February 15, and also found a large Lorentz force change coinciding with the eruption.

From the theoretical side, Hudson et al. (2008) quantitatively assessed the back reaction on the photosphere and solar interior with the coronal field evolution required to release flare energy, and predicted that the magnetic field should become more horizontal after flares. Wang & Liu (2010) were first to link this idea to observed field changes. They provided observational evidence of the increase of transverse field at the PIL when vector magnetograms were available. When only the LOS field measurement was available, they found that if the source active region is not located at the disk center, the measured apparent LOS field changes are consistent with the picture of Hudson et al. (2008), i.e., fields turn more horizontal across the PIL. They used the same concept which we mentioned before: due to the projection effect, there is an apparent increase of the flux in the polarity toward the limb and a decrease for the polarity closer to the disk center. More recently, Fisher et al. (2012) and Hudson et al. (2012) further developed analytic modeling, by separately considering Lorentz forces acting on the upper solar atmosphere and the solar interior. The upward momentum of the erupting plasma can be estimated by equating the change in the upward momentum with the Lorentz force impulse acting on the outer solar atmosphere. The authors also argued that the back reaction on the solar interior may

be responsible for the sudden sunspot motion on the photosphere and the excitation of seismic waves in the interior.

It is noted that the previous studies were mainly focused on large flares such as X-class or upper M-class events. HMI has been obtaining seeing-free, high-resolution data since 2010 April. In this chapter, we target our study on the magnetic field change associated with flares in a broad range of magnitudes, including C-class events. We also attempt to find the possible relationship among flare magnitude, field changes, and momentum involved in the eruptions.

In Section 3.2, we will describe observations and data processing, and will show two examples of case studies. The statistical results between flare magnitude and field changes will be presented in Section 3.3, in which we will also discuss a practical method to estimate the CME mass. Section 3.4 will give the summary and discussion.

3.2 Observations and Data Processing

HMI and the Atmospheric Imaging Assembly (AIA; Lemen et al. 2012) on board SDO provide full-disk, multi-wavelength observations in high spatial and temporal resolution. The LOS magnetic field observation with $\sim 0.5''$ pixel scale and a 45s cadence has recorded all flares on the solar disk since April 2010. The noise level of the LOS field measurement is 10 G. HMI also provides full-disk vector magnetic field measurement with a separate system. However, the measurement has larger uncertainty due to the difficulty in the Stokes inversion. It is noted that HMI team has put significant effort to improve the inversion code. Using an average of 12-minute data, the accuracy of the transverse field measurement is in the order of 100 G as derived from Stokes Q and U. We are using the latest release of the processed data from the HMI data archive. The HMI vector fields are derived using the Very Fast Inversion of the Stokes Vector (VFISV) algorithm (Borrero et al. 2011) based on the Milne Eddington approximation. The 180° azimuthal ambiguity is resolved with the

minimum energy method (Metcalf 1994; Leka et al. 2009). Four active regions that produced X-class flares in 2011 and 2012 have been analyzed in this study. They are NOAA regions 11158, 11166, 11283, and 11429.

To demonstrate the procedure of data handling, let us first describe the analysis of the largest flare in our sample: the X5.4 flare in AR 11429. AR 11429 was located in the northeast of the solar disk when the X5.4 flare peaked at 00:24 UT on 2012 March 07. The data cube covers the entire active region with projection effect corrected.

For this and all the events under study, we first scrutinize the movie of the horizontal fields covering the flare. Rapid/irreversible enhancement of the horizontal field is always clearly shown across the flaring PIL that can be identified with the help of the corresponding AIA images Figure (3.1(d)). To pinpoint the location of the horizontal field change, we construct a difference image by subtracting a postflare horizontal field image Figure (3.1(b)) from a preflare horizontal field image Figure (3.1(a)). We then use the contour with a level of 120 G (slightly above the confidence level of the measured transverse field) as the boundary of the region of interest (ROI) for further quantitative analysis. In Figure 3.1(c), the ROI covers part of the flaring PIL. We then plot the mean field change in the ROI as a function of time. As shown in Figure 3.1(e), the horizontal magnetic field within the ROI increases by $\sim$40% from $\sim$650 G to $\sim$920 G in $\sim$30 minutes. This is consistent with all the previous studies that showed a step-like change of the fields. The observed field change is clearly above the fluctuation (indicated by the error bars) by more than an order of magnitude. In addition, we did not detect any transient changes of the fields due to flare emissions as described by Patterson & Zirin (1981) and Qiu & Gary (2003).

Next, we analyze the related Lorentz force change as formulated by Hudson et al. (2008) and Fisher et al. (2012). Here, we focus on the Lorentz force change in the volume below the photosphere using the equation in Fisher et al. (2012):

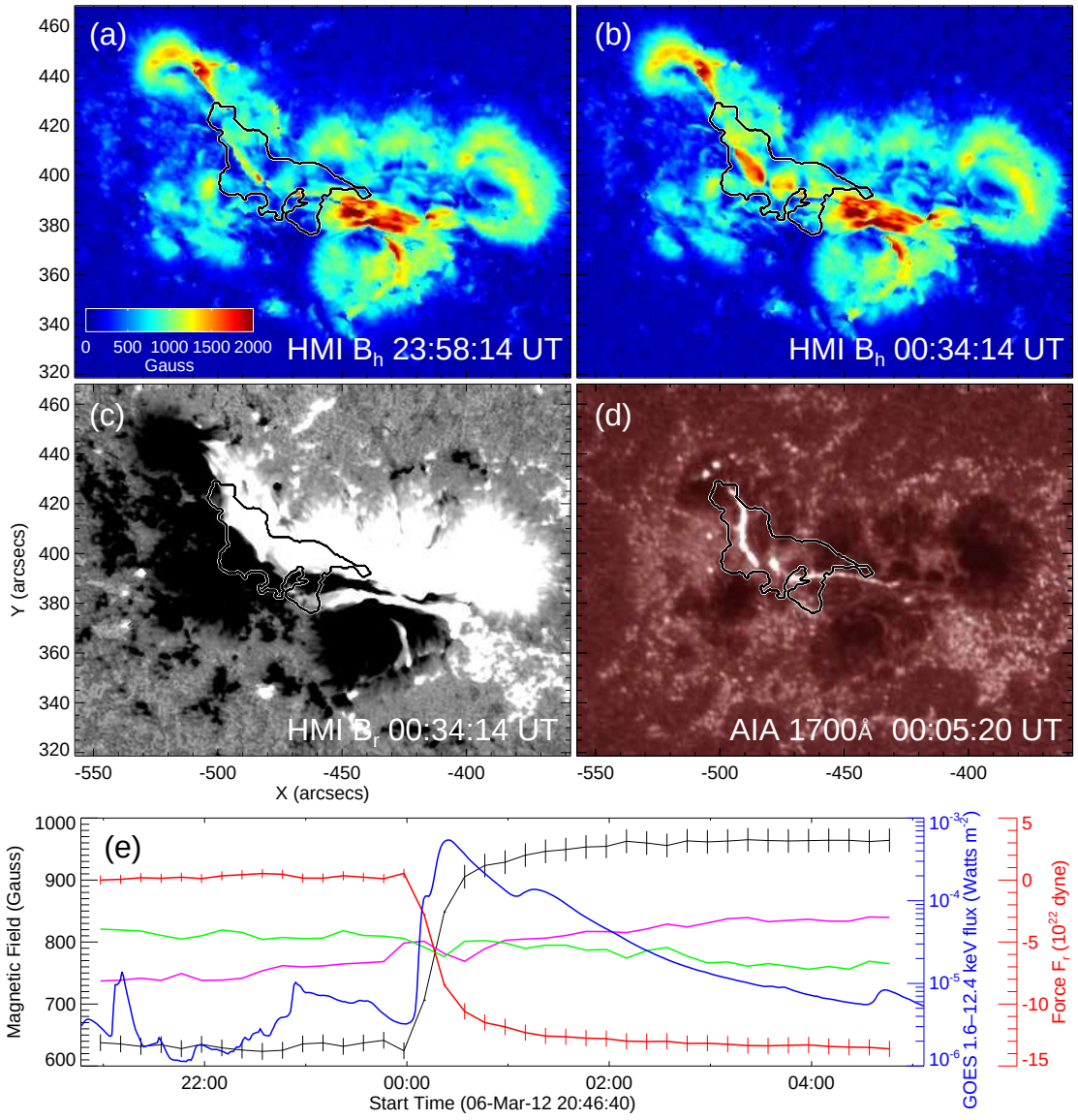

Figure 3.1 X5.4 flare on 2012 March 07. Panels (a) and (b) show the preflare and postflare horizontal magnetic field maps. Panel (c) is the radial magnetic field map. Panel (d) is an AIA 1700 Å map. The ROI is overplotted with the white-bordered black contour. In the panel (e), the black and red curves with vertical error bars are the temporal evolution of the mean horizontal magnetic field and radial Lorentz force within the ROI respectively, in comparison with the GOES light curve in 1–8 Å (blue curve). The vertical error bars indicate a 3σ level of the fluctuation in the pre- and postflare states. Purple and green curves represent positive and negative mean radial magnetic fields, respectively, which do not show obvious step wise changes.

$$\delta F_r = \frac{1}{8\pi} \int_{A_{ph}} dA(\delta B_r^2 - \delta B_h^2), \tag{3.1}$$

where B_r is the vertical field while B_h is the horizontal field. We note that the radial field shows no rapid irreversible change in any of the 18 events (see Figure 3.1(e) and Figure 3.2(e) as examples). Therefore, we omitted the term δB_r^2 to minimize the effect of longer term evolution. The summation of δF_r in the whole ROI gives the value of the integrated Lorentz force change. The total change of Lorentz force in the volume below the photosphere during this flare is 1.1×10^{23} dyne, comparable with previous studies.

The same data analysis procedure is applied to all the 18 events in four active regions. The result of the C4.8 event on 2011 Feburary 15 is shown in Figure 3.2. This event did not occur in the main PIL that produced the large X2.2 flare on the same day. However, the stepwise increase of the horizontal field is clearly demonstrated.

3.3 Statistical Results

After studying the horizontal field movies for all observed events in these four ARs, we find that 18 flares (listed in Table 3.1) obviously show a rapid/irreversibe change in the horizontal fields. The magnitude of flares ranges from GOES-class C4.7 to X5.4. In these active regions, all the M2.0 and above flares have the detectable changes. Three out of five M1.0–M1.9 flares and five out of 17 C4.0–C9.9 flares also demonstrate a similar pattern of field change. As described in the previous section, the ROI is defined using a threshold of 120 G based on the difference image between the horizontal fields right before and after flares. We then calculate the integrated horizontal magnetic field change and the downward Lorentz force change. For each event, we find that (1) the ROI is spatially related to the flare kernels pinned down with AIA data, covering the flaring PIL; and (2) the evolution of magnetic field and

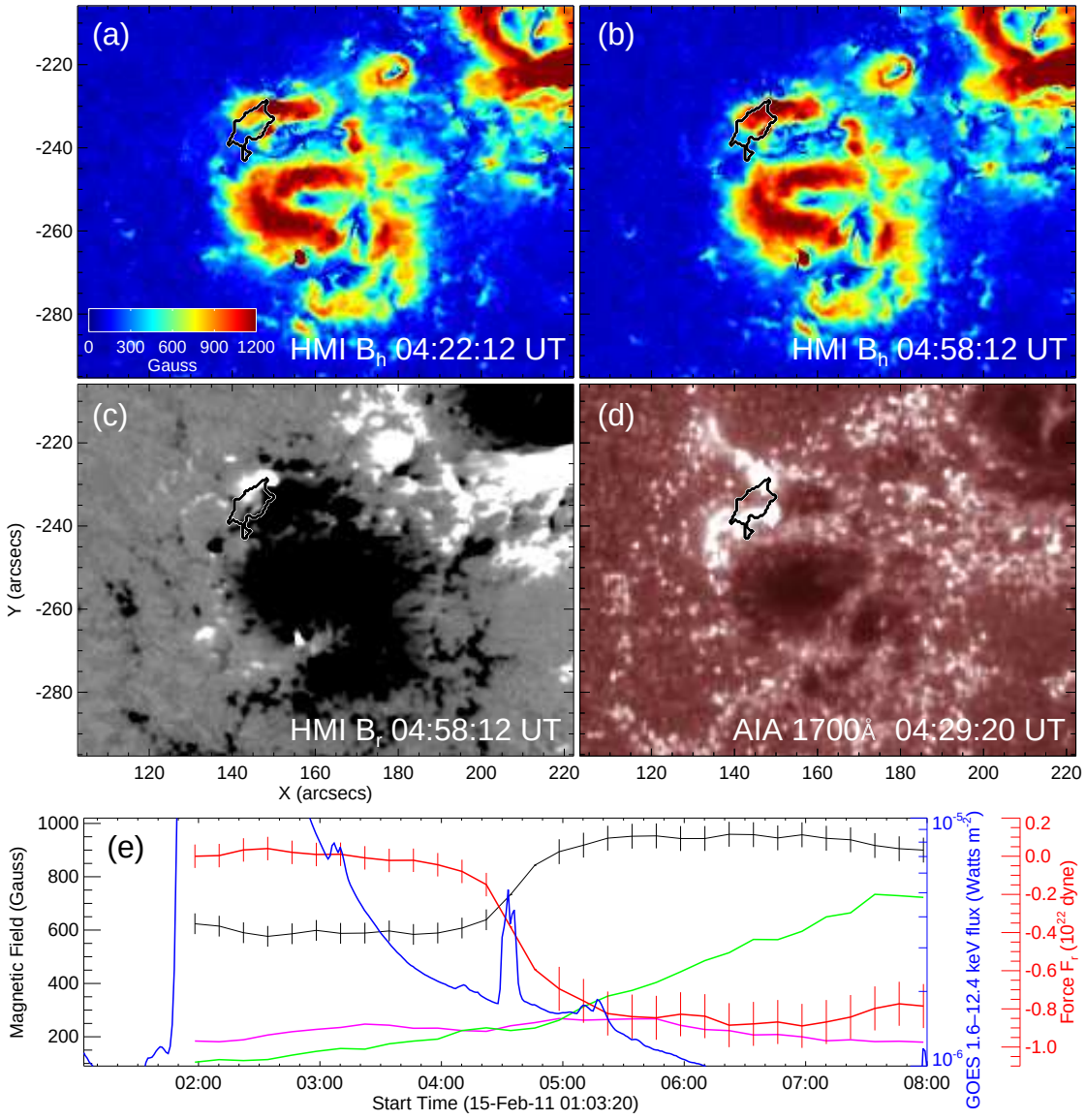

Figure 3.2 Same as Figure 3.1, but for the C4.8 flare on 2011 February 15. This small flare occurred in a different PIL that produced the X2.2 event around 02 UT.

the downward Lorentz-force change both show variations in a stepwise fashion. Based on this statistical study, we find significant correlations between the peak GOES X-ray flux and both the integrated horizontal field change and the total downward Lorentz force change. The results are shown in Figure 3.3.

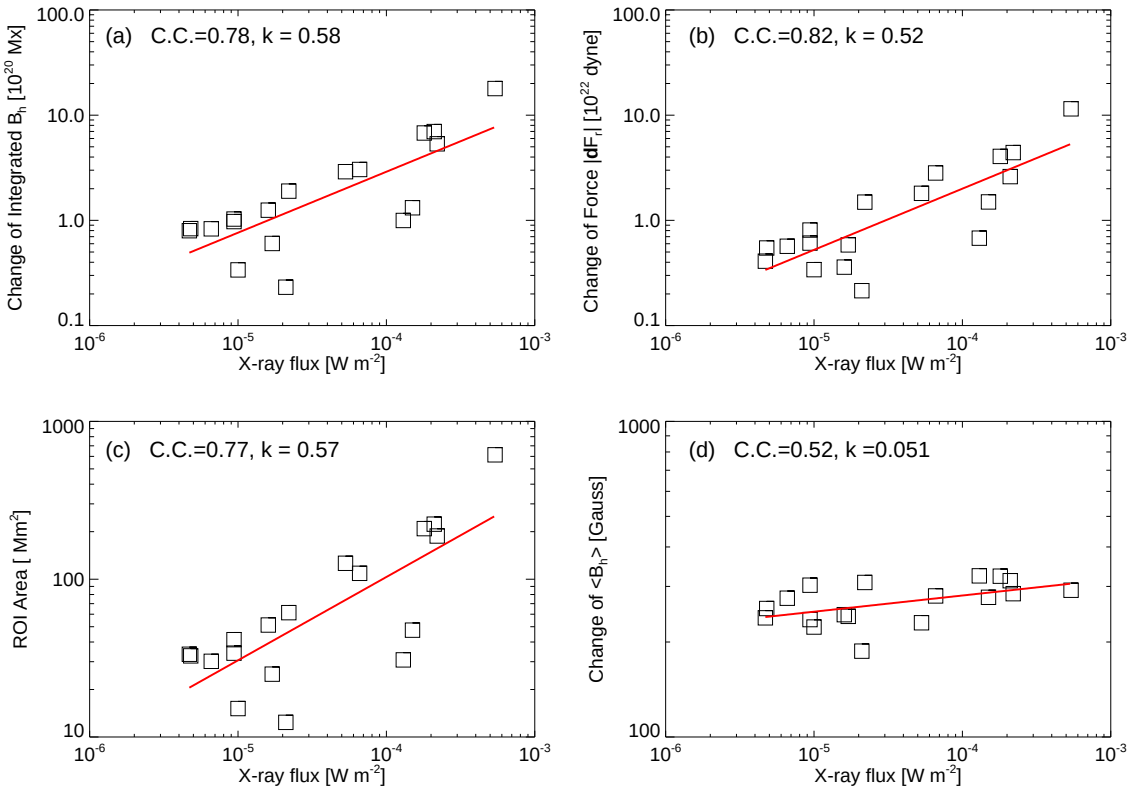

Figure 3.3 Scatter plots of the peak GOES X-ray flux in 1–8 Å vs. various parameters. The red lines show the least-squares linear fit to the data points. The correlation coefficient (C.C.) and slope (k, corresponding to power index in linear-linear plot) are shown in each panel.

In panels (a), (b), (c), and (d) of Figure 3.3, we plot the integrated horizontal field enhancement, the total change of the downward Lorentz force, ROI size, and the mean horizontal field change respectively as functions of the peak soft X-ray flux of flares. It is clear that the amount of field change is correlated well with flare magnitude. The linear fit on a log-log scale gives a cross correlation coefficient of around 0.8 and a slope (corresponding power index) of around 0.5 for the first

Table 3.1 Events with Rapid Change of Horizontal Photospheric Magnetic Fields

GOES 1–8 Å Peak (UT)	NOAA AR	GOES Class	Integrated δB_h (10^{20} Mx)	Total δF_r (10^{22} dyne)
2011 Feb 13 13:56	11158	C4.7	0.80	0.41
2011 Feb 13 17:38	11158	M6.6	3.0	2.8
2011 Feb 14 12:53	11158	C9.4	1.0	0.81
2011 Feb 14 17:26	11158	M2.2	1.9	1.5
2011 Feb 14 19:30	11158	C6.6	0.83	0.57
2011 Feb 15 01:56	11158	X2.2	5.3	4.4
2011 Feb 15 04:32	11158	C4.8	0.83	0.55
2011 Feb 16 14:25	11158	M1.6	1.2	0.36
2011 Mar 09 14:02	11166	M1.7	0.97	0.61
2011 Mar 09 22:12	11166	C9.4	0.60	0.59
2011 Mar 09 23:23	11166	X1.5	1.3	1.5
2011 Sep 06 01:50	11283	M5.3	2.9	1.8
2011 Sep 06 22:20	11283	X2.1	7.0	4.1
2011 Sep 07 22:38	11283	X1.8	6.8	2.6
2012 Mar 06 07:55	11429	M1.0	0.34	0.34
2012 Mar 06 12:41	11429	M2.1	0.23	0.21
2012 Mar 07 00:24	11429	X5.4	17	11
2012 Mar 07 01:14	11429	M1.3	1.0	0.68

three parameters Figure (3.3 (a)–(c)). The last parameter (Figure 3.3(d)) is not sensitive to the flare magnitude. We use the unit of magnetic flux Mx to describe the integrated horizontal field. In reality, it is not magnetic flux as the horizontal field is not normal to the surface. We note a previous study of Chen et al. (2007), in which the darkening of sunspot intensity at the flaring PIL line is also related to the flare magnitude, consistent with the picture of fields turn to horizontal. However, in that study, the authors were not able to analyze the magnetic structure change.

This is the first time that the rapid/irreversible field changes are found to be associated with C-class flares. Of course, we need to be careful about the confidence level of the detected changes. In Figure 3.1(e) and Figure 3.2(e), to demonstrate the fluctuation before and after the flare, we plot the $3\sigma_{\rm pre}$ ($3\sigma_{\rm pos}$) as error bars, where $\sigma_{\rm pre}$ ($\sigma_{\rm pos}$) is derived from the linear fit of the temporal evolution of the horizontal field in the preflare (postflare) state. As shown in Figure 3.2(e), the rapid change of the horizontal field even for the C4.8 flare is significant compared to variations seen in the long-term evolution.

Our main motivation of this study is to estimate the change of the Lorentz force acting on either the outer solar atmosphere or on the solar interior. One important application is to evaluate the upward momentum associated with magnetic eruptions. The upward impulse exerted on the outer solar atmosphere is suggested to account for the CME momentum (Fisher et al. 2012). Therefore the estimated CME mass is:

$$M_{CME} \simeq \frac{1}{2}\frac{\delta F_r \delta t}{v}, \tag{3.2}$$

where here, δF_r is the change of the Lorentz force acting on the outer solar atmosphere (with the same magnitude but opposite sign as δF_r in Eq. 1), v is the CME speed available from the LASCO CME catalog [2], and δt is the change over time of the field.

[2]http://cdaw.gsfc.nasa.gov/CME_list

In using this expression, we've made the assumption that the entire mass moves with the same velocity, a gross over-simplification, and we have also ignored the work done against gravity. It does, nevertheless, provide an indpendent estimate for the CME mass. Due to the 12 minute cadence of HMI data, it is difficult to evaluate the critical parameter δt for the CME mass estimate. There is evidence that the back-reaction is impulsive (Donea & Lindsey 2012; Sudol & Harvey 2005; Petrie & Sudol 2010). We therefore use the typical time scale of hard X-ray spike time, i.e., around 10 s, as a rough estimate of δt during the flare impulsive phase. We also assume that the initial CME velocity is zero. The estimated masses of the seven CME events are shown in Table 3.2, and are consistent with the typical value in the previous studies (Vourlidas et al. 2010; Carley et al. 2012). Please note that among the 18 events, these seven are the only ones that have identified CMEs in the LASCO catalog. Unfortunately, the mass estimates of these CMEs are not yet available from LASCO white-light intensity analysis to be compared with our derived values.

3.4 Summary and Discussion

Taking advantage of the newly released HMI vector magnetograms in flare-productive active regions, we are able to analyze changes of vector magnetic fields associated with 18 flares. This is the first time that such changes are found for small flares down to the GOES C class. The results listed in Tables 3.1 and 3.2 agree with previous studies in the following aspects:

1. All events exhibit a step-like increase of the horizontal magnetic field after flares, with an order of magnitude of 10^{20} Mx after integrating over the ROI.
2. The changes are co-temporal with the flare initiation, and the change-over time is about three time bins of the HMI data, i.e., 36 minutes. However, we believe that the reaction time for the field change could be much shorter than this.

From the statistical studies of the 18 events, we also note the following:

Table 3.2 Events with CME

GOES 1–8 Å Peak (UT)	NOAA AR	GOES Class	CME Time (UT)	CME Speed (km s^{-1})	CME Mass (10^{15} g)
2011 Feb 13 17:38	11158	M6.6	18:36	373	3.8
2011 Feb 14 17:26	11158	M2.2	18:24	326	2.3
2011 Feb 15 01:56	11158	X2.2	02:24	669	3.3
2011 Mar 09 23:23	11166	X1.5	23:05	332	2.3
2011 Sep 06 01:50	11283	M5.3	02:24	782	1.2
2011 Sep 06 22:20	11283	X2.1	23:05	575	2.3
2011 Sep 07 22:38	11283	X1.8	23:05	792	2.6

1. The permanent magnetic field change is always co-spatial with the PIL connecting the two primary flare kernels.
2. Significant linear relationships between the peak GOES X-ray flux and all the following parameters are found: the size of the affected area, the integrated horizontal field change, and the total downward Lorentz force change.

The above findings clearly support the idea of back reaction of surface magnetic fields to the eruption in the corona, as proposed by Hudson et al. (2008) and Fisher et al. (2012). The fields are observed to change from a more vertical to a more horizontal configuration. The downward change of Lorentz force reflects such a topological change in magnetic fields. In the photospheric layers, in static equilibrium before and after eruptive events, there should be a balance between the Lorentz force, gas pressure gradients, and gravity. The Lorentz force difference between the post-flare and pre-flare states is the signature of an unbalanced Lorentz force in the solar atmosphere, occurring during the time of the eruption, in which Lorentz forces are balanced primarily by the inertial force of the accelerating plasma.

If the above physics is correct, then the upward CME momentum can be estimated based on the derived impulse associated with the Lorentz force change. We can then estimate the CME mass. However, as we already mentioned, an uncertain parameter in the equation is the reaction time associated with the field change. We prefer to use a short time (10 s based on the hard X-ray observation), as the change is observed to occur in a time scale close to the temporal resolution of the HMI data. If a longer time is used, the estimated CME mass will be much larger than the established values in literature. It is easier to estimate mass of CMEs for the close-to-limb events based on the white-light image intensity such as that measured by LASCO coronagraph. We are providing an independent method to estimate the CME mass based on the change of the photospheric magnetic field. This is particularly useful for events closer to the disk center. Our positive correlation between the change

of Lorentz force and the peak soft X-ray flux also agrees with the study of Zhang et al. (2004) and Zhang & Dere (2006), in which they found that the CME speed is associated with the soft X-ray flux. A possible future research is to study CMEs at positions between disk center and limb with Thompson scattering method to obtain CME mass, and using the CME mass to find the impulse time.

CHAPTER 4

STUDY OF RAPID FORMATION OF A δ SUNSPOT ASSOCIATED WITH THE 2012 JULY 2 C7.4 FLARE USING HIGH-RESOLUTION OBSERVATIONS OF NEW SOLAR TELESCOPE

In this chapter [1], taking advantage of the newly released New Solar Telescope at Big Bear Solar Observatory, a new phenomenon of penumbral formation related to photospheric magnetic field reconstruction during flare is discussed. Rapid, irreversible changes of magnetic topology and sunspot structure associated with flares have been systematically observed in recent years. The most striking features include the increase of horizontal field at the PIL and the co-spatial penumbral darkening. A likely explanation of the above phenomenon is the back reaction to the coronal restructuring after eruptions: a coronal mass ejection carries the upward momentum while the downward momentum compresses the field lines near the PIL. Previous studies could only use low resolution (above $1''$) magnetograms and white-light images. Therefore, the changes are mostly observed for X-class flares. Taking advantage of the $0\farcs1$ spatial resolution and 15 s temporal cadence of the New Solar Telescope at Big Bear Solar Observatory, we report in detail the rapid formation of sunspot penumbra at the PIL associated with the C7.4 flare on 2012 July 2. It is unambiguously shown that the solar granulation pattern evolves to alternating dark and bright fibril structure, the typical pattern of penumbra. Interestingly, the appearance of such a penumbra creates a new δ sunspot. The penumbral formation is also accompanied by the enhancement of horizontal field observed using vector magnetograms from the Helioseismic and Magnetic Imager. We explain our observations as due to the eruption of a flux rope following magnetic cancellation at the PIL. Subsequently the re-closed

[1]This chapter is based on the following paper:
Wang, Haimin; Liu, Chang; Wang, Shuo; Deng, Na; Xu, Yan; Jing, Ju; Cao, Wenda, The Astrophysical Journal Letters, 774, L24, 2013.

arcade fields are pushed down towards the surface to form the new penumbra. NLFFF extrapolation clearly shows both the flux rope close to the surface and the overlying fields.

4.1 Introduction

Solar eruptive events, including flares, filament eruptions, and coronal mass ejections (CMEs) are due to magnetic reconnection or loss of equilibrium in the solar corona (see, e.g., a recent review by Webb & Howard 2012). From time sequence magnetograph observations, irreversible and rapid changes of surface magnetic fields associated with a large number of major flares have been observed (e.g., Wang 1992, 2006; Kosovichev & Zharkova 2001; Wang et al. 1994; Wang & Liu 2012; Wang et al. 2004a,b; Liu et al. 2005; Sudol & Harvey 2005; Petrie & Sudol 2010; Burtseva & Petrie 2013). Wang & Liu (2010) synthesizes earlier studies and presented analysis of new events, and found a trend of increase of horizontal field at the polarity inversion line (PIL) associated with almost all the flares studied by the authors. The results agree with our previous finding of rapid changes of sunspot structure associated with flares (Liu et al. 2005; Deng et al. 2005), where the spot feature near the flaring PIL darkens while part of peripheral penumbra decays. Recently, the HMI on board the SDO is providing state-of-the-art observations under seeing-free condition, which help advance the study of magnetic field changes associated with flares (e.g., Liu et al. 2012; Wang et al. 2012b,c; Petrie 2013). All these photospheric magnetic field changes are interpreted due to either the change of field line orientation or the appearance of newly formed magnetic loops near the surface. In both cases, the changes are more prominent in the horizontal rather than the vertical component.

From the viewpoint of the theory of the flare phenomenon, Hudson et al. (2008) and Fisher et al. (2012) pointed out that the coronal energy release and magnetic restructuring may cause back reaction to the solar surface and interior.

The authors found that after a flare, the photospheric magnetic field may become more horizontal at the PIL. The authors used the simple principle of energy and momentum conservation, and specifically predicted that flares can be accompanied by rapid and irreversible changes of photospheric magnetic field. Melrose (1997, 2012) also provided an explanation for the enhancement of magnetic shear at the flaring PIL, using the concept of reconnection between two current-carrying flux systems. Such a magnetic share increase at the PIL is often observed (Wang et al. 2012b,c). The work of Melrose and those of Hudson and Fisher, may have physics linkage: there are two current systems, one moves upward as part of an eruption and the other moves toward the surface. These might be linked to the tether-cutting reconnection model for sigmoids (Moore et al. 2001; Moore & Sterling 2006).

It is noticeable that even with the SDO/HMI observations, the resolution of data is no better than $1''$. Therefore, the detailed evolution of sunspot structure may not be well observed. The high-resolution ($0\farcs1$) observation with the 1.6 m New Solar Telescope (NST; Goode et al. 2010; Cao et al. 2010) at Big Bear Solar Observatory (BBSO) thus provides a unique opportunity to understand the fine-scale structure change of sunspots associated with flares. Compared with most of the previous observations mainly for X-class flares, NST images also allows such a study related to weaker flares. In this chapter, we provide a detailed analysis of rapid formation of a δ sunspot associated with the C7.4 flare on 2012 July 2 from the NOAA AR 11525. We describe the multiwavelength observations and results in Section 4.2, and summarize and discuss our major findings in Section 4.3.

4.2 Observations and Results

NOAA AR 11525 produced numerous C-class and M-class flares during its disk passage from 2012 June 29 to July 12. Figure 4.1 (f) displays a HMI vertical field covering the entire active region. Multiple PILs and the possible interaction between

emerging flux systems could be the primary reasons of the high flare productivity. We concentrate our analysis on a small field-of-view (FOV) ($27'' \times 27''$) as marked by the black box in (f), in order to scrutinize the flare-related changes of sunspot structure. This FOV includes a main flaring PIL, and is within the larger $70'' \times 70''$ FOV of NST diffraction-limited observation. NST best covers the C7.4 flare on July 2, which started at 18:45 UT, peaked at 18:56 UT, and ended at 19:02 UT in GOES 1–8 Å flux. The related NST observations are at three wavelengths, the Hα line center, H$\alpha-0.75$ Å offband, and the TiO band at 7057 Å which is a good proxy for the photospheric continuum. The cadence of Hα blue-wing images is 6 s, while that of Hα line center and TiO images is 15 s. All the observations were taken with the BBSO's 76 element adaptive optics, which is able to correct most of the atmospheric seeing at these wavelengths. Speckle reconstruction using 100 frames (obtained within 3 s) is subsequently applied in order to obtain diffraction-limited image sequences (i.e., around $0\farcs1$ at Hα and TiO). Figures 4.1 (a) and (b) are the Hα line center and offband images at the flare peak time, showing the double flare ribbons and the erupting material (pointed to by arrows). In fact, this flare is most probably preceded by the eruption of a filament lying along the PIL from ∼18:33:50 onward (see the time-lapse movie). A complete study of the erupting filament will be presented elsewhere. Figures 4.1 (c) and (d) compare preflare and postflare TiO images, with the preceding spots P1–P3 and the following spot F1 labeled. It can be distinctly seen that after the flare, there is a newly formed penumbra (pointed to by the arrow) that directly connects P1 and F1 (see further discussion below). Contours of HMI line-of-sight (LOS) magnetic field is also over-plotted on the pre-flare TiO image in Figure 4.1 (e) to clearly exhibit the polarity of each spot. BBSO did not have magnetograph observations on that day.

To shed light on the 3D magnetic field structure, we resorted to the nonlinear force-free field extrapolation (NLFFF), using HMI vector magnetograms as the

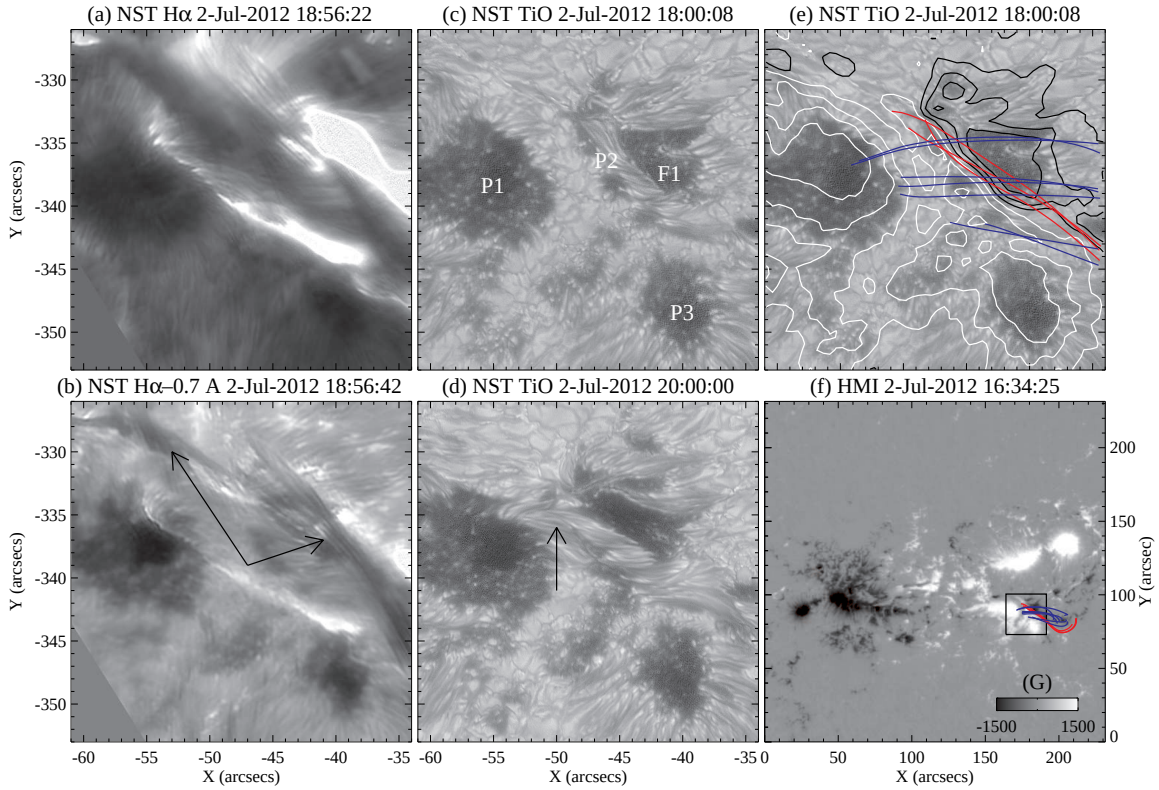

Figure 4.1 NST Hα center (a) and blue-wing (b) images at the flare peak time showing the two flare ribbons and the possible signature of flux rope eruption (pointed to by the arrows in (b)). The NST TiO images about 1 hr before (c) and 1 hr after (d) the flare clearly show the formation of penumbra (pointed to by the arrow in (d)), which connect the northern two umbrae lying in the opposite magnetic field. The same preflare TiO image in (e) is superposed with positive (white) and negative (black) HMI LOS magnetic field contours, with levels of $\pm$200, $\pm$600, $\pm$1000, and 1400 G. All the images are aligned with respect to 18 UT. The remapped HMI vector magnetogram at 16:34 UT displaying the whole active region is shown in (f), overplotted with the black box denoting the approximately same FOV of (a)–(e). The superimposed red and blue NLFFF lines (also in (e)) represent the sheared flux rope along the PIL and the overlying arcade field, respectively. Two movies are associated with the Figure. movie-1a-ha-offband.mpeg is the Hα blue wing movie, while movie-1b-tio.mpeg is the TiO movie.

boundary condition. This extrapolation model uses the "weighted optimization" method as discussed by Wiegelmann (2004). The photospheric boundary is pre-processed to simulate the force-free condition (Wiegelmann et al. 2006). The calculation was performed to a volume of $\sim 171 \times 171 \times 171$ Mm^3. Selected NLFFF lines are superimposed on Figures 4.1 (e) and (f), demonstrating a possible sheared flux rope lying along the PIL (red) and the overlying arcade field (blue). These are nicely consistent with the above observation of the erupting filament and flare ribbons. In the standard flare picture, filament eruption can stretch open the overlying fields, which then reconnect and produce flare ribbons at their footpoints.

We present in Figure 4.2 the time sequence of TiO images right across the flare (panels (a)–(g)) and a corresponding HMI vector magnetic field map (panel (h)). It is evident that there exists strongly sheared fields along the PIL between the positive, ridge-like P2 and negative F1 spots, and that before the flare, a sheared penumbra lies between P2 and F1 (Figure 4.2 (a)). With the occurrence of the flare, a significant new section of penumbra then rapidly forms and is obviously seen to directly connect the main positive spot P1 with the negative F1 (Figures 4.2 (e)–(g)) and hence link part of the flare ribbons (cf. Figures 4.1 (b) and (d)). We note that some penumbral fibrils may apparently join positive spots P1 and P2. This is most probably because that the inclined penumbral field stemming from P1 could have a dip near the region of P2 but then curves up again to reach F1 (e.g., Figure 8 of Wang & Liu 2012). In the sense that the main spots P1 and F1 with opposite magnetic polarity now share a common penumbra, the flare effectively creates a new δ sunspot.

In order to further demonstrate the rapidness of the flare-related penumbral formation, we show in Figures 4.3 (a) and (b) the temporal evolution of the mean TiO intensity within the red boxed region in Figure 4.2 along with that of the corresponding horizontal magnetic field, in comparison with the GOES 1–8 Å flux (the red line). It is remarkable that the TiO intensity begins to sharply drop with the

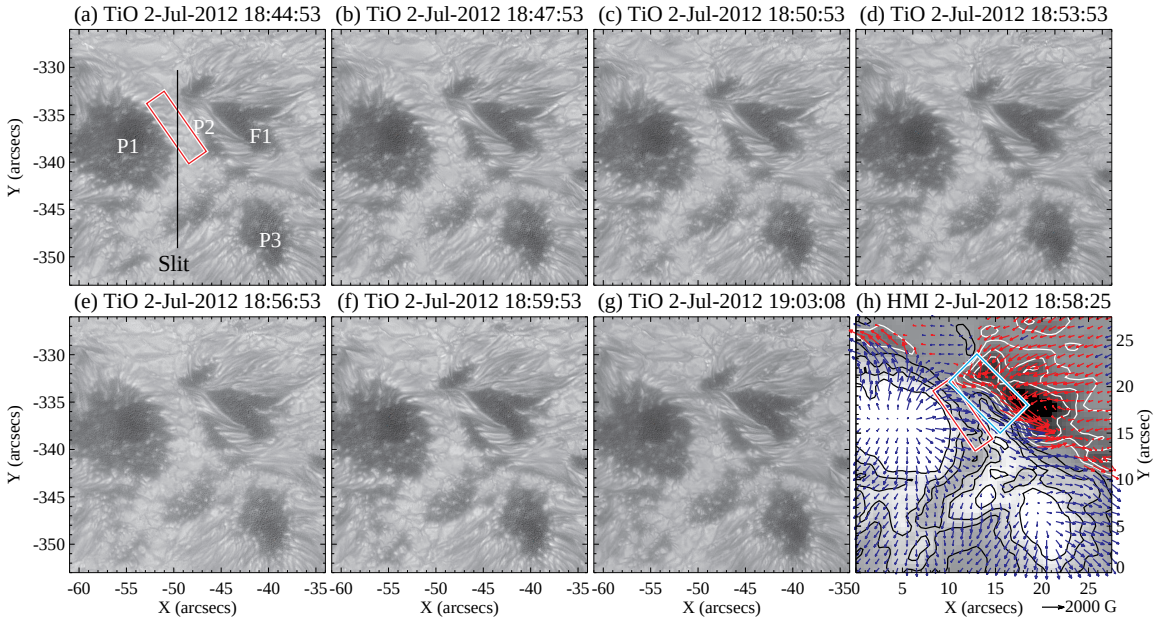

Figure 4.2 (a–g) Time sequence of NST TiO images from right before to right after the flare, showing the gradual formation of penumbra. A remapped HMI vector magnetogram with an approximately same FOV is plotted in (h). The contours of vertical field have the same levels with those in Figure 4.1 (e). The arrows represent horizontal magnetic field vectors. The red box overplotted on (a) and (h) is the region for which we calculate the temporal evolution of TiO intensity and horizontal magnetic field as shown in Figure 4.3 (b). The cyan box overplotted on (h) is the region for which we measure the temporal evolution of vertical magnetic flux as shown in Figure 4.3 (c). The black line in (a) is the slit using which we construct the time slices in Figure 4.4.

onset of the flare at 18:45 UT and reaches a nearly 20% lower level around 19:30 UT. At the meantime, the horizontal field starts to gradually increase from ∼18 UT but exhibits a highest increase rate (see the cyan line in (b)) simultaneously with the flare peak. Similar to our previous studies (e.g., Liu et al. 2005; Wang et al. 2012b), we believe that the rapid intensity darkening and horizontal field enhancement are resulted from the 3D magnetic field reconstruction due to the flare. The long-term gradual strengthening of the horizontal field, however, may be related to the overall evolution of the active region, i.e., the converging motion between P1/P2 and F1 as discussed below.

The spatial-temporal relationship of the formation of the new penumbra can be best seen in Figure 4.4, in which we show the time slice image along the slit as marked in Figure 4.2 (a). Before the flare, obvious convective pattern is present in the upper region (∼10–19″) with a time scale of 10–20 minutes and a spatial scale of about 1–2″, which are typical scales of granulation. After the flare, such a pattern is replaced by a typical penumbral structure with alternating dark and bright fibrils. It is also convincing that the transition from granulation to penumbrae is rapid and occurs right after the flare peak (the over-plotted solid line).

Since long-term evolution of magnetic field can provide hints for understanding the triggering of flares, we also examine in Figure 4.3 (c) the time profiles of magnetic flux within the cyan box in Figure 4.2 (h) that encompasses the main flaring PIL. We realize the difficulty in separating the short-term change in the smaller scale from the long-term change in the larger scale. Nevertheless, with the help of the accompanied magnetograph movie, there is some indication of magnetic cancellation in this region beginning from ∼18 UT, which reduces the positive flux with the highest cancellation rate (see the cyan line) co-temporal with the peak of the flare. The cancellation could be caused by the collision between P2 and the eastward motion of the emerging negative F1 field. However, it is also possible that such a reduction of positive flux

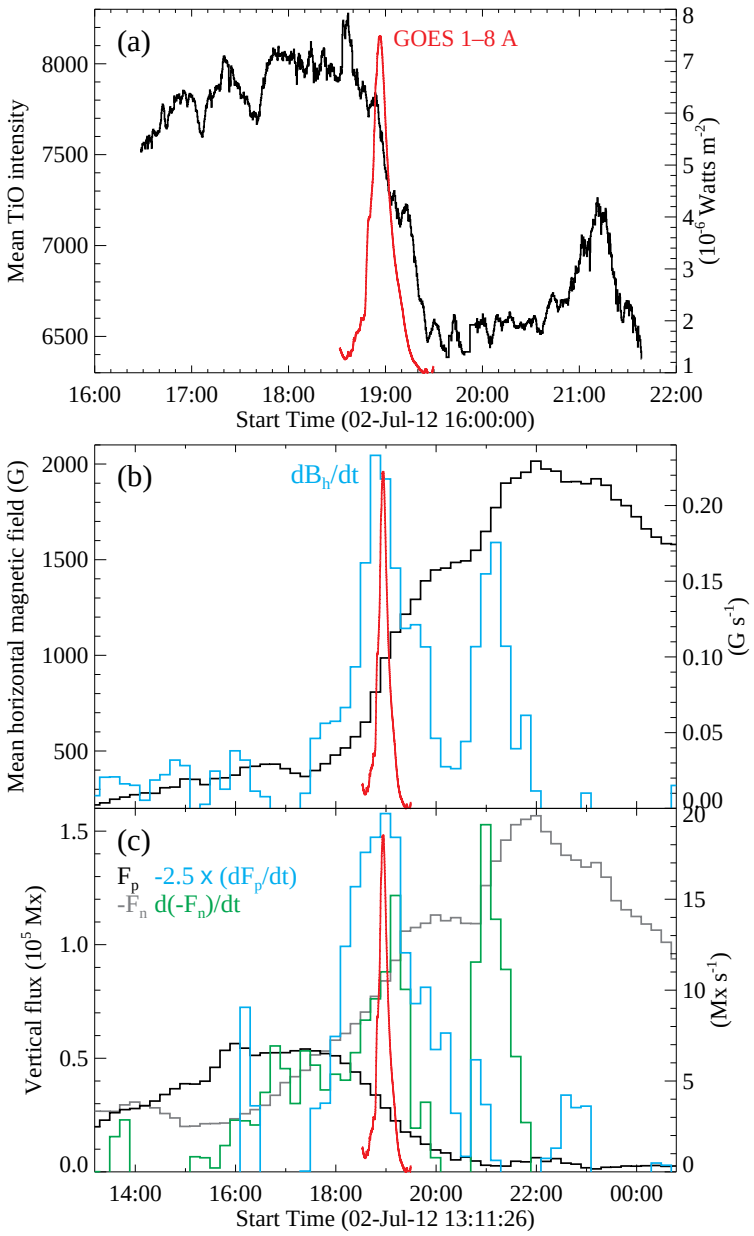

Figure 4.3 Temporal evolution of the mean TiO intensity (a) and horizontal magnetic field (b) within the red boxed region in Figures 4.2 (a) and (h), and the positive (F_p) and negative (F_n) magnetic fluxes (c) within the cyan boxed region in Figure 4.2 (h). The overplotted red line is the GOES 1–8 Å light curve for this flare. The colored lines in (b) and (c) are the temporal derivative of the corresponding quantities. Associated movie (movie-3-bl-bt.mpeg) shows the time sequence of longitudinal (left) and horizontal fields (right).

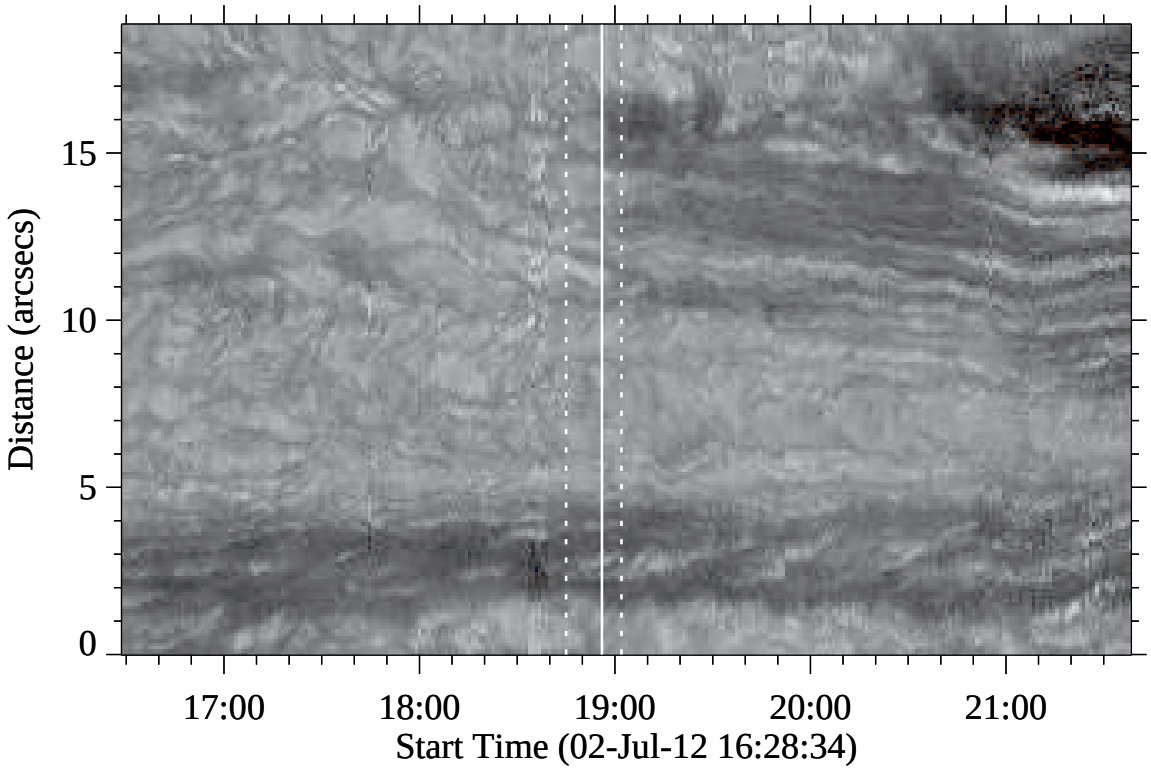

Figure 4.4 TiO time slices for the slit shown in Figure 4.2 (a). The distance is measured from the southern end of the slit. The dashed and solid lines denote the time of the start, peak, and end of the flare in GOES 1–8 Å.

is partially due to its southward migration. The evolution of negative field can not be used to identify the flux cancellation, as F1 is part of another larger scale flux emergence. The sharp increase of negative flux (see the green line) around the flare peak time is then due to the emerging flux moving into the calculation box. All these may be resulted from the interplay between the long-term and short-term magnetic restructuring, for which we presently can not draw a definite conclusion.

It is worth emphasizing two facts in our plots. First, a rapid change is only observed in the TiO intensity observed with NST. In contrast, all the HMI magnetic quantities have a more gradual change with an onset time even before the flare, although the sharp increase of the change rate is apparently associated with the flare. This could be attributed to the very different image scales of the two sets of observations and the long-term evolution of the entire active region in a large scale. Second, there is another peak in the field change rate around 21:15 UT, while we can not find any GOES X-ray signature around this time. After carefully examining the NST Hα data, we noted a sub-flare peaked at 21:16 UT, which has a similar morphology as the C7.4 flare. We speculate that the magnetic field as well as intensity changes are associated with this sub-flare.

4.3 Summary and Discussion

Taking advantage of the 0.″1 spatial resolution and 15 s cadence images of the NST, we observed in detail the rapid formation of a sunspot penumbra across the PIL closely associated with the 2012 July 2 C7.4 flare. The penumbral formation is unambiguously evidenced by the transformation from patterns of typical granulation to penumbral fibrils, and is accompanied with rapid TiO intensity darkening and horizontal field enhancement. The formation of this penumbra produces a larger scale δ sunspot. Such a fine-scale study is only possible with observations at sufficiently high resolution.

Based on the observational results, we propose the following interpretation. There could exist a low-lying flux rope right above the initially sheared PIL, which can be supported by sheared arcade fields. Some evidence of magnetic cancellation at this PIL and the filament eruption preceding the flare are consistent with the formation and eruption of the flux rope (e.g., Green et al. 2011). As the flux rope moves upward, the closing of the opened overlying fields are then pushed back toward the surface as a result of the downward momentum (Fisher et al. 2012). This leads to the formation of the new penumbra and the δ-spot configuration. Several supporting evidences for this scenario are as follows. (1) Sheared fields exist around the original PIL before the vertical fields cancel across it. (2) NLFFF extrapolation clearly shows both the flux rope and the overlying arcade fields. (3) Rising of the flux rope is visible in the Hα movie, and part of the bundle is apparent in the Hα blue-wing image in Figure 4.1 (b). (4) As shown in Hα images (Figures 4.1 (a) and (b)), the flare ribbons are not located beside the compact flaring PIL, but lie further apart in the main sunspots P1 and F1 that are finally connected by the newly formed penumbra. We also note that there are four homologous flares occurred during this period (17–22 UT). Each flare may have a partial contribution to the flux rope eruption but the C7.4 flare plays a major role. The penumbral formation is also only associated with this flare.

We emphasize that only high-resolution observing sequence would allow such a detailed examination of sunspot structure change. The size of the new penumbra is only about $5''$. Without these new NST observations, we might only conclude on the feature darkening near the flaring PIL as what have been described in our previous observations (e.g., Liu et al. 2005). The formation of new penumbra also signifies the downward push of fields due to Lorentz force change, as implied by the more horizontal field lines after flares (Hudson et al. 2008; Fisher et al. 2012). As soon as some horizontal fields subside close to the surface, the penumbra can be formed. The opposite process was also observed before (Wang et al. 2012a), in which the

peripheral sunspot penumbra may disappear suddenly after flares, so that convection in the granule scale appears immediately as the fields turn from horizontal to vertical state. In both cases, penumbra may be quite a thin layer of structure, as discussed by Wang et al. (2012a).

Although the study of larger scale flare activity is out of the scope of this study, it is worth mentioning that the present flare involves additional brightenings in other areas in the active region. In fact, by looking at Figure 4.1 (f), we find a magnetic field configuration favorable for circular-ribbon flares (e.g., Petrie & Sudol 2010). That is, positive field surrounds the central negative field, and the negative field also exhibits obvious motion. Indeed, during this flare, EUV images taken by the Atmospheric Imaging Assembly (AIA) show a semi-continuous circular ribbon in the outer positive field together with the more compact ribbon in the central negative field region. The two ribbons in Figure 4.1 as seen by NST represent part of the outer ribbon and most of the inner flare core. This circular flare picture is supported by the outward ejecting jets as clearly seen in the AIA movies. Flares having a circular ribbon have rarely been reported, although it is expected in the fan-spine magnetic topology involving reconnection at a 3D coronal null point (Masson et al. 2009; Reid et al. 2012; Wang & Liu 2012). It is speculated that the eruption of flux rope may have been triggered by the outer null-point reconnection (e.g., Jiang et al. 2013), which cause homologous jets as observed by AIA.

CHAPTER 5

STUDY OF SUNSPOT MOTION AND FLOW FIELDS ASSOCIATED WITH SOLAR FLARES

Study of evolution of sunspot structure and photospheric magnetic fields is important to understand how the flare energy is built up and released. With high-resolution data in optical wavelength, it is possible to examine in details the flows of the photosphere and their relationship to the flaring process. In this chapter[1], by using G-band and Stokes-V data obtained with Hinode Solar Optical Telescope (SOT), we study the sunspot motion and flow fields associated with the 2006 December 13 X3.4 flare in NOAA AR 10930. We calculate the centroids of the delta spot umbrae lying in opposite magnetic polarities, and use two different methods to derive the photospheric flow fields of the AR. We find that the shearing motion before the flare changes to unshearing motion associated with the eruption. A decrease of average velocity of shear flow in a magnitude of 0.2 km s^{-1} is found to be associated with the flare.

As a related study, we also test implementation of the recently developed differential affine velocity estimator for vector magnetograms (DAVE4VM; Schuck 2008) technique for the magnetic field observations obtained by the Big Bear Solar Observatory (BBSO) and Helioseismic Magnetic Imager (HMI) on board the Solar Dynamic Observatory (SDO).

5.1 Introduction

Evolution of sunspot structure and photospheric magnetic field associated with solar flares have recently drawn increasing attention. A sudden change of center-of-mass (CoM) separation of the two opposite polarities of a δ spot structure was found to

[1]This chapter is based on the following paper:
Wang, Shuo; Liu, Chang; Wang, Haimin, The Physics of Sun and Star Spots, Proceedings of the International Astronomical Union, IAU Symposium, 273, 412, 2011.

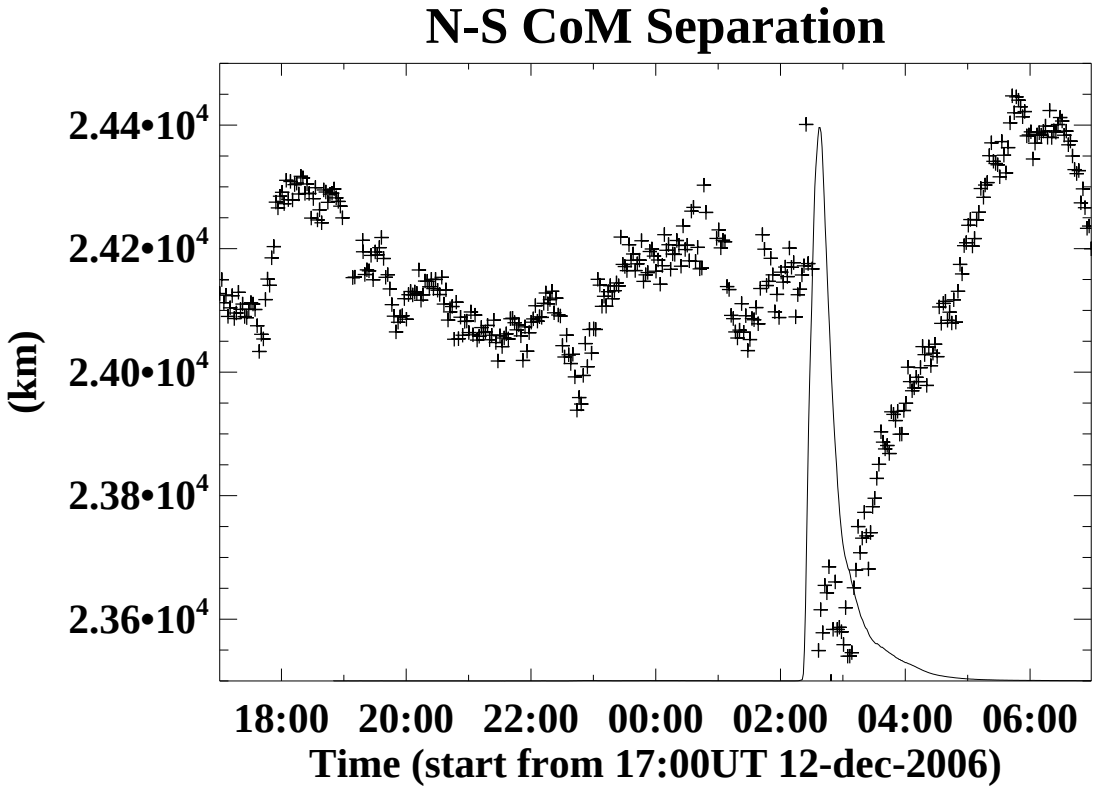

Figure 5.1 Time profile of CoM separation (pluses) in G-band intensity of NOAA AR 10930 between the northern (positive) and southern (negative) umbrae in the north-south direction, overplotted with GOES 1–8 Å soft X-ray light curve.

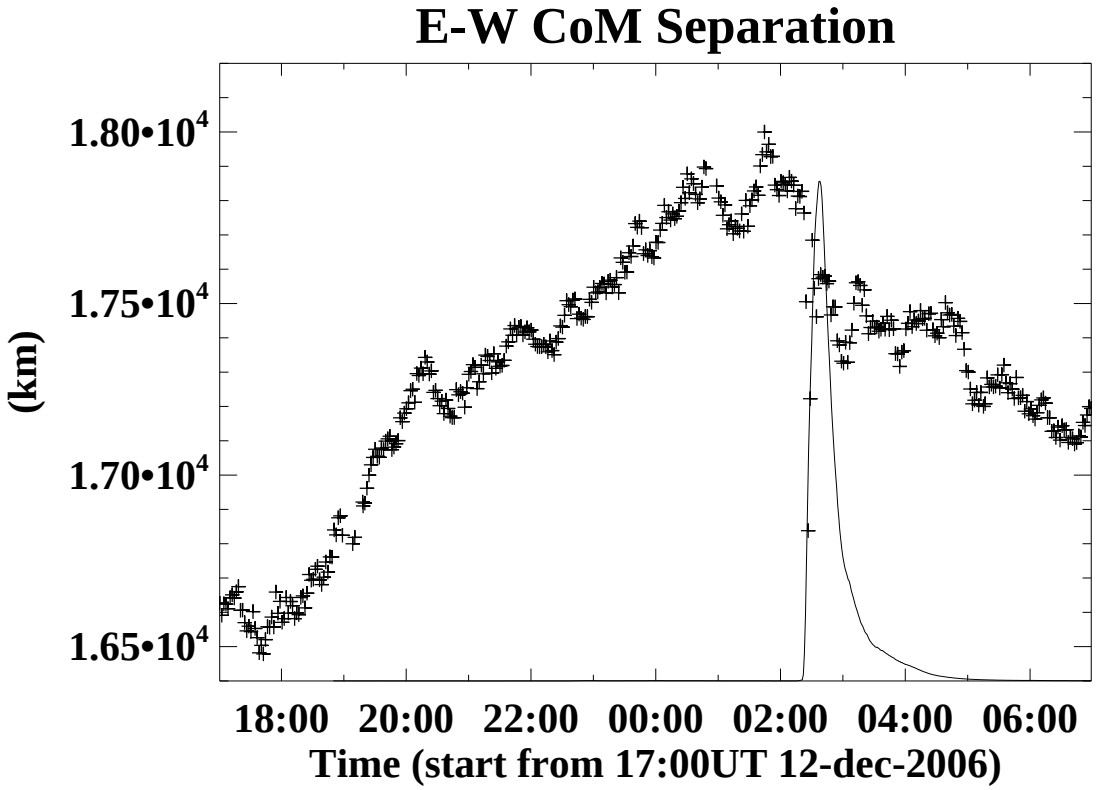

Figure 5.2 Time profile of CoM separation (pluses) in G-band intensity of NOAA AR 10930 between the northern (positive) and southern (negative) umbrae in the east-west direction, overplotted with GOES 1–8 Å soft X-ray light curve.

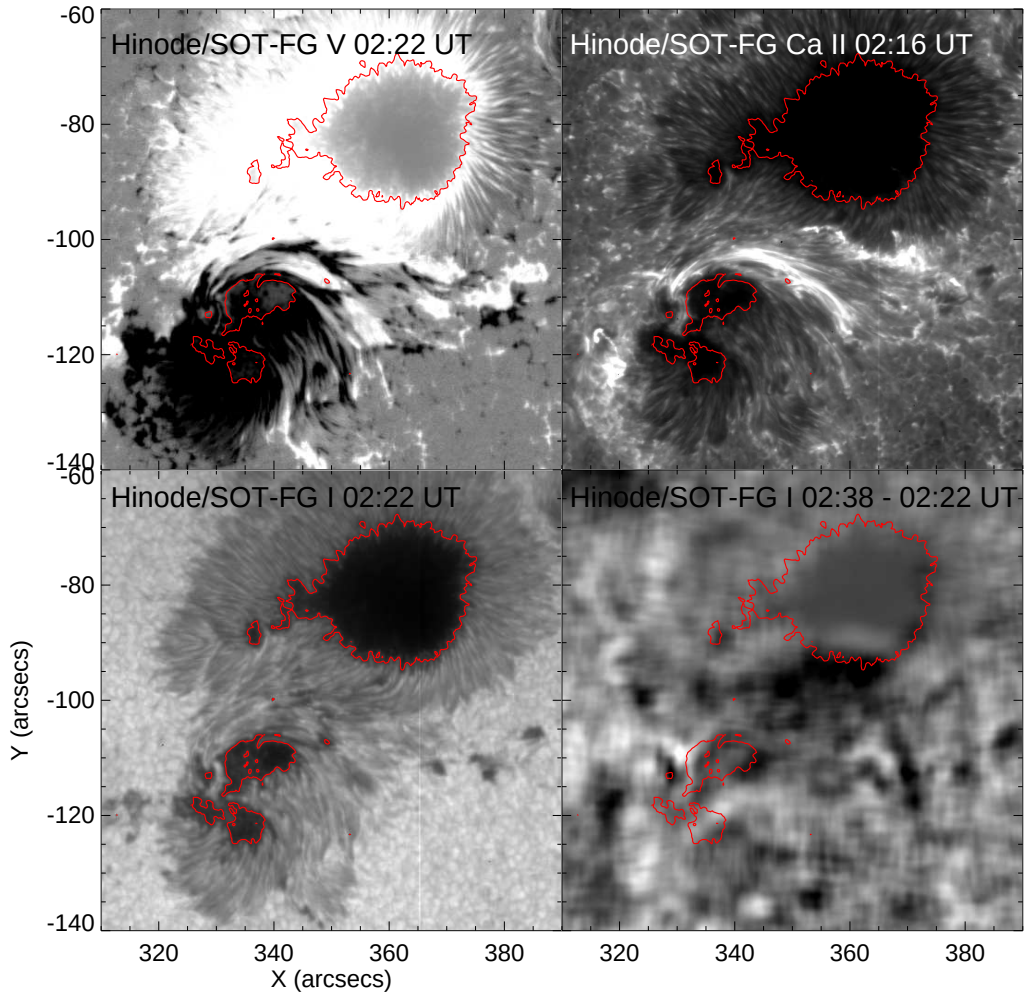

Figure 5.3 Hinode/SOT images for the X3.4 two-ribbon flare occurred in NOAA AR 10930 on 2006 December 13. Upper left panel: A LOS magnetogram at 02:22 UT. Upper right panel: A Ca II H image showing the flare ribbons. Lower left panel: A pre-flare G-band image. Lower right panel: A G-band difference image between post- and pre-flare states. Red contours show the position of umbral boundary.

be associated with large flares (Wang 2006). In the direction parallel to the magnetic PIL, the CoM separation always decreases, while in the direction perpendicular to the PIL, the CoM separation increases and decreases when the active region magnetic fields have a divergence and convergence motions, respectively. To further understand the variation of CoM separation of sunspots related to the flaring process, we investigated the high-resolution Hinode observations (Kosugi et al. 2007) to obtain the spot motion and flow fields associated with the 2006 December 13 X3.4 flare. Such a study can be greatly advanced with the aid of temporal evolution of the three-dimensional (3D) velocity fields of the source active region, which can now be achieved by the DAVE4VM (Schuck 2008) technique using vector magnetic field observations.

The DAVE4VM models motion of a vector of images with normal component of the ideal magnetic induction equation: $\partial_t B_z + \nabla_h \cdot (B_z V_h - V_z B_h) = 0$, where the plasma velocity V and the magnetic fields B are decomposed into a local Cartesian coordinate system with vertical direction along the z-axis and the horizontal plane, denoted generically by the subscript h, containing the x- and y-axes. Here we applied this method to NOAA AR 10365 on 2003 May 28 and NOAA AR 11057 on 2010 March 29, the latter of which belongs to the new solar cycle 24.

5.2 Data Sets and Analysis Methods

On 2006 December 13, an X3.4 two-ribbon flare occurred in NOAA AR 10930. Hinode fully covered this event, and we used G-band (430.5 nm) and Stokes-V (Fe I 630.2 nm) images obtained by its onboard SOT (Tsuneta et al. 2008). Active region flow fields from before to after the flare were derived and compared using both the DAVE (Schuck 2006) and Fourier LCT (Welsch et al. 2004) techniques.

Vector magnetograms of NOAA AR 10365 associated with an X3.6 flare on 2003 May 28 were taken by BBSO. For NOAA AR 11057 on 2010 March 29, magnetic field

observation was made by the state-of-the-art SDO/HMI. The 3D active region velocity fields of both active regions were derived using DAVE4VM. The initial test shows the promise that we will be able to carry out systematic studies of flare-related temporal evolution of photospheric flow field.

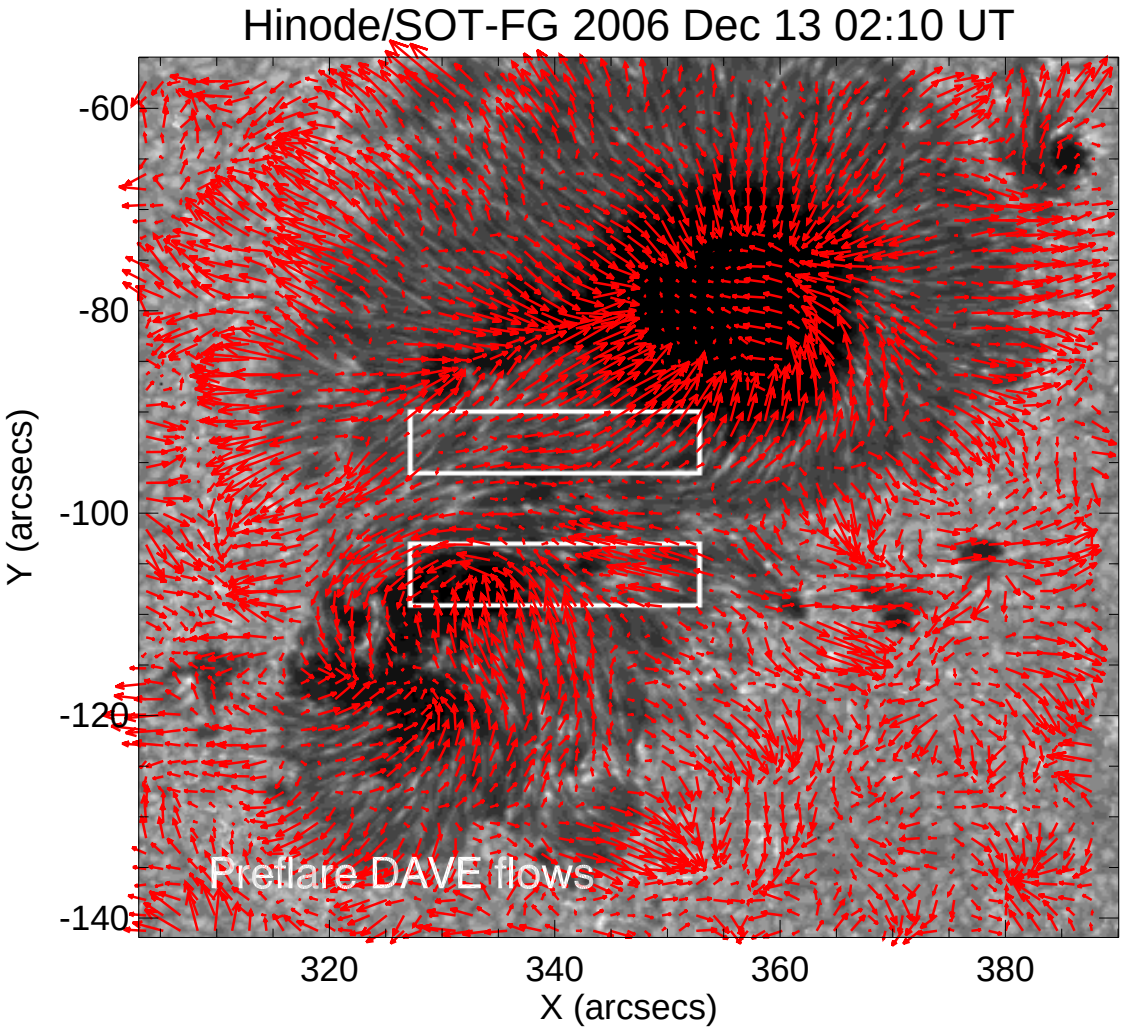

Figure 5.4 Flow fields for the pre-flare state derived using the DAVE method.

5.3 Results

Figures 5.1 and 5.2 show that the shearing motion of the two sunspots with opposite polarities of the δ configuration of NOAA AR 10930 changes to unshearing motion in the direction parallel to the PIL (east-west), which seems to be cotemporal with the

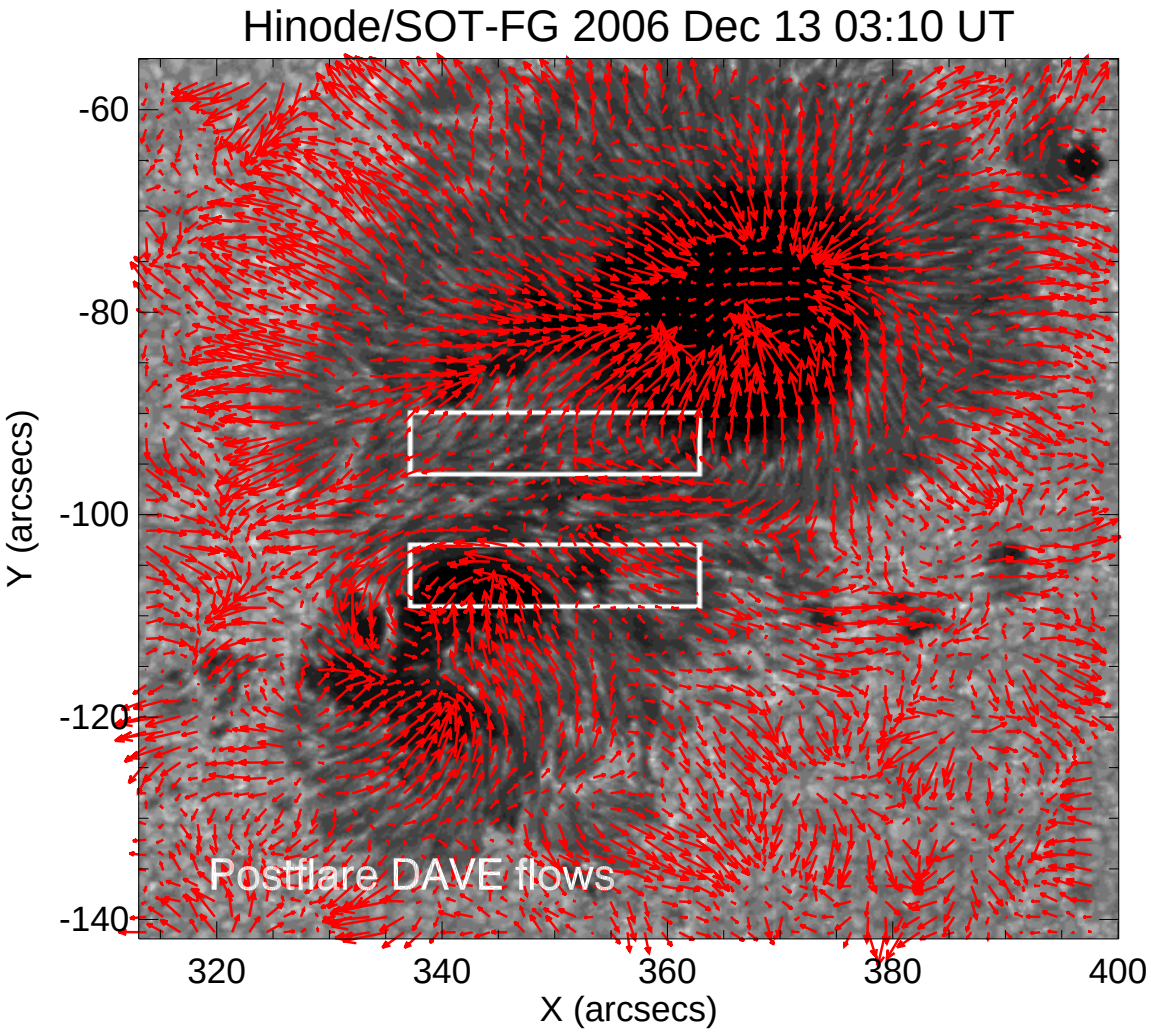

Figure 5.5 Flow fields for the post-flare state derived using the DAVE method.

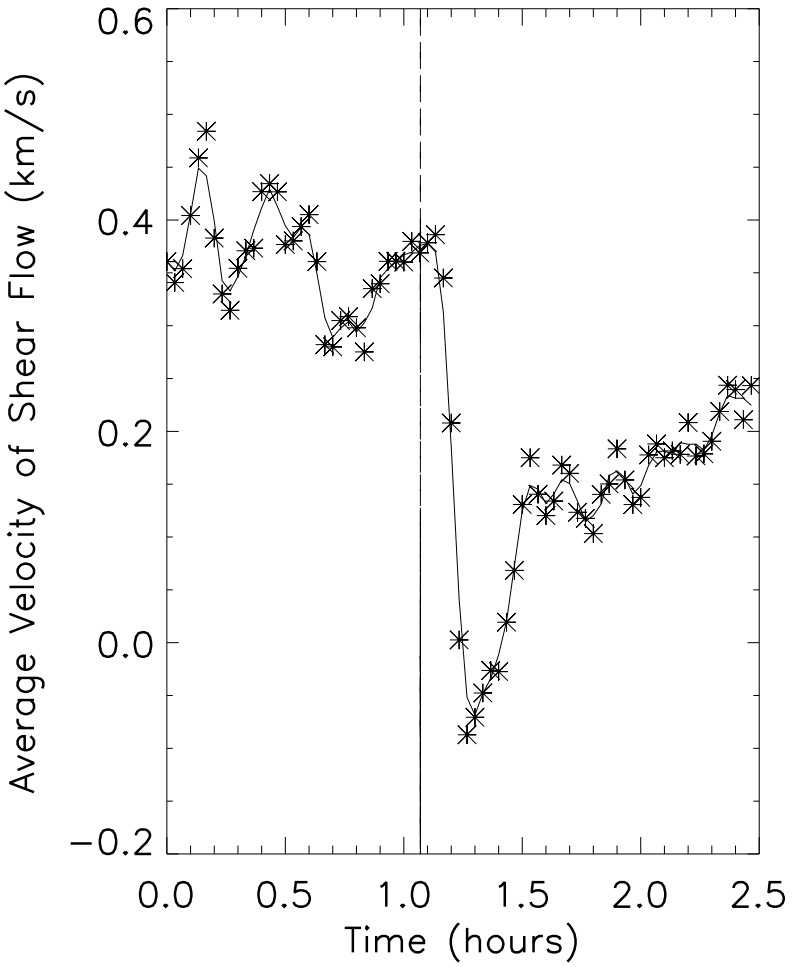

Figure 5.6 Time profile of shear flows calculated using the DAVE method as the difference of flows within the two boxed regions, and the start time is 1:10:40 UT 2006 December 13.

GOES-class X3.4 flare. In the lower right panel of Figure 5.3, the difference images in G-band intensity are taken immediately before and after the flare (post-flare 02:38:36 UT minus pre-flare 02:22:35 UT state), which reveals the enhancement (black) and decay (white) of sunspot structure that mainly occurred at penumbral regions. The enhancement and decay patterns appear to be consistent with the sudden change in the CoM separation. A Ca II image at 02:16 UT displayed in the upper right panel of Figure 5.3 shows the position of initial flare ribbons. The locations of penumbral decay and enhancement are related to flare emissions similar to previous studies (e.g., Liu et al. 2005). In Figures 5.4, 5.5, 5.7, 5.8, the white boxes denote the regions where the temporal evolution of the mean shear flow (curves with asterisks) is calculated. Overall, the DAVE method seems to produce more consistent results of flow field with the sunspot morphology. The decrease of average velocity of shear flow around the flaring PIL with a magnitude of 0.2 km s^{-1} is comparable to that obtained by Tan et al. (2009) using LCT method (0.3 km s^{-1}).

In Figure 5.10, we present the longitudinal magnetic field B_z of NOAA AR 10365 overplotted with the 3D DAVE4VM velocities associated with the occurrence of 2003 May 28 X3.6 flare. The horizontal flows are up to 6 km s^{-1}, and the contour levels for vertical flows are 0.1, 0.2, and 0.3 km s^{-1}. Enhancement of the 3D flow fields (i.e., diverging and vertical flows) seem to be spatially correlated with the flare around the same segment of the PIL. Note that these are mainly to test the implementation of the DAVE4VM technique on the ground-based magnetograph data. The observed flow signal during the flare may not be true as the magnetic field measurement can be seriously affected by flare emissions. Moreover, seeing variation can also contribute to about 1 km s^{-1} noise in the velocity measurement.

Figure 5.11 shows B_z of NOAA AR 11057 on 2010 March 29 overplotted with the 3D DAVE4VM velocities. The horizontal flow field exhibits super-penumbral flows corresponding to moving magnetic features, the magnitude of which is about

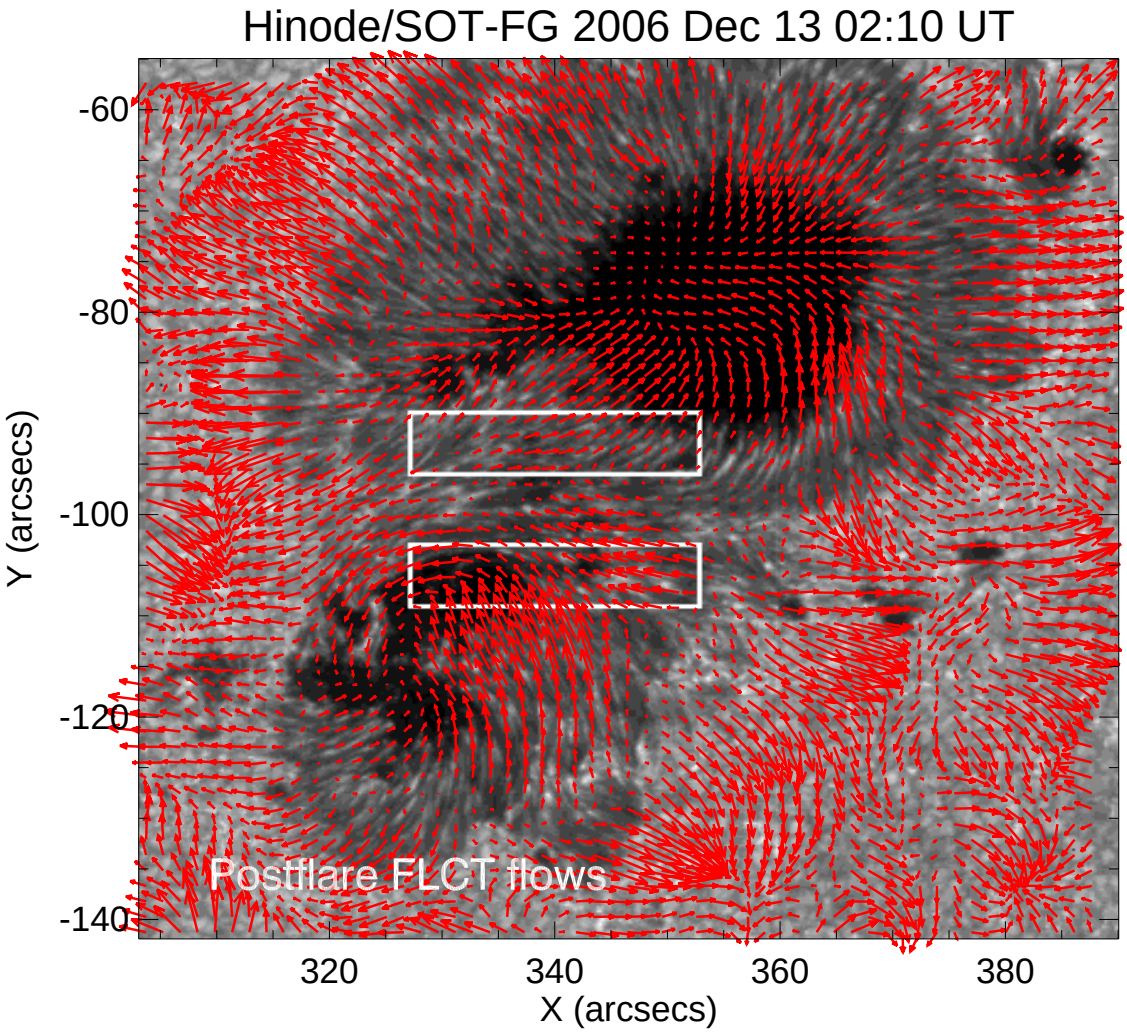

Figure 5.7 Flow fields for the pre-flare state derived using the FLCT method.

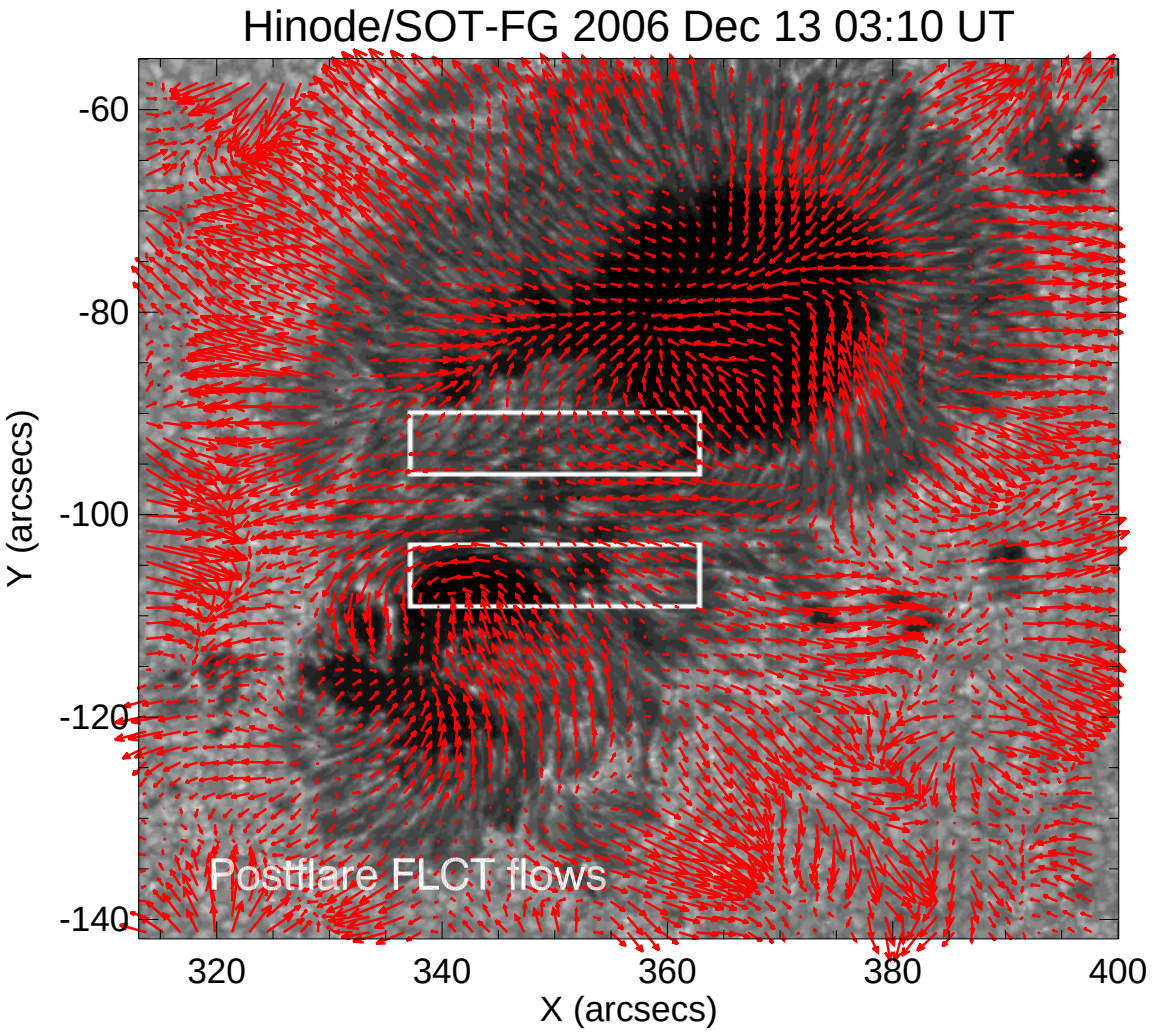

Figure 5.8 Flow fields for the post-flare state derived using the FLCT method.

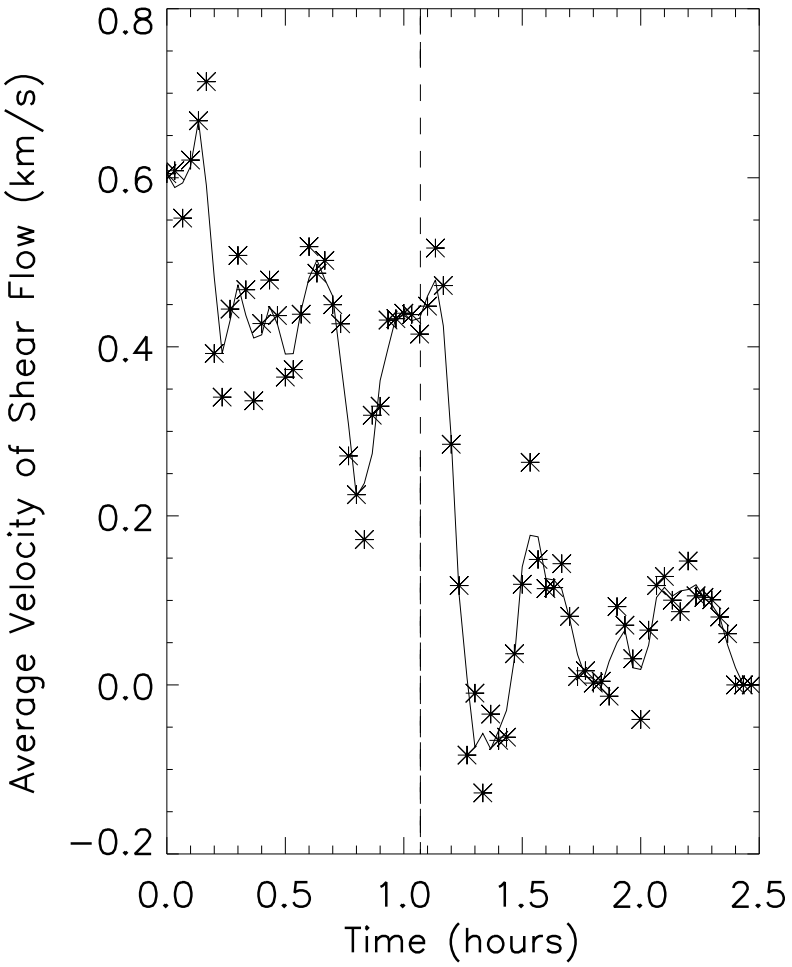

Figure 5.9 Time profile of shear flows calculated using the FLCT method as the difference of flows within the two boxed regions, and the start time is 1:10:40 UT 2006 December 13.

0.3 km s^{-1}, comparable to the results of Brickhouse & Labonte (1988) and Hagenaar & Shine (2005) .

5.4 Summary

Using Hinode G-band data spanning the X3.4 flare occurred in NOAA AR 10930 on 2006 December 13, we found a sudden change of shearing motion to unshearing motion between the two spots with opposite polarities after the flare. We obtained the flow fields with both DAVE and FLCT methods, and computed the evolution of shear flow around the flaring PIL. A gradual decrease of average velocity of the shear flow is found to be associated with the flare, with a magnitude of 0.2 km s^{-1}.

We obtained the 3D velocity field of NOAA AR 10365 on May 28, 2003 using DAVE4VM. Enhancement of 3D flow fields seem to be associated with the occurrence of an X3.6 flare. Note that these are mainly to test the implementation of the DAVE4VM technique on the ground-based magnetograph data. The observed flow signal during the flare may be affected by flare emissions as well as seeing variation.

DAVE4VM 3D velocity field of NOAA AR 11057 on 2010 March 29 was also derived using HMI vector magnetogram. This active region shows a horizontal super-penumbral flows corresponding to moving magnetic features, the magnitude of which is about 0.3 km s^{-1}. The vertical flow is smaller than 0.1 km s^{-1}.

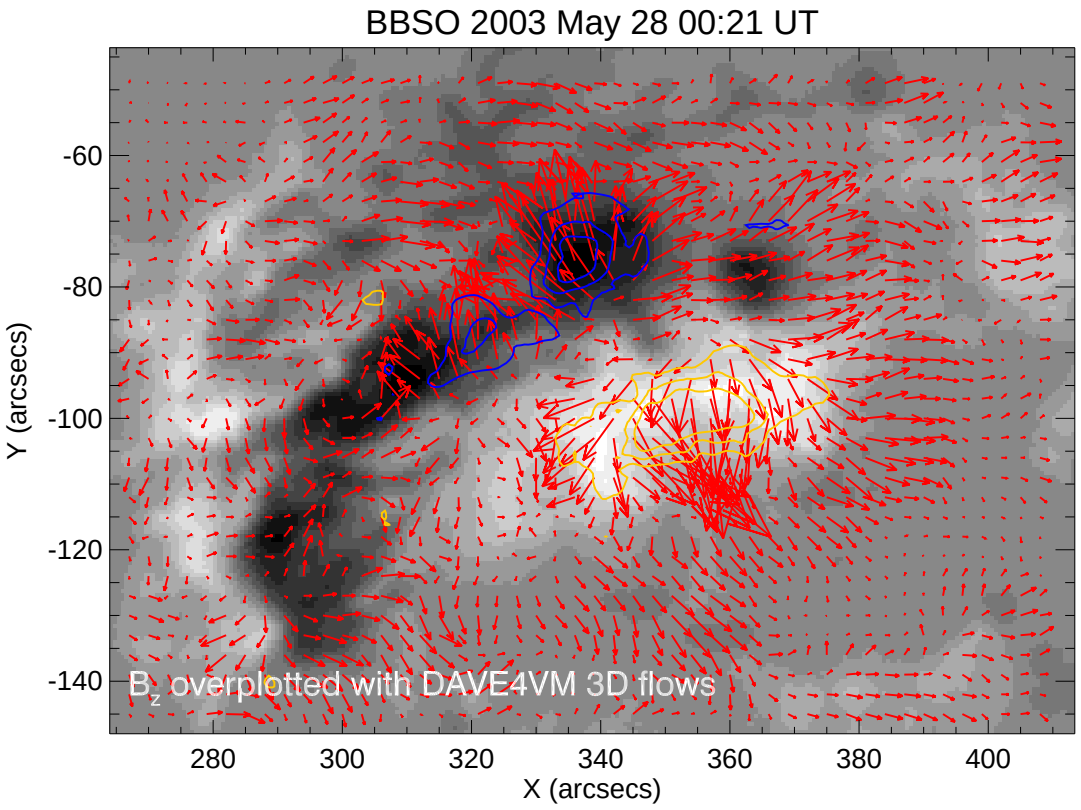

Figure 5.10 3D flow fields of NOAA AR 10365. Red arrows denote horizontal flows, and blue and yellow contours represent upflows and downflows, respectively.

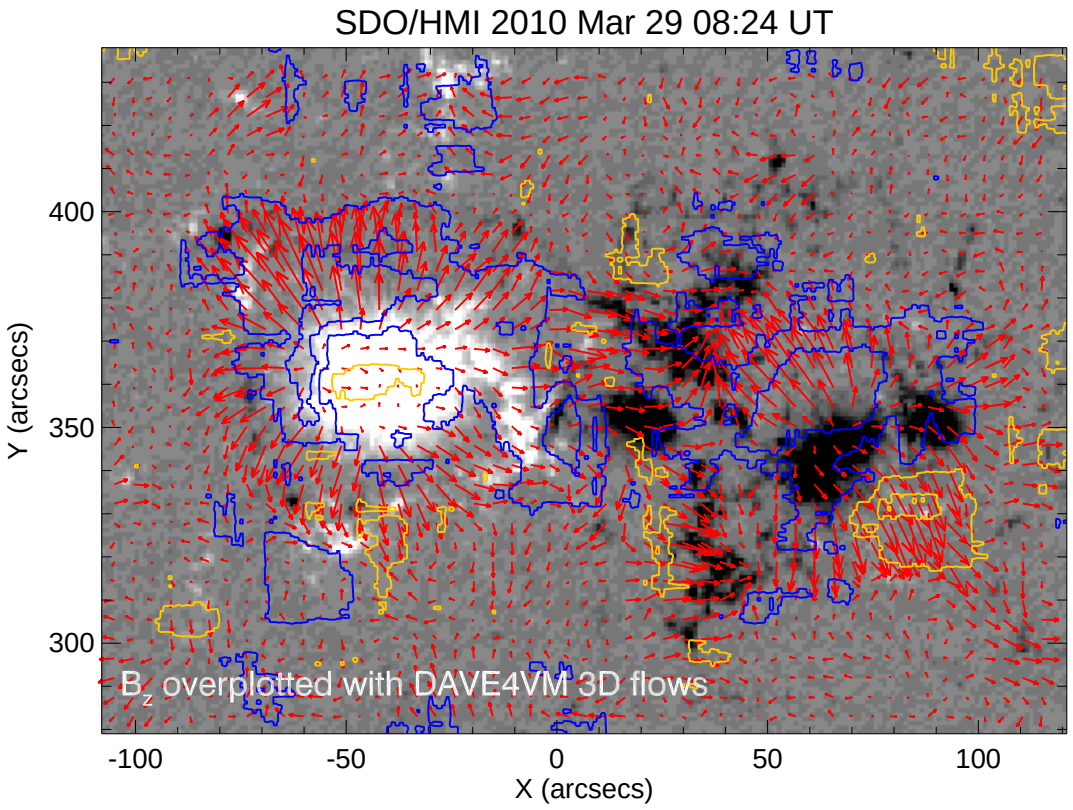

Figure 5.11 3D flow fields of NOAA AR 11057. Red arrows denote horizontal flows, and blue and yellow contours represent upflows and downflows, respectively.

CHAPTER 6

SUDDEN PHOTOSPHERIC MOTION AND SUNSPOT ROTATION ASSOCIATED WITH THE X2.2 FLARE ON 2011 FEBRUARY 15

The main objective of this chapter[1] is to study the sudden photospheric flow motion during the X2.2 flare on 2011 February 15. The Helioseismic and Magnetic Imager provides 45 s cadence intensity images and 720 s cadence vector magnetograms. These unprecedented high-cadence and high-resolution data give us a unique opportunity to study the change of photospheric flows and sunspot rotations associated with flares. By using the differential affine velocity estimator method and the Fourier local correlation tracking method separately, we calculate velocity and vorticity of photospheric flows in the flaring NOAA AR 11158, and investigate their temporal evolution around the X2.2 flare on 2011 February 15. It is found that the shear flow around the flaring magnetic PIL exhibits a sudden decrease, and both of the two main sunspots undergo a sudden change in rotational motion during the impulsive phase of the flare. These results are discussed in the context of the Lorentz-force change that was proposed by Hudson et al. (2008) and Fisher et al. (2012). This mechanism can explain the connections between the rapid and irreversible photospheric vector magnetic field change and the observed short-term motions associated with the flare. In particular, the torque provided by the horizontal Lorentz force change agrees with what is required for the measured angular acceleration.

6.1 Introduction

Besides the magnetic complexity and its evolution in flare productive active regions, the flow field is another important factor contributing to the energy storage and

[1]This chapter is based on the following paper:
Wang, Shuo; Liu, Chang; Deng, Na; Wang, Haimin, The Astrophysical Journal Letters, 782, L31, 2014.

release of solar eruptions. Martres et al. (1973, 1982) studied photospheric vortex motions, and found that they are correlated with the magnetic field evolution. Recently, rotating sunspots and other magnetic structures have been studied using space-borne observations with high spatial and temporal resolution. Brown et al. (2003) analyzed rotations of seven spots by examining feature movement on uncurled penumbral time-slices. The authors suggested that the rotation may be due to magnetic flux tube emergence. Anwar et al. (1993) observed rapid translational motion of a sunspot associated with the 1991 November 15 X1.1 flare, and suggested that the horizontal Lorentz force change can be sufficient to drive the sunspot motion. Closely related horizontal flow motion along the magnetic PIL was found in the photosphere and chromosphere by Harvey & Harvey (1976). Yang et al. (2004) analyzed photospheric shear flows in the NOAA AR 10486 and related them to the flare occurrence. Tan et al. (2009) found that the shear flow along the PIL dropped by 50% after a major flare. Beauregard et al. (2012) compared the flow field before and after the 2011 February 15 X2.2 flare, and revealed that the shear flow around the flaring PIL changed after the flare.

It is well known that the observed surface flow field is coupled to the evolution of the photospheric magnetic field. Rapid and permanent flare-related changes of magnetic fields on the photosphere in terms of magnetic shear were discovered by Wang (1992) and Wang et al. (1994). The change in the line-of-sight field component was also recognized (e.g., Wang et al. 2002; Spirock et al. 2002; Yurchyshyn et al. 2004; Sudol & Harvey 2005; Wang 2006; Petrie & Sudol 2010; Burtseva & Petrie 2013). Wang & Liu (2010) suggested that the vector magnetic field changes are mainly in the form of the horizontal field enhancement at flaring PILs. In the mean time, the permanent intensity change in the penumbral and umbral regions related to the magnetic field change was also revealed (Wang et al. 2004b; Deng et al. 2005; Liu et al. 2005; Chen et al. 2007; Jing et al. 2008; Wang et al. 2012a, 2013). Most recently,

the photospheric magnetic field change after flares was reconfirmed with space-based vector magnetogram observations (e.g., Liu et al. 2012; Wang et al. 2012b,c; Sun et al. 2012; Liu et al. 2013a). Wang et al. (2012b) found that there was a rapid enhancement of the horizontal magnetic field in a compact region along the PIL of the 2011 February 15 X2.2 flare. Petrie (2013) studied the azimuthal change of horizontal magnetic field in the main spots of this active region during the X2.2 flare, and further pointed out the co-spatial torsional Lorentz force change as well as the sheared Lorentz force along the PIL.

From the theoretical point of view, Hudson et al. (2008) used the vertical component of Lorentz force change to assess the back reaction of the coronal restructuring expected from a more horizontal photospheric magnetic field after flares. Fisher et al. (2012) formulated the changes of both the vertical and horizontal Lorentz forces implied by the observed changes of vector magnetic fields associated with flares, and further discussed the back reaction scenario using the principle of momentum and energy conservation. The idea of back reaction has already been reflected in some flare models. For example, the tether-cutting reconnection model for sigmoids (Moore et al. 2001) suggests two new flux loops associated with an eruption: a newly formed short loop that is pushed toward the surface, and an eruptive twisted long flux loop that carries the upward momentum. In the X2.2 flare, the former was manifested by the horizontal magnetic field enhancement on the surface (Wang et al. 2012b), and the latter was observed as a flux rope in corona that becomes part of the coronal mass ejection (CME) (Schrijver et al. 2011). There also exists some theoretical models that predict a sudden change in rotational motion of sunspots on the surface as a result of coronal transients. In the simulation of Fan (2009), the vorticity of the two spots at the feet of an emerging flux tube is enhanced in the same direction and with a similar magnitude for a short time, when coronal magnetic reconnection occurs during the flux emergence.

In this chapter, we focus on the sudden photospheric motions associated with the 2011 February 15 X2.2 flare. We scrutinize the sudden change in rotational motion of the two main sunspots and the shear flow variation close to the flaring PIL. The spatiotemporal changes of the horizontal Lorentz force are analyzed quantitatively, and our main goal is to examine the possible relationship between the observed sudden motions and the flare-related Lorentz force changes.

6.2 Observations and Data Processing

Intensity images from the HMI (HMI; Schou et al. 2012) on board the SDO were used to study the photospheric motions. The data with a pixel size of 0.5″ and a cadence of 45 s are reconstructed from the profile of Fe I absorption line at 6173 Å. The differential affine velocity estimator (DAVE; Schuck 2006) was applied to the HMI intensity images to derive the photospheric flow field. The DAVE method used combines the advection equation and a differential feature tracking technique to detect flows. We used a window size of 19 pixels according to former studies (e.g., Liu et al. 2013c), which is large enough to include structure information and small enough to have a good spatial resolution. The Fourier local correlation tracking method (FLCT; Fisher & Welsch 2008) was applied separately to confirm the result. The FLCT spatial windowing parameter σ was set to 7 pixels, corresponding to the same window size as in DAVE method. There are no optional parameters invoked in our use of FLCT. We also used the vector magnetograms supplied by the HMI team to investigate the vector field change. The vector data are derived from the observed Stokes parameters of the Fe I 6173 Å line. The Stokes parameters are inverted with the Very Fast Inversion of the Stokes Vector (Borrero et al. 2011). The 180° ambiguity is resolved using the minimum energy method (Metcalf 1994; Leka et al. 2009).

The flare started at 01:44 UT, peaked at 01:56 UT, and ended at 02:06 UT in GOES 1–8 Å flux. In order to study the sunspot rotation during the flare, regions

of interests (ROIs) are defined with a threshold of 1300 G of the vertical magnetic field strength. In intensity images, these ROIs correspond to the umbral region of the sunspots. We show in Figure 6.1 the ROIs marked with p and f, which correspond to the proceding and following spots, respectively. We also select other two ROIs marked as s1 and s2, which are two adjacent rectangular regions along the flaring PIL for the study of the shear flow. The change of horizontal Lorentz force $\delta\mathbf{F}_h$ was computed using the 12 minute cadence vector magnetograms. Fisher et al. (2012) formulated $\delta\mathbf{F}_h$ at and below the photosphere as a surface integral reduced from a volume integral by using the Gauss' theorem (Eq. 18 of Fisher et al. 2012):

$$\delta\mathbf{F}_h = \frac{1}{4\pi}\int_{A_{ph}} dA\delta(B_r\mathbf{B}_h) \ , \tag{6.1}$$

where B_r is the photospheric vertical field and $\mathbf{B}_h$ is the photospheric horizontal field. The torque ($\mathbf{T} = \mathbf{r}\times\delta\mathbf{F}_h$) of horizontal Lorentz force applied to the ROIs p and f can then be estimated, where the "center-of-mass" centroids of the ROIs are located based on the vertical magnetic field and are used as the rotation axis. We note that transient magnetic field changes could be induced by flare emissions (Patterson & Zirin 1981; Qiu & Gary 2003); however, we found no transient change of the horizontal magnetic field in this event.

6.3 Results

The preceding (p) and following (f) spots have positive and negative polarity, respectively. The flow map of the p spot before the X2.2 flare at 01:27 UT is presented in Figure 6.2(a). The spot generally rotates in the clockwise direction at an average speed of 0.2 km s^{-1} in its boundary region. During the flare, the speed increases to around 0.8 km s^{-1} at 01:51 UT as shown in Figure 6.2 (b). Thus the p spot rotates three times faster after the flare occurrence. The change of horizontal Lorentz force

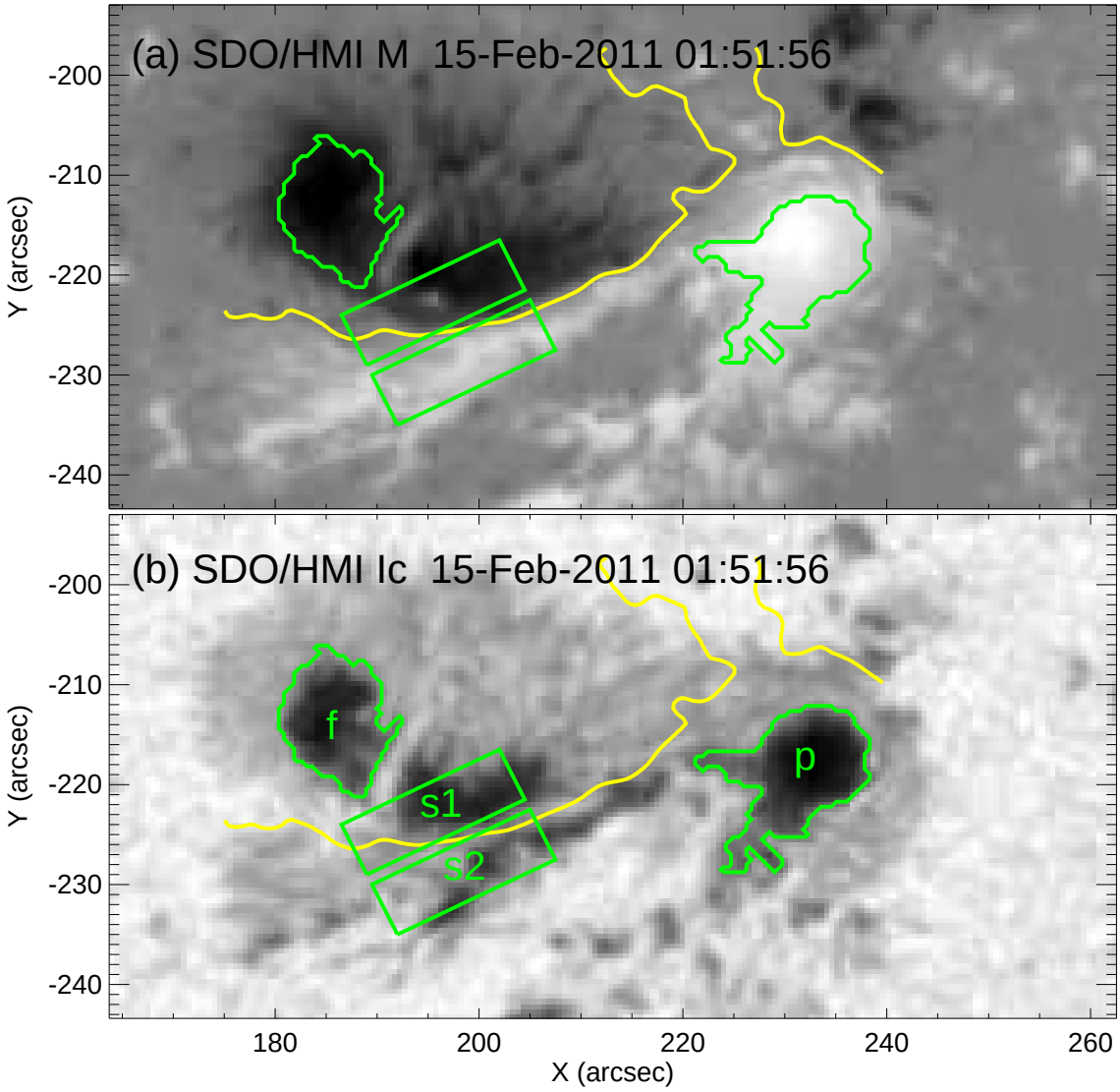

Figure 6.1 Maps of AR 11158 with regions of interest marked by green contours. (a) SDO/HMI line-of-sight magnetogram. (b) SDO/HMI intensity image. The yellow curve represents the main flaring PIL.

shown in Figure 6.2(c) indicates that the force acting on the volume at and below the photosphere during the flare is also in the clockwise direction, and may provide the driving force for the increased rate of spot rotation. Figures 6.2(d)–(f) display the maps of flows and Lorentz force in the f spot region, which show similar patterns of rotation and torque to those of the p spot. The centroid of the p(f) spot is marked with a green point in Figure 6.2(c(f)), and is used as the pivot to calculate the torque provided by the horizontal Lorentz force.

Based on the derived DAVE flow maps, we compute the flow vorticity at different times, and present the result in Figure 6.3. It can be seen that a negative vorticity dominates the umbral regions during the flare as shown in Figure 6.3(b), which is consistent with our flow tracking result that both the p and f spots undergo a sudden clockwise rotation during the flare.

We define the shear flow as the difference between the average velocity in the positive s2 and negative s1 regions in the direction parallel to the flaring PIL. The shear force is defined in a similar way based on the total Lorentz force in these regions. The shear force and the shear flow within the regions s1 and s2 (as denoted in Figure 6.1) are studied, and the result is shown in Figure 6.4(b). The shear flow is about 0.2 km s^{-1} before 01:53 UT. At ∼01:55 UT the shear flow suddenly reverses its direction. Then it recovers to about 0.1 km s^{-1} at ∼02:07 UT and remains roughly constant afterward. The fact that there is a 50% reduction of the shear flow after the flare is similar to the event studied by Tan et al. (2009). The sudden shear flow decrease is co-temporal with a $\sim 2.9 \times 10^{22}$ dyne of shear force, which is in the direction opposite to that of the initial shear flow. The shear force is close to zero at non-flaring periods. Therefore, the sudden decrease of shear flow speed is likely related to the horizontal Lorentz force.

Figure 6.4(c) shows the time profiles of rotational speed and torque of the preceding spot p. It rotates at about 6° hr^{-1} clockwise before the flare. At ∼01:49 UT,

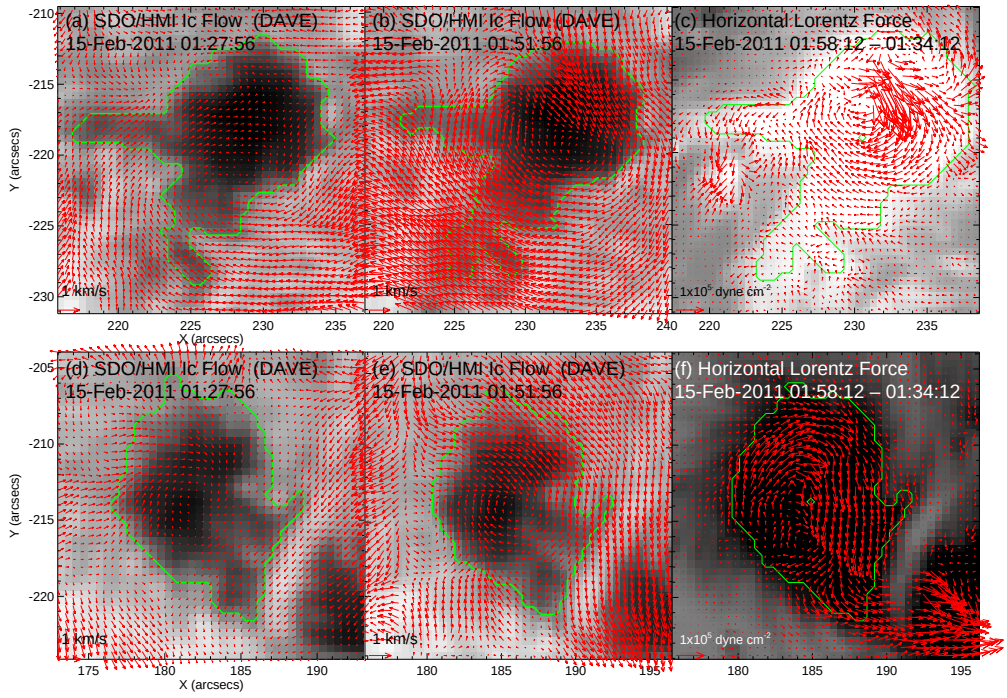

Figure 6.2 DAVE flow maps of the region p before (a) and during (b) the flare. The change of horizontal Lorentz force during the flare is plotted in (c). DAVE flow maps of the region f before (d) and during (e) the flare. The change of horizontal Lorentz force during the flare is plotted in (f). The centroid of the p(f) spot is marked with a green point in (c(f)). To show the rotational motion better, the background constant translational motion is subtracted in the flow maps.

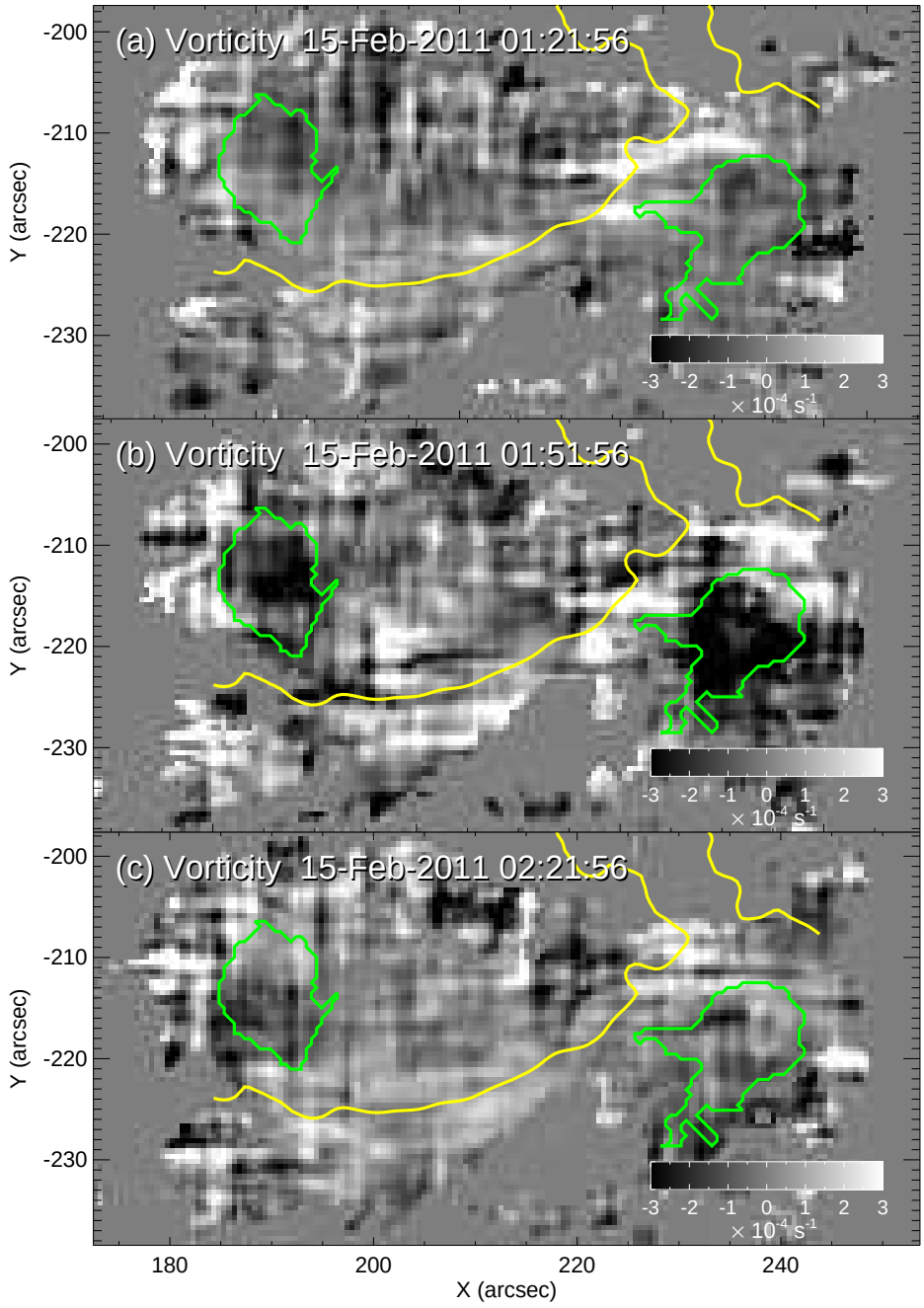

Figure 6.3 Vorticity maps based on DAVE flows tracked based on SDO/HMI intensity images at different times. The sudden enhancement of negative vorticity in the sunspot areas (green contours) are co-spatial and co-tempoal with the flare.

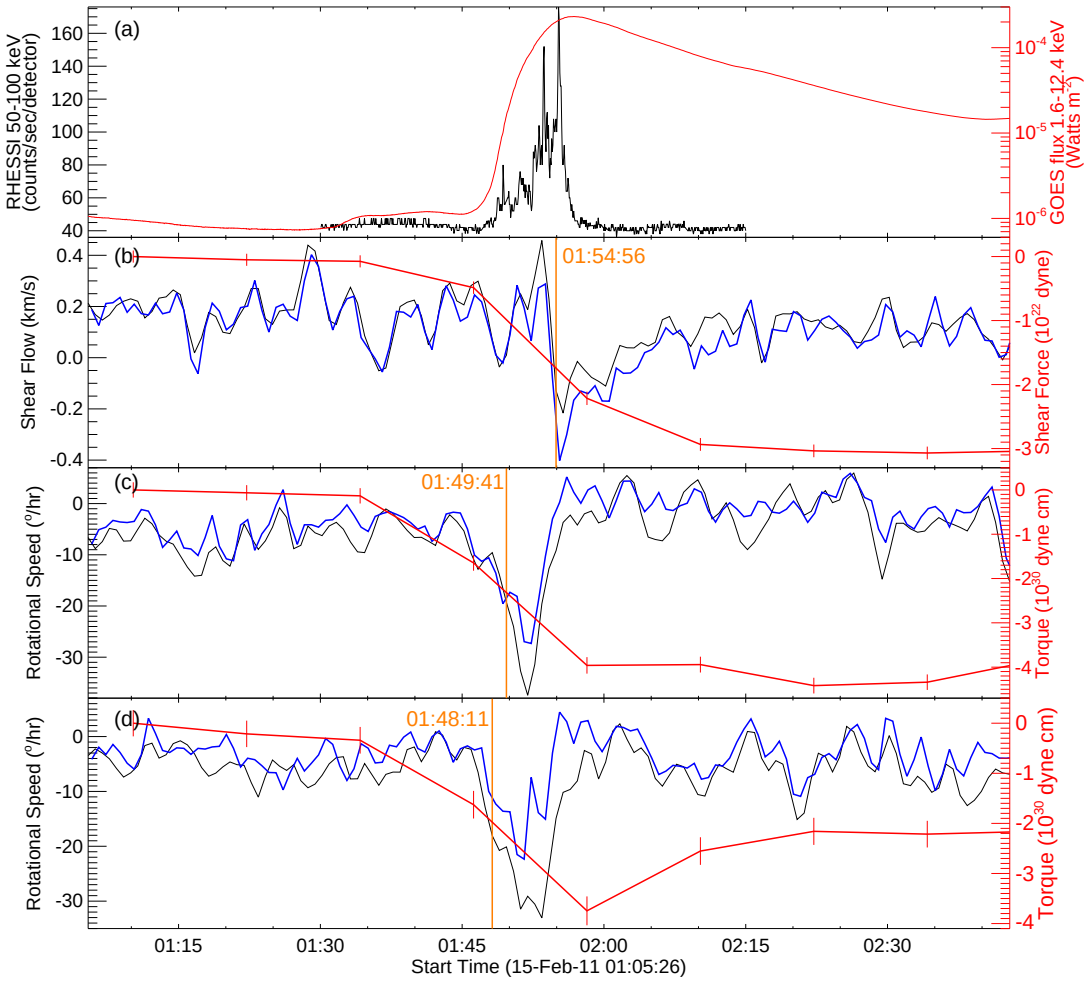

Figure 6.4 Temporal evolution of the sudden motions. (a) The black curve represents RHESSI 50–100 keV HXR light curve. The red curve shows the GOES 1.6–12.4 keV flux. (b) Time profiles of the shear flow near PIL. The black and blue curves represent the mean velocity of the shear flow derived by DAVE and FLCT, respectively. The red curve shows the change of horizontal Lorentz force. (c) and (d) display the time profiles of the regions p and f, respectively. The black curves give the vorticity derived using DAVE flows, while the blue curves are from the FLCT result. The red curves show the torque provided by the change of horizontal Lorentz force. The orange vertical lines marked with time show the starting time of the sudden shear motion and rotations. The error bars of red curves indicate a 3σ level.

the rotational motion accelerates, and the angular speed reaches 37° hr^{-1} clockwise at ∼01:52 UT. The rotational speed then decreases to ∼1° hr^{-1} clockwise in ∼5 minutes. This sudden motion results in about 3° clockwise rotation within 8 minutes. As a comparison, Jiang et al. (2012) reported that several features on the outer edge of the penumbra of the p spot undergo a clockwise rotation from 20 hr before the flare to 1 hr after flare, with a speed of 1.8–5.1° hr^{-1}. Although we use a different method, our results are consistent with this previous study. The temporal evolution of the following spot f is displayed in Figure 6.4(d). The start time of the sudden clockwise rotation is ∼01:48 UT, and the angular speed reaches maximum at ∼01:51 UT co-temporal with the occurrence of the maximum torque. The overall property of the f region is similar to that of the p region. It is noticeable that the torque is only present during the flare, and hence it is likely responsible for the above sudden change in rotational motions during the flare.

Our observational results suggest that the horizontal Lorentz force is the driving force of the sudden photospheric motion. Specifically, the rotational speed of p and f spots increases 27° hr^{-1} in 225 s and 315 s, which results in an angular acceleration α of 5.8×10^{-7} rad s^{-2} and 4.2×10^{-7} rad s^{-2}, respectively. In the s1 and s2 regions, the shear flow changes 0.4 km s^{-1} in 45 s, which corresponds to an acceleration of 1×10^3 cm s^{-2}. As a more quantitative analysis, we compare these observed acceleration with those derived based on the measured torque T due to the change of Lorentz force. For the spots p and f, we assume a geometry of rigidly rotating disk, for which $T = I\alpha$ and the moment of inertia $I = \frac{1}{2}\rho\pi hr^4$, where the density $\rho \approx 4 \times 10^{-7}$ g cm^{-3}, depth $h \approx 250$ km (density scale height at the photosphere), and radius $r \approx 10''$. Since the measured $T \approx 3.9 \times 10^{30}$ (2.5×10^{30}) dyne cm for the p (f) spot at 02:10 UT, the torque can produce an α of 8.8×10^{-7} (5.7×10^{-7}) rad s^{-2}, which is roughly comparable with the observation. Similarly, for the rectangular regions s1 and s2 (about 18″ by 12″) with an estimated mass $m \approx 1.1 \times 10^{19}$ g, the

measured shear force $\delta F_h = 2.9 \times 10^{22}$ dyne at 02:10 UT would cause an acceleration $\delta F_h/m \approx 2.6 \times 10^3$ cm s^{-2}, which is also close to the observed acceleration. These results are summarized in Table 6.1. We caution that there is a large uncertainty in our calculation, which presumes a density scale height as the coherent depth of the rotational motion. Nevertheless, the acceleration due to the Lorentz force change is within the right order of magnitude to explain the observed changes in the rotation rate of spots and the shearing speed near the PIL.

We further compare the initiation time of the sudden motions in different regions. The two spots p and f start the sudden rotation at almost the same time at ∼01:48 UT, while the sudden decrease of the shear flow occurs at ∼01:55 UT, i.e., 7 minutes later. Interestingly, the flare hard X-ray emission up to 100 keV has a first minor peak around 01:48 UT and has a main peak at 01:55 UT (see Figure 6.4(a)), the latter of which could be co-temporal with the peak of CME acceleration (Temmer et al. 2008). Therefore, this time gap of the above sudden motions might reflect the different response time of the different photospheric regions to the coronal field restructuring. Specifically, we surmise that the sudden change of the rotational motion of the sunspots at the feet of the flux rope could represent an immediate response to the flux rope eruption. In contrast, the delayed sudden shear flow change in the central flaring region could indicate a later effect of the magnetic field implosion process accompanying the rapid CME acceleration (e.g., Li et al. 2011).

6.4 Summary and Discussion

Using SDO/HMI intensity images with a high spatiotemporal resolution, we have carried out a detailed analysis of the evolution of photospheric flows associated with the 2011 February 15 X2.2 flare. We used the concept of vorticity to examine the flare-related sudden change in rotational motion of sunspots, which was considered difficult to measure. We have also investigated the sudden change of the shear flow

Table 6.1 Comparison of Acceleration of Photospheric Regions

	α in p region	α in f region	acceleration in s1 & s2 regions
DAVE observed	5.8×10^{-7} rad s^{-2}	4.2×10^{-7} rad s^{-2}	1×10^{3} cm s^{-2}
Estimated from δF_h	8.8×10^{-7} rad s^{-2}	5.7×10^{-7} rad s^{-2}	2.6×10^{3} cm s^{-2}

around the flaring PIL. These results are discussed in the context of the change of the horizontal Lorentz force derived from SDO/HMI vector magnetograms. The main results are summarized as follows.

1. The two sunspots at the feet of the erupting flux rope show sudden acceleration of rotational motion during the flare. The fast clockwise rotation lasts ∼5 minutes and reaches a peak angular speed of ∼30° hr^{-1}.

2. The region around the flaring PIL shows a sudden decrease of the shear flow velocity after the onset of the flare. The shear flow changes ∼0.4 km s^{-1} within 1 minute, and recovers to 0.1 km s^{-1} (half of the preflare value) in ∼10 minutes. The region is co-spatial with the horizontal magnetic field enhancement as studied in Wang et al. (2012b).

3. The horizontal Lorentz force may be the driving force of the sudden motions in the photosphere. The direction, magnitude, and spatiotemporal distribution of the force and the motion are consistent. The change of horizontal Lorentz force in the sheared regions is $\sim 3 \times 10^{22}$ dyne, and the torque in each of the sunspot region is $\sim 3 \times 10^{30}$ dyne cm. The change of Lorentz force provides the needed torque to drive such sudden motions.

A major result is that we reveal, for the first time, that the rotational speed of sunspots suddenly changes about 4 minutes after the onset of the X2.2 flare, and that this motion could be driven by the change of the horizontal Lorentz force exerted on the photosphere. We note the simulation of Fan (2009), in which the vorticity of two spots with opposite polarities and rotating in the same direction could be enhanced in that direction with a similar magnitude, when a coronal magnetic reconnection occurs during the emergence of the flux tube. In our study, the results of the X2.2 flare show a similar vorticity change in the regions of the two main sunspots with opposite polarities, which is co-temporal with the first minor hard X-ray peak soon after the

flare initiation. We speculate that this rotational change of sunspots represents an immediate response to the flux rope eruption. Also notably, the sudden change of the shear flow in the central flare region occurs 7 minutes after the sunspot rotational change. The shear flow change is co-temporal with the main peak of the hard X-ray emission and CME acceleration. As momentum conservation implies that the upward impulse exerted on the erupting CME must be balanced by a downward impulse acting on the surface, it might be possible that the delayed shear flow change at the flare core region is a manifestation of the response of the low atmosphere to the magnetic field implosion. Obviously, studies of more events are needed in order to provide further observational evidence for the impact of coronal field restructuring on the photosphere.

As a final note, Zharkov et al. (2011, 2013) discussed the properties of seismic sources of this event. It is interesting that the two sources are not located at the strong HXR sources near s1 and s2; instead, they are associated with two remote locations near the edge of p and f sunspots, where HXRs are hardly detected. The authors used the erupting flux rope model to explain the observations. We speculate that the sudden change in horizontal sunspot rotation may be associated with these two seismic sources.

CHAPTER 7

A SOLAR ERUPTION DRIVEN BY RAPID SUNSPOT ROTATION

In this chapter[1], the observation of a major solar eruption associated with fast sunspot rotation is presented. The event includes a sigmoidal filament eruption, a coronal mass ejection, and a GOES X2.1 flare from NOAA active region 11283. The filament and some overlying arcades were partially rooted in a sunspot. The sunspot rotated at $\sim 10^{\circ}$ per hour rate during a period of 6 hours prior to the eruption. In this period, the filament was found to rise gradually along with the sunspot rotation. Based on the HMI observation, for an area along the PIL underneath the filament, we found gradual pre-eruption decreases of both the mean strength of the photospheric horizontal field (B_h) and the mean inclination angle between the vector magnetic field and the local radial (or vertical) direction. These observations are consistent with the pre-eruption gradual rising of the filament-associated magnetic structure. In addition, according to the Non-Linear Force-Free-Field reconstruction of the coronal magnetic field, a pre-eruption magnetic flux rope structure is found to be in alignment with the filament, and a considerable amount of magnetic energy was transported to the corona during the period of sunspot rotation. Our study provides evidences that in this event sunspot rotation plays an important role in twisting, energizing, and destabilizing the coronal filament-flux rope system, and led to the eruption. We also propose that the pre-event evolution of B_h may be used to discern the driving mechanism of eruptions.

[1]This chapter is based on the following paper:
Ruan, Guiping; Chen, Yao; Wang, Shuo; Zhang, Hongqi; Li, Gang; Jing, Ju; Su, Jiangtao; Li, Xing; Xu, Haiqing; Du, Guohui; Wang, Haimin, The Astrophysical Journal, 784, 165, 2014.

7.1 Introduction

Solar eruptions, including solar flares, coronal mass ejections (CMEs), and filament eruptions, are spectacular energy release phenomena that occur in the solar atmosphere. They often lead to catastrophic impacts on the near-Earth space environment. They are generally believed to be a result of the rapid release of magnetic energy stored in highly-stressed/twisted magnetic structures of the corona (e.g., Forbes 2000; Low 2001). The magnetic energy is transported into the corona via slow photospheric footpoint motions, e.g., emergence, shearing, twist, etc., in a relatively long period of time, comparing to the time scale of an eruption. Among various forms of photospheric motions, sunspot rotation, first observed a century ago by Evershed (1910), has been considered to be an important process and has been studied extensively (e.g., Stenflo 1969; Barnes & Sturrock 1972; Ding et al. 1977, 1981; Amari et al. 1996; Tokman & Bellan 2002; Török & Kliem 2003; Brown et al. 2003; Régnier & Canfield 2006; Yan & Qu 2007; Yan et al. 2008b,a, 2009; Su et al. 2010).

Previous studies confirmed the important role played by sunspot rotation in transporting energy and helicity from below the photosphere into the corona with quantitative calculations (e.g., Kazachenko et al. 2009; Vemareddy et al. 2012), and revealed some temporal and spatial association of sunspot rotation with solar flares on the basis of observational data analysis (e.g., Zhang et al. 2007, 2008; Yan & Qu 2007; Yan et al. 2008b,a, 2009; Jiang et al. 2012). There also exist a number of magnetohydrodynamic (MHD) studies examining the consequence of twisting a flux rope structure which is confined by overlying magnetic arcades (e.g., Amari et al. 1996; Török & Kliem 2003). In a latest study, Török et al. (2013) examined the role of twisting the overlying arcades in the onset of a CME using a flux rope model. These studies showed that the CME can be triggered by twisting either the core flux rope structure or the overlying coronal fields, thus established the importance of sunspot

rotation in the eruption process from a theoretical perspective. On the other hand, observational studies connecting sunspot rotation with CMEs remain elusive.

Here we present a case study of the evolution of a sigmoidal filament which has roots in a rotating sunspot. The study, involving multi-wavelength imaging and vector magnetic field data from the SDO, provides a rare case revealing the role of sunspot rotation being as not only a general energy transport process but also a direct driving process that leads to the eventual flare, CME, and filament eruption.

7.2 Observation

We analyzed the multi-wavelength imaging data provided by the Atmospheric Imaging Assembly (AIA; Lemen et al. 2012) and the vector magnetic field and continuum intensity data by the Helioseismic and Magnetic Imager (HMI; Schou et al. 2012) on board the SDO spacecraft for the NOAA active region (AR) 11283 between 2011 September 3 and September 8. The AR was located N14W15 at 16:00 UT on September 6, close to the disk center. AIA observes the Sun in 10 different wavebands, covering a wide range of temperatures and reveals physical processes at various layers of the solar atmosphere. The data are taken with a pixel size of $0.6''$ and 12s cadence. For our study, we only analyze the AIA observations at the 304 Å (HeII, T$\sim$ 0.05 MK) to follow the dynamics of the cool filament and the 94 Å (FeXVIII, T$\sim$6.3 MK) observation to trace the hot eruptive structures. The processed disambiguated HMI vector magnetic field data are of 12-minute cadence at a $0.5''$ pixel resolution, provided by the HMI team (see ftp://pail.stanford.edu/pub/HMIvector2/movie/ar1283.mov for the corresponding movie). These vector magnetogram data have been de-rotated to the disk center, and remapped using a Lambert equal area projection (Calabretta & Greisen 2002; Thompson 2006). The field vectors are then transformed to Heliographic coordinates with projection effect removed (Gary & Hagyard 1990; Sun et al. 2012).

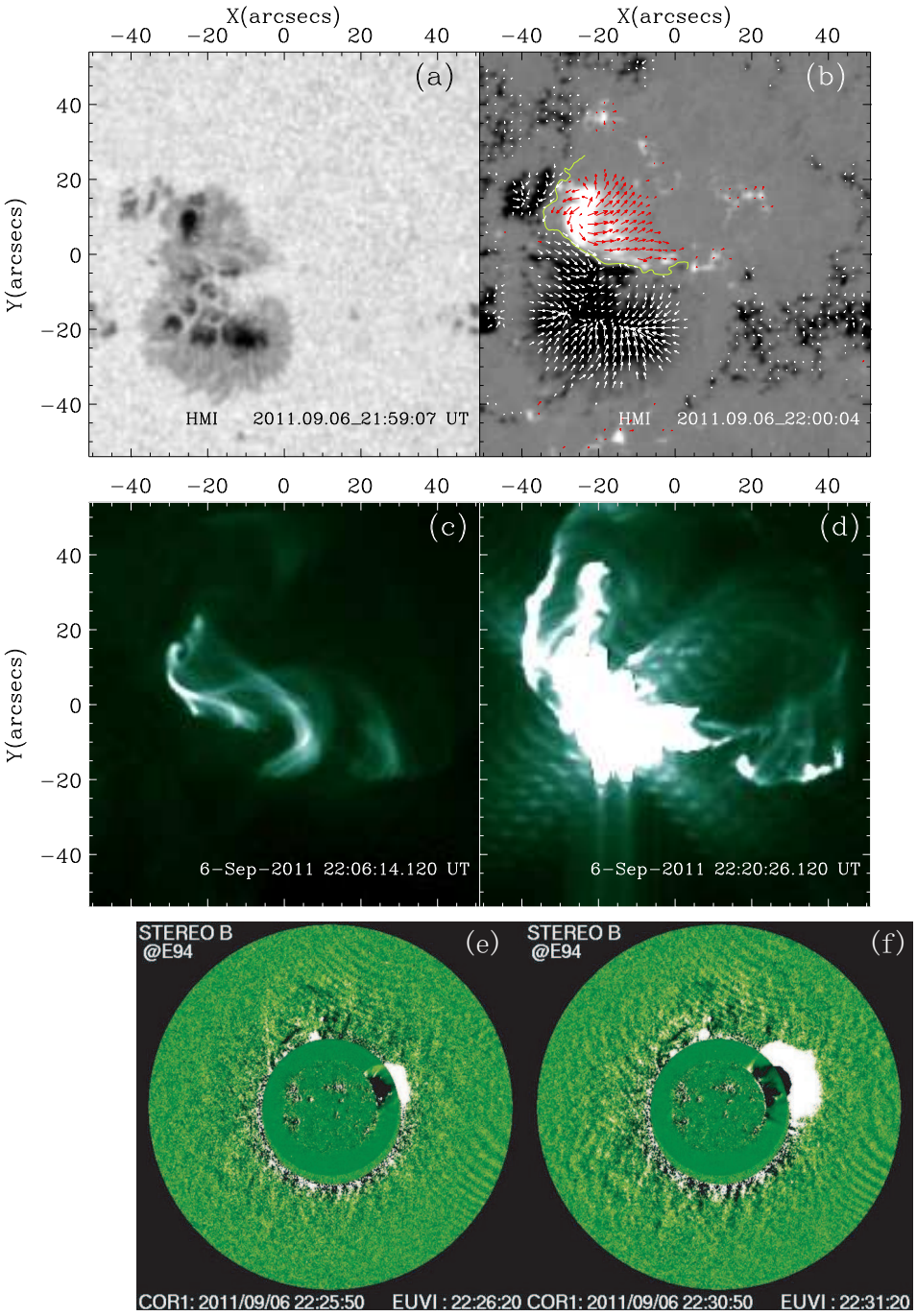

Figure 7.1 (a, b): The HMI continuum intensity image and vector magnetogram for the NOAA AR 11283 (N14W18) observed at $\sim 22:00$ UT on September 6, 2011. B_z is shown in white (black) for positive (negative) polarity, B_h is represented with arrows that are color-coded according to the corresponding B_z polarities. The yellow line represents the PIL. (c, d): The AIA 94 Å images at 22:06 UT and 22:20 UT in the same FOV as panel a. (e, f): The CME images observed by STEREO-B.

In Figure 7.1, we present the intensity map (panel a) and HMI vector magnetogram (panel b) at ∼22:00 UT on September 6, just before the X2.1 flare. We show the local vertical (i.e., radial) magnetic field component (B_z) in white and black for positive and negative polarities. The color-coded arrows in panel (b) represent the horizontal magnetic field B_h, which is the component parallel to the solar surface (i.e., $B_h = \sqrt{(B_x^2 + B_y^2)}$, where x and y represent two orthogonal directions in the plane of the solar surface). The yellow curve represents the magnetic PIL. From the temporal evolution of the HMI vector magnetic field, this AR is characterized by an emerging positive polarity sunspot. The emergence started from the heliographic location N13E28 near the end of September 3 and was the dominant process in the first two days. After that, the AR developed into a $\beta\gamma\delta$ magnetic complexity. Since early September 6, the emerged sunspot exhibited an apparent clockwise rotation, as well as a slow westward shearing motion along the PIL. The rotation direction is consistent with the right-handed twist of the horizontal field as can be seen in panel b. Near the PIL, this field component is almost parallel to the PIL indicating the presence of strong magnetic shear.

Many flares have been produced by this AR from September 3 to 7. Among them, three big flares were observed on September 6 and 7 with GOES SXR flare classes being M5.3, X2.1, and X1.8. Their peaking times were 1:50 UT and 22:20 UT on September 6, and 22:38 UT on September 7, respectively. The sunspot rotation can be discerned a few hours before and after the M5.3 flare. It then became harder to trace until at ∼16:00 UT, 6 hours before the X2.1 flare, when two magnetic tongues formed, providing excellent tracer to the rotation. We focus our analysis in this 6-hour period to examine the role of sunspot rotation in the onset of the eruption associated with the X2.1 flare.

It is important to understand the topology of the coronal magnetic structure and how important the rotation in the coronal energy accumulation process. To achieve

this, we reconstructed the three-dimensional (3D) coronal magnetic field using the nonlinear force-free field (NLFFF) extrapolation method developed by Wiegelmann (2004); Wiegelmann et al. (2006) on the basis of HMI data. Details of the method are presented in the Appendix.

7.3 Results and Interpretation

The X2.1 flare started at 22:12 UT, peaked at 22:20 UT, and ended at 22:50 UT according to the GOES x-ray (1-8 Å) light curve shown in Figure 7.2. The pre-flare (22:06 UT) and flare-peaking (22:20 UT) images observed in the 94 Å bandpass have been shown in panels c and d of Figure 7.1 and the accompanying animation. The pre-flare hot structures exhibited an arcade connecting the northern and southern ends of the eruptive structure, two sets of arcade loops of different size, and highly twisted structures at the north-west part of the image. The large bright area in the post-flare 94 Å image indicates a strong heating there.

The flare was accompanied by a halo CME travelling at a linear speed of 575 km s^{-1} according to the CDAW (Coordinated Data Analysis Workshops) catalog of the LASCO data (Brueckner et al. 1995). The eruption was also observed with the STEREO spacecraft (Howard et al. 2008) as a limb event. Panels e and f of Figure 7.1 present two subsequent images at ∼22:26 UT and 22:31 UT observed by COR1 and EUVI aboard STEREO-B. We see that the CME front moved ∼0.5 R$\odot$ within 5 minutes yielding a speed of ∼1200 km s^{-1}, much faster than that measured with LASCO. This is mainly due to the projection effect and the CME deceleration during its propagation to the outer corona.

Figure 7.3 presents sequences of the sunspot (a-c) and the filament (d-f) morphological evolutions. The contours in panels b and e represent the ±350 G level of B_z at ∼19:00 UT. We can see from this figure that the dominant motion in this period was the sunspot rotation. The sunspot developed co-rotating magnetic

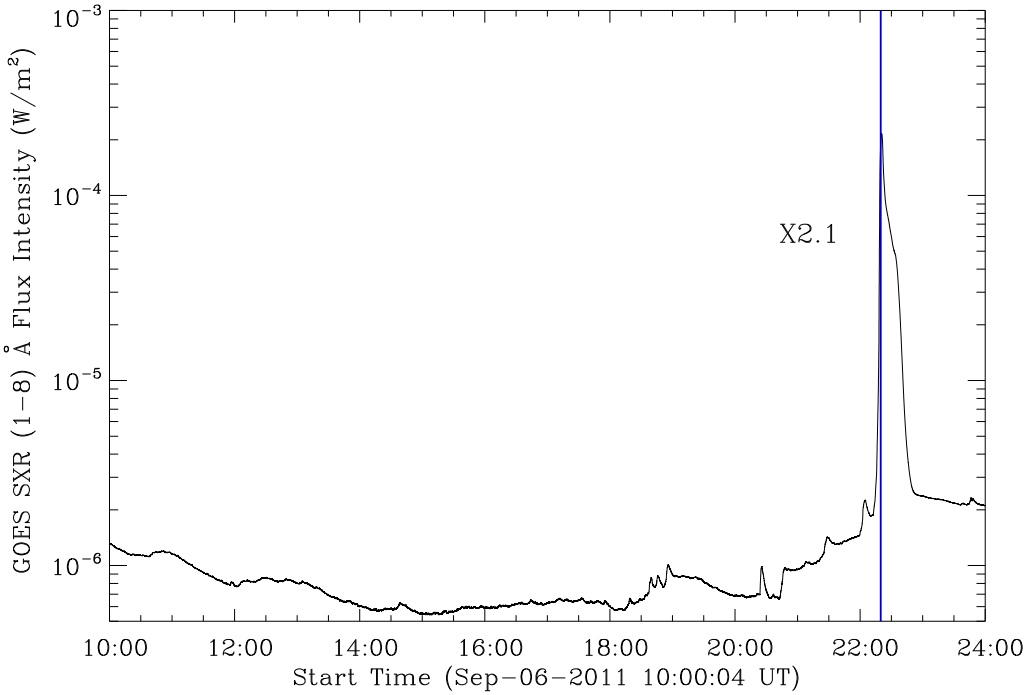

Figure 7.2 The 1-8 Å GOES SXR flux intensity profiles. The blue vertical line represents the flare peaking time (22:20 UT).

tongues at ∼16:00 UT on September 6. This allows a quantitative determination of the rotation rate. To do this, we present in Figure 7.3 (g) the $r - \theta$ time-slice plot of the sunspot for the time range of 10:00 UT to 24:00 UT. The $r - \theta$ plot was produced by retrieving images along two semi-circular slices with a radius of $\sim 3.5'' $ and $3''$ around the sunspot center (which is in motion), and stack them over time. The $\theta = 0^\circ$ is along the northward (upward) direction. The angle increases in the clockwise direction. We use two slices so that we can examine both tongues simultaneously.

The $r - \theta$ plot reveals features consistent with the above description of the sunspot rotation. We can see that the sunspot rotated by $\sim 60^\circ$ in the 6 hours prior to the flare, with an average rotation rate $\sim 10^\circ$ per hour. After the flare (peaking time shown by the blue vertical line), the sunspot experienced a sudden morphological change and the rotation became hard to track. In comparison with events reported earlier (e.g., Zhang et al. 2007; Yan et al. 2012), our event can be regarded as a fast rotation one. Along with the rotation, the sunspot center moved westward by $\sim 2'' $ in the 6 hours. Comparing to the fast rotation, the shearing motion seems to be insignificant, which is therefore presumed to play a less important role in the onset of the eruption.

From panels d-f of Figure 7.3, the entire filament structure exhibited a highly curved pattern with two segments. The southern and the northern segments were disconnected from each other at both ends. The southern filament erupted first which was followed by the eruption of the northern filament. In this study, we focus only on the southern filament. It presented a highly-curved sigmoidal morphology. Since its northern end was mostly rooted in the sunspot penumbra region, we suggest that the sunspot rotation was directly related to the dynamics of this filament.

There were clear filament morphological changes during the 6-hour period. According to Figure 7.3, the filament exhibited separated filamentary structures which

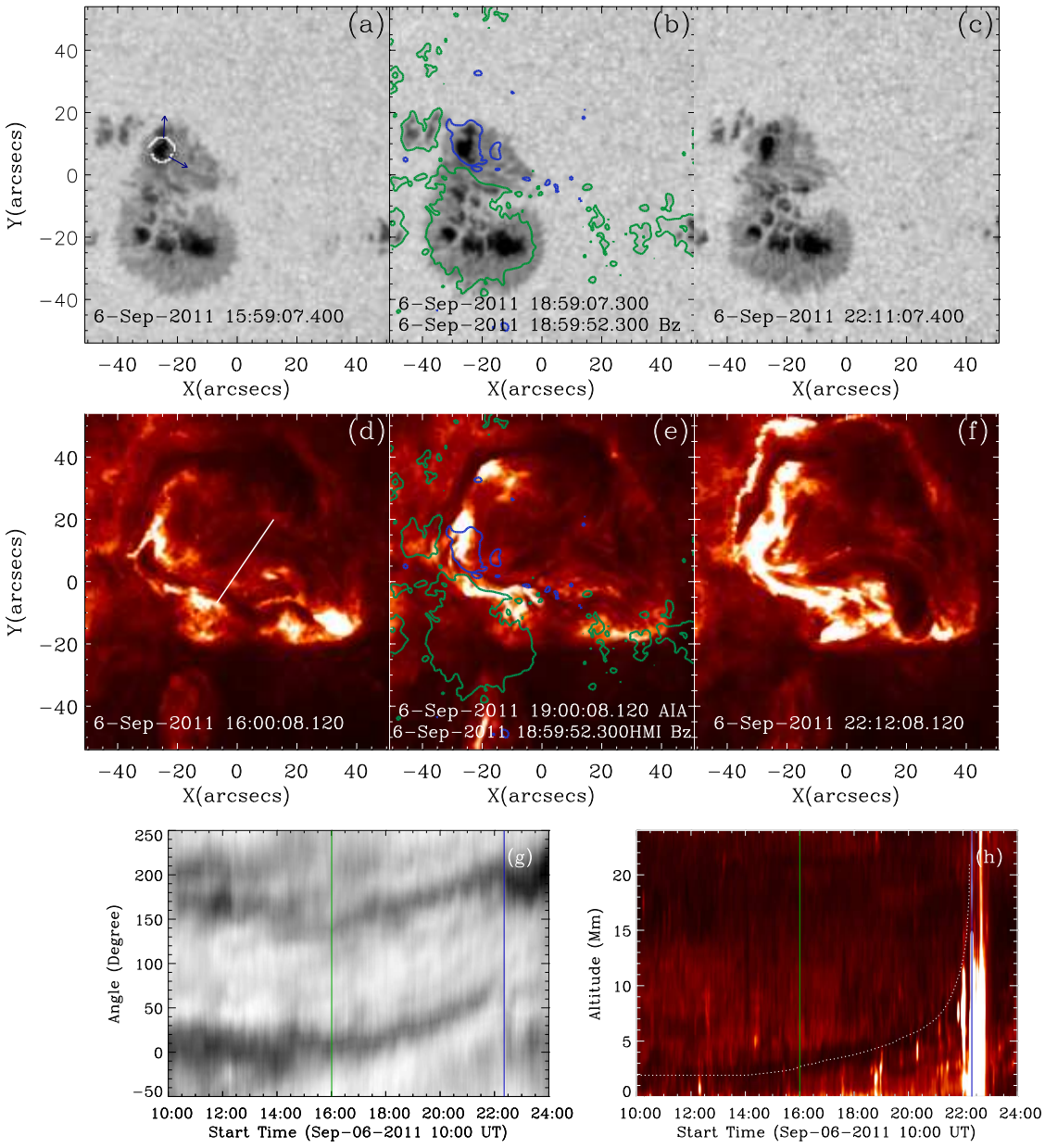

Figure 7.3 (a-h): Sequences of sunspot (a-c) and filament (d-f) morphological evolutions in the same FOV as that of Figure 7.1 (a). The blue and green contours in panels b and e represent the ±350 G level of B_z at ∼19:00 UT. The two arrows in panel a point alongside the two magnetic tongues. (g): The $r-\theta$ plot of the rotating sunspot. (h): The height-time plot for the filament along the white line shown in panel d. The green and blue vertical lines in panels g and h represent the start time of apparent sunspot rotation (16:00 UT) and the flare peaking time (22:20 UT).

seem to be twisted around each other. The filament became more bulging after 20:00 UT. At ∼22:00 UT, the filament already started to rise rapidly before the start of the flare (22:12 UT). The filament motion can be viewed from the time-slice plot shown in panel h. The slice is drawn in panel d as a white line. The white-dotted line in panel h is drawn to indicate the moving filament. As can be seen, the motion of the filament along the slice was hardly measurable before 16:00 UT, and was clear from 16:00 UT to 21:00 UT, during which it moved a distance of ∼5 Mm (∼7′ ′).

It has to be noted that the above measured moving distance consists of contributions from both the radial (or vertical) and horizontal motions of the filament, and it is generally difficult to disentangle them due to the projection effect. Nevertheless, we can estimate the maximum rising distance of the filament by assuming a pure radial motion. With this assumption, the deprojected motion ($\triangle R$) of the filament can be given by $\triangle R = \triangle r \frac{R_\odot}{r}$, where $\triangle r$ and r are the filament moving distance and the distance from the filament center to the solar center as measured in the projection plane. The real distance from the filament to the solar center is approximated by the solar radius assuming that the initial filament height is negligible comparing to the solar radius. A schematic showing the relationship between these parameters is shown in Figure 7.4. According to the AIA data, we have $r \sim 0.34 R_\odot$ at 16:00 UT and $\triangle r \sim 7''$. This leads to a maximum rising height of $\triangle R \sim 20''$.

In the pre-event process, several temporary and persistent brightening structures were observed in the 94 Å bandpass (see the animation accompanying Figure 7.1), indicating the existence of reconnections. These reconnections can release part of the accumulated energy and affect the dynamics and morphology of the filament.

To further explore the details of magnetic field evolution, we display the distributions of B_h at 22:00 UT (panel a) and 22:36 UT (panel b) in Figure 7.5. It can be seen that B_h increased rapidly after the flare, in agreement with previous studies

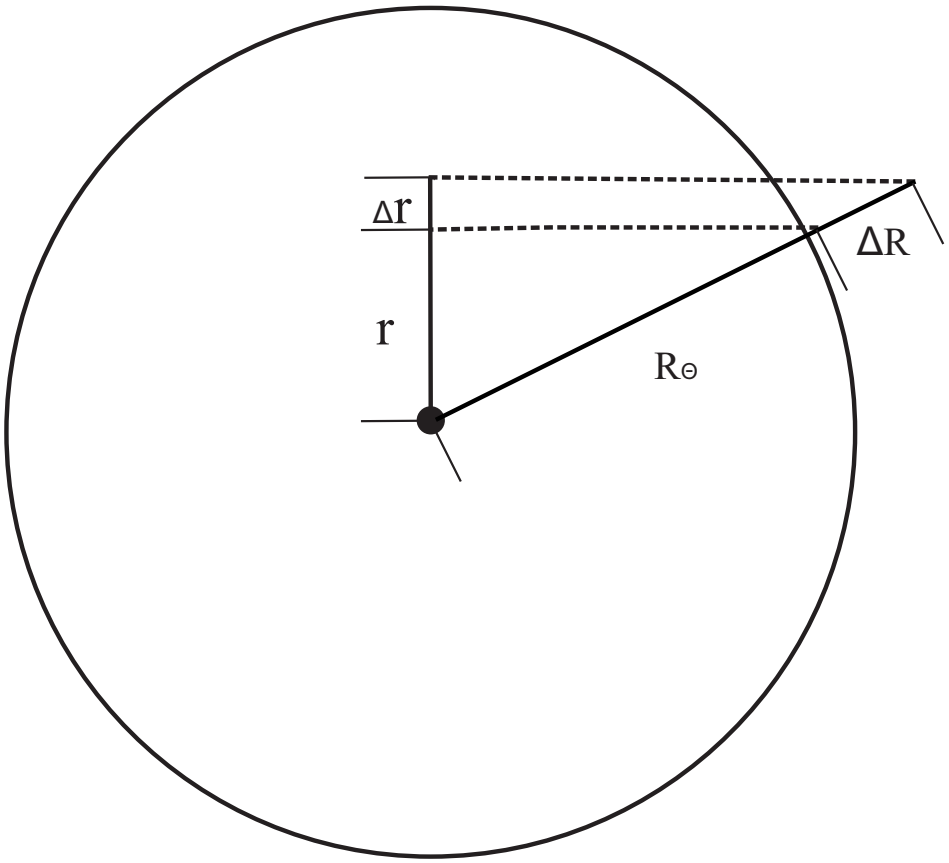

Figure 7.4 Schematic showing the relationship between the projected and deprojected (i.e., real) filament heights (r and R) and rising distances ($\triangle\ r$ and $\triangle\ R$). See text for more details.

(e.g., Wang et al. 1994; Wang & Liu 2010; Liu et al. 2012; Wang et al. 2012b; Sun et al. 2012). The post-flare B_h contour observed at 22:36 UT at a level of 1250 G is plotted in both panels, outlining the major region of the flare-induced B_h enhancement, which is referred to as region R hereafter. It can be seen that region R is underneath the filament and across the PIL. In this study, we focus on the variation of the pre-flare photospheric field in the above region defined by the post-flare B_h enhancement. Note that magnetic field measurement during flare time (within $\sim$30 minutes in general) is less accurate than before and after the flare (e.g., Qiu & Gary 2003).

The temporal evolutions of the average B_h and the positive and negative B_z in R are plotted in Figure 7.6, as the black-solid, blue-dotted, and dashed lines, respectively. The error bars of the B_h and B_z data shown in this figure are given by 3σ where σ is the standard deviation of the HMI data obtained from a nearby quiet-sun region. Also plotted are the inclination angle of the vector photospheric magnetic field (θ_B) (i.e., the angle between the local vertical direction and the vector magnetic field) in green and the total flux in red-dotted.

It can be seen that before the sudden changes of B_h and θ_B, there were gradual but steady decreases of both quantities. This trend was especially clear during the 6-hour period between 16:00 UT and 22:00 UT. Indeed, the average B_h decreased consistently by 15% from about 1185 G at 16:00 UT to 1009 G at 22:12 UT. In comparison, both the absolute value and variation of B_z were much smaller than that of B_h during the 6 hours before the flare. The positive B_z increased from 350 G to 410 G, while the negative one changed from -160 G to -153 G during the same period. The total flux (the red dotted line) presented a slow yet steady increase with no apparent change of increasing rate during the period of sunspot rotation (i.e., after 16:00 UT). On the other hand, the average θ_B changed persistently from $\sim 70^\circ$ to $\sim 63^\circ$ during the 6 hours of sunspot rotation. This suggests that the relevant magnetic structures became more vertical. The total magnetic field strength (not

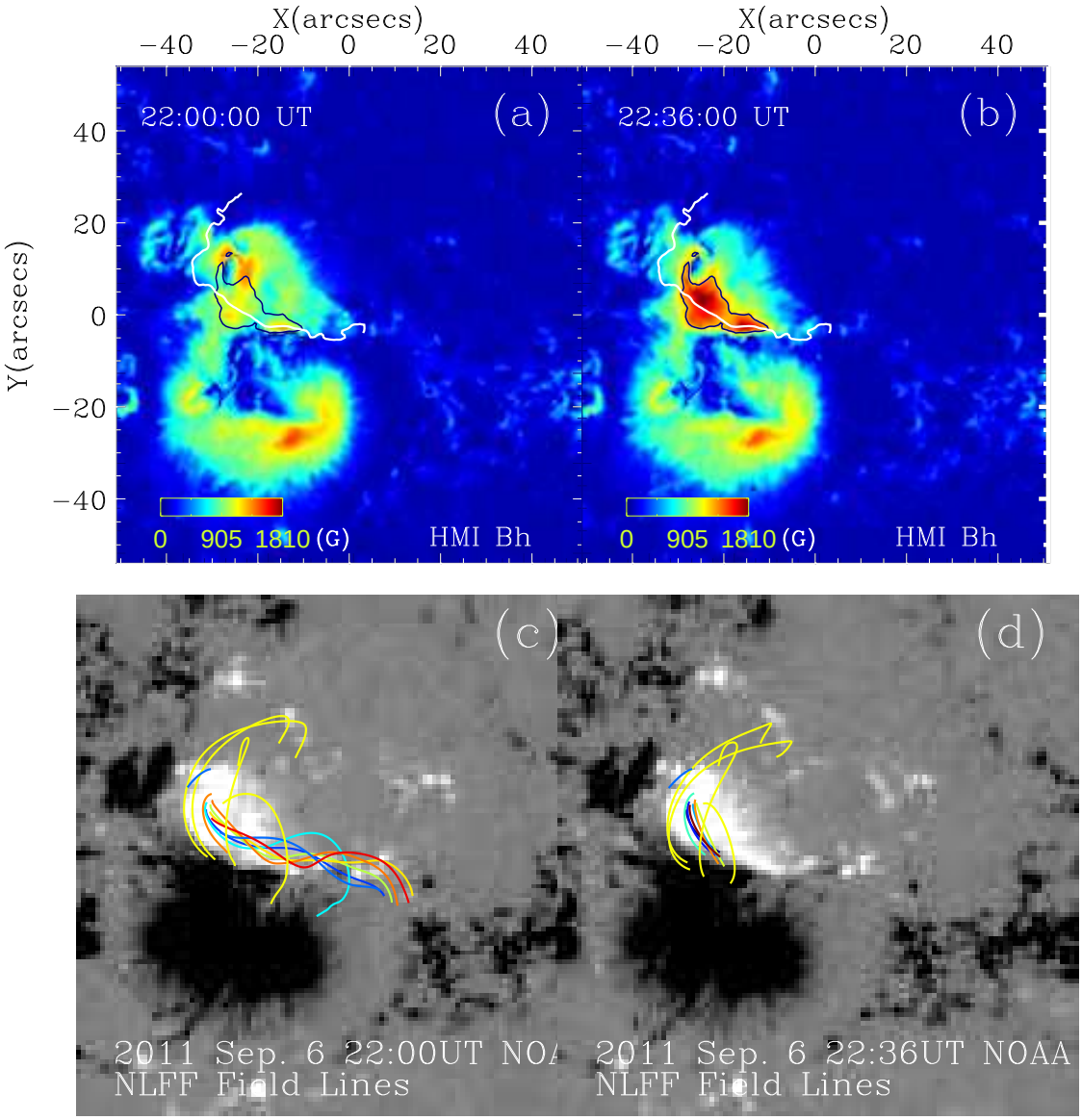

Figure 7.5 (a, b): The B_h distribution at 22:00 UT and 22:36 UT. (c, d): Selected coronal field lines given by the NLFFF reconstruction method.

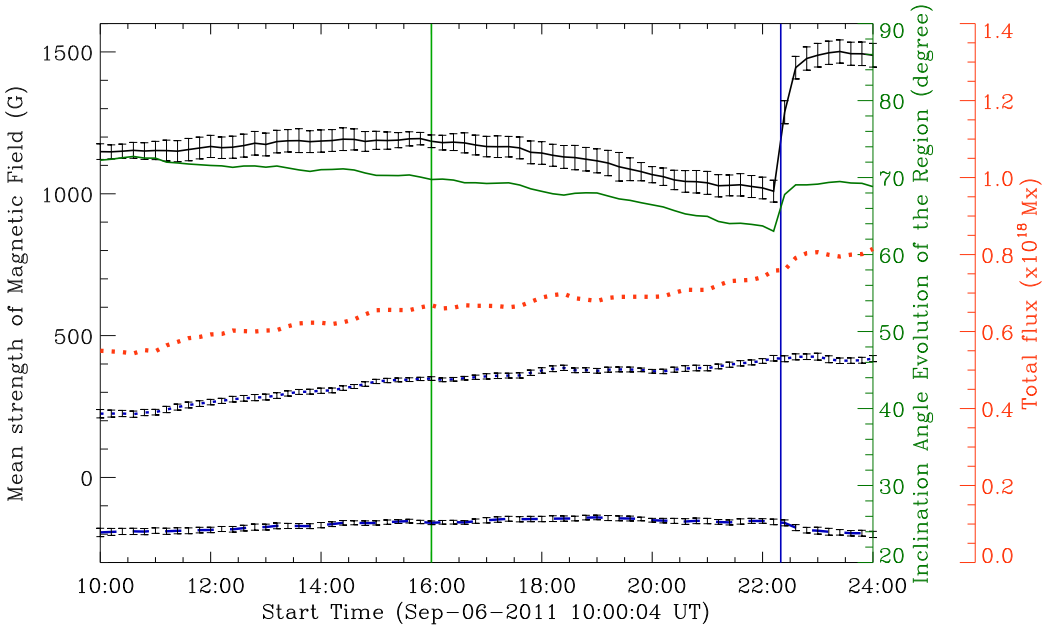

Figure 7.6 The temporal profiles of the average B_h (black solid), the average of the positive (blue dotted) and negative (blue dashed) B_z components, the total flux (red dotted) and inclination angle θ_B (green solid) in the area defined by the black contour of Figure 7.5 (b). The green and blue vertical lines represent the start time of apparent sunspot rotation (16:00 UT) and the flare peaking time (22:20 UT).

shown here) decreases gradually in a manner similar to that of B_h since B_h is much stronger than B_z. It is expected that when a magnetic structure rises into the corona it will expand into a larger volume. This will result in a decrease of both the total and the horizontal magnetic field strength, consistent with our observation.

Selected field lines of NLFFF reconstructions are shown in Figure 7.5(c & d). The location of the low-lying twisted magnetic structure, i.e., a flux rope structure, co-aligned with the southern filament. Note that the magnetic topology of this event was also reconstructed and studied by Jiang & Feng (2013); Jiang et al. (2013, 2014); Feng et al. (2013). They have presented similar reconstruction results as shown here. We can see that these field lines and some overlying magnetic arcades were rooted in the rotating sunspot, agreeing with the observation shown in Figure 7.3. Thus, the sunspot rotation may affect both the twisted filament-flux rope structure and the overlying arcade. After the flare, the field lines in the filament location became shorter and less twisted indicating a relaxed energy state.

We plot in Figure 7.7(a) the temporal profile of the total energy of the reconstructed magnetic field in a sub-volume with a bottom shown as the blue square in Figure 7.7 (b) and the same height as that used for the NLFFF reconstruction. The sub-domain is selected to focus on the smaller region of eruption. An estimate of the total magnetic energy in the whole reconstruction domain yields a very similar profile. We see that the total magnetic energy in this sub-domain shows a rapid increase after 16:00 UT, which is the starting time of the apparent sunspot rotation, and an abrupt decline during the flare. The energy increase from 16:00 UT to ∼22:00 UT is about 3×10^{31} erg, which is capable of energizing a major solar event (e.g., Vourlidas et al. 2002) and therefore probably important to the onset of the following eruption. This indicates that the sunspot rotation, which is a major dynamical feature of the active region, is important to the pre-eruption energy storage in the corona. A detailed study on the energetics of this event, including the estimates of the free magnetic

energy before and after the eruption, the thermal and nonthermal energies for the flare, the CME kinetic and potential energies, as well as the partition of the released magnetic energy between the CME and the flare, has been presented by Feng et al. (2013). They show that the flare and the CME may have consumed a similar amount of magnetic free energy within the estimate uncertainty.

One likely driving mechanism of the eruption in our event is illustrated in the schematics shown in Figure 7.8. The white structure with two extending tongues indicates the rotating sunspot with the rotating direction denoted by the arrows. The long twisted field lines along the PIL represent the magnetic structure associated with the filament, representing the filament-carrying flux rope structure whose chirality is consistent with the direction of sunspot rotation. The flux rope and a part of the overlying arcades are rooted in the rotating sunspot. Thus, the sunspot rotation can directly transport energy and helicity into the coronal flux rope system. Török et al. (2013) proposed a novel mechanism for CME eruption induced by the expansion of the overlying arcades that are rooted in a rotating sunspot. Our study provides observational evidences supporting their scenario. Note that our observations show that both the flux rope-filament structure and the overlying arcades were twisted by the rotation of the sunspot. Both twistings may play a role in driving the eruption in our event, and it is not possible to disentangle them. From Figure 7.8 (a) to 6.8c, the sunspot rotates about $\sim 60^{\circ}$, as indicated by the locations of the two tongues. Correspondingly, the central part of the twisted field lines expands and moves higher and the overlying arcades become more vertical. These features agree with the observations of the filament rising and the gradual decreases of both the horizontal component and the inclination angle of the photospheric magnetic field. In short, the observational features in our event can be understood with a flux rope CME driven by a persistent sunspot rotation, as schematically illustrated here.

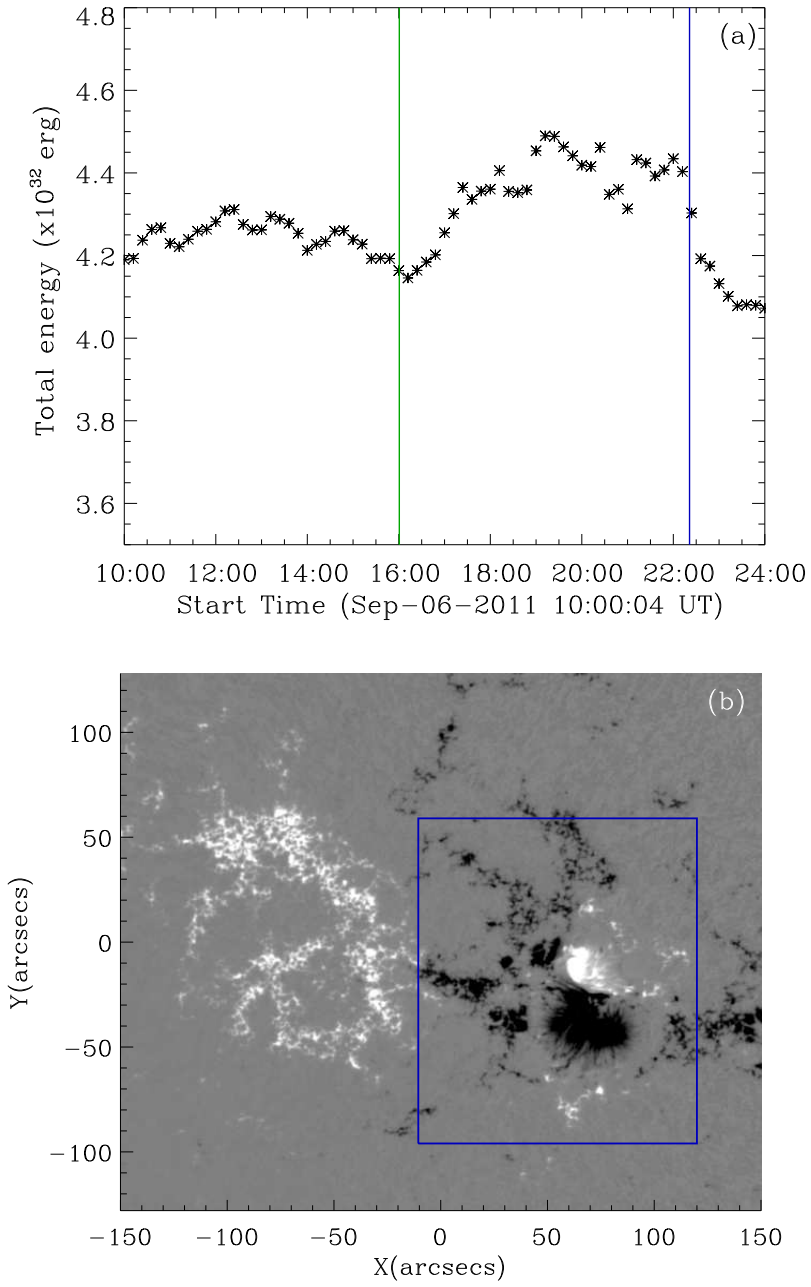

Figure 7.7 The temporal profile (panel a) of the total energy of the reconstructed magnetic field in a sub-volume with a bottom shown as the blue square in panel (b) and the same height as that used for the NLFFF reconstruction. The green and blue vertical lines represent the start time of apparent sunspot rotation (16:00 UT) and the flare peaking time (22:20 UT).

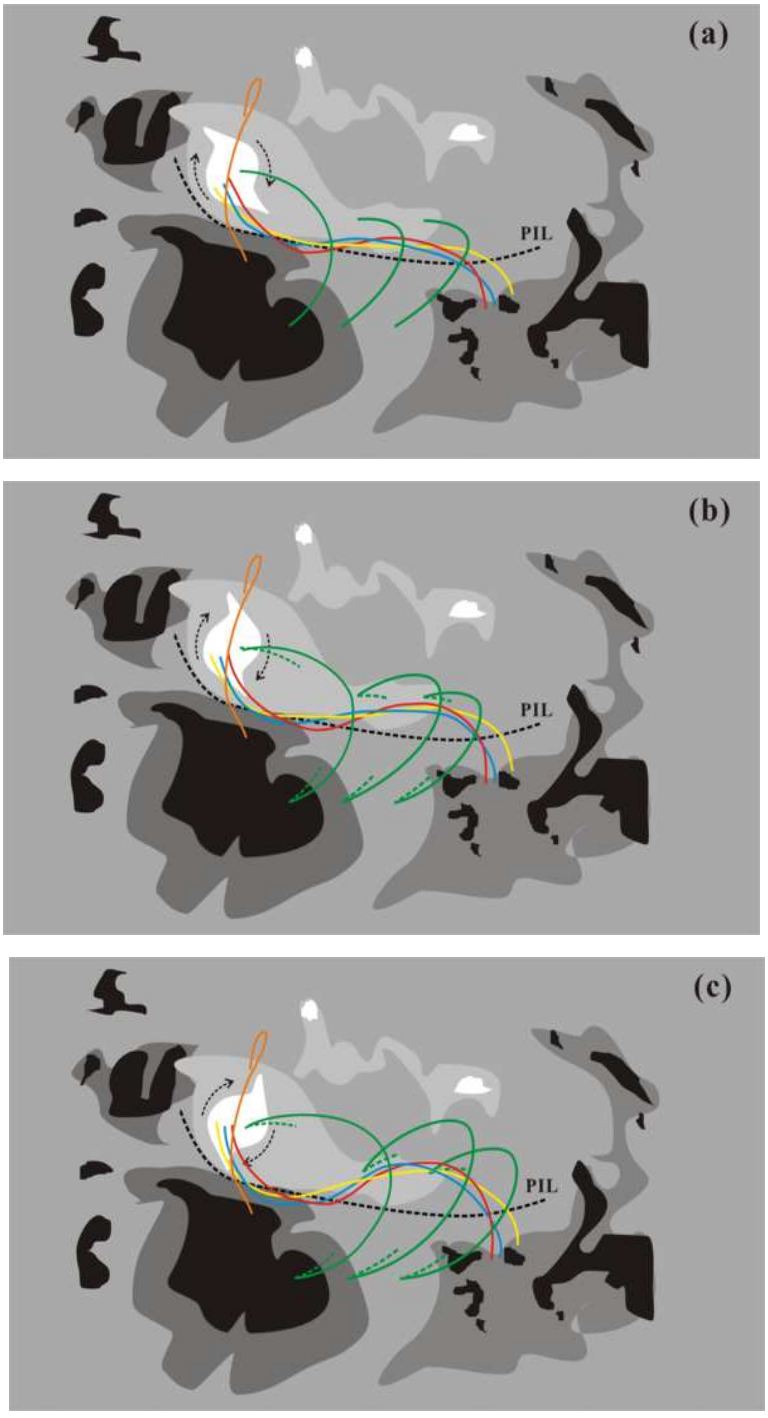

Figure 7.8 Schematics of a flux rope CME driven by persistent sunspot rotation. The rotating sunspot is indicated by the white structure with two extending tongue structures. The rotating direction is denoted by two curved arrows. The short green dashed lines indicate the field line location at the preceding moment. See text for more details.

7.4 Summary

We present observations of a sunspot rotation before a major solar event consisting of a fast CME, an X2.1 flare, and a filament eruption. We suggest that this pre-eruption rotation is not only transporting energy to the corona, but also playing a dynamic and critical role in leading to the eruption. Our suggestion is based on the data analysis results, which are summarized below. Firstly, the sunspot rotation was the dominant motion in the 6 hours before the flare. The rotation rate was $\sim 10^{\circ}$ per hour, considerably faster than some previous observations (e.g., Zhang et al. 2008). Secondly, the filament and part of the overlying arcades were rooted in the rotating sunspot, and the filament exhibited an apparent gradual rising motion along with the sunspot rotation. This provides a possible dynamical link between the sunspot rotation and the filament dynamics as well as the resultant eruption. Thirdly, the evolutions of both the photospheric horizontal field and the magnetic field inclination angle agree with the gradual rising of the magnetic structure that supports the filament. Last, using the NLFFF method of coronal magnetic field reconstructions, we find the presence of a well-developed twisted flux rope structure associated with the filament and a considerable amount of magnetic energy increase during the sunspot rotation period. These results highlight the importance of sunspot rotation to the energy storage and the onset of the eruption.

The evolution of photospheric magnetic field is essential to both the energy build-up and the triggering of a solar eruption. Many studies have focused on rapid changes of B_h induced by the flare (e.g., Wang et al. 1994; Wang & Liu 2010; Liu et al. 2012; Wang et al. 2012b). However, the detailed pre-flare evolution of this field component has not received sufficient attention. Such evolution would carry important information of the energy storage and eruption onset process. In our study, we found that B_h in the area underneath the filament decreased gradually in hours before the flare. This is related to the gradual ascending of the filament-

flux rope structure. Our analysis indicates that this is associated with the rapid sunspot rotation. On the contrary, studies of another active region (NOAA AR 11158) revealed that B_h there increased gradually in a similar time period prior to the flare (Liu et al. 2012; Wang et al. 2012b). Those studies deduced that the corresponding eruptions were driven by tether-cutting reconnection (Moore et al. 2001) of two approaching magnetic loops. The pre-flare footpoint separation of these loops can explain the gradual increase of B_h. By comparing the different behavior of B_h and corresponding understanding of the eruption mechanism, we suggest that the pre-flare variation of B_h can be taken as a clue to discern the eruption mechanism: A gradual decrease of B_h may be a precursor for an eruption in terms of the flux rope instability, while an increase of B_h may be the precursor for tether-cutting reconnection. This needs further clarifications in future studies.

CHAPTER 8

SUMMARY OF THE DISSERTATION

The work presented in this dissertation focuses on the relationship between solar activities and certain physical parameters in the photosphere including vector magnetic field and flow field. Solar flares and CMEs are generally believed to be manifestations of a sudden and rapid release of the accumulated magnetic energy in the corona. The transients created in the tenuous low-beta corona are generally thought unlikely to alter the photospheric magnetic fields, which are line-tied to the dense high-beta photosphere. However, rapid and permanent photospheric magnetic field changes associated with flares were discovered twenty years ago (Wang 1992; Wang et al. 1994). Since then, Space Weather Research Lab at NJIT continued on this topic and found many consistent results and interesting phenomena which are all pointed to a photospheric response to solar flares. A trend indicating a more horizontal orientation of the photospheric magnetic field around the flaring PILs after flares and CMEs has continued to be observed (Wang et al. 2002, 2004b, 2005; Liu et al. 2005; Wang et al. 2007; Jing et al. 2008; Li et al. 2009; Liu et al. 2011) and shows some agreement with recent model predictions (Li et al. 2011). Sudden penumbral decay and umbral darkening due to the photospheric magnetic field change associated with flares are also reported (Liu et al. 2005; Deng et al. 2005; Wang et al. 2005; Jing et al. 2008). In particular, the feature of unbalanced flux evolution of opposite polarities provides an indirect evidence for the more horizontal orientation of photospheric magnetic fields around flaring PILs after flares/CMEs (Wang & Liu 2010).

Only recently, a rapid back reaction on the photosphere due to the coronal magnetic field reconfiguration has been seriously considered from the theoretical point of view (e.g., Hudson et al. 2008; Fisher et al. 2012), with a prediction that the

photospheric magnetic field would be oriented more horizontally resulting in a Lorentz force acting downwardly on the solar surface and interior. Such magnetic impulse is speculated to cause sudden perturbation of sunspots and excitation of seismic waves. Meanwhile, the equal-magnitude, upward Lorentz-force change may drive the eruption of CMEs. Therefore, the changes in the photospheric field and dynamics associated with flares/CMEs could serve as a direct observational probe of the energy transformations and momentum balance in the flare/CME process. This dissertation made substantial progress on this topic. Its main results are summarized in the following.

- The first solid evidence of a rapid and irreversible enhancement in the photospheric horizontal magnetic field at the flaring magnetic PIL is obtained. Furthermore, a statistical study of magnitude of change in the horizontal magnetic field during flares is carried out, and the relationship between GOES X-ray flare class and several physical paramters characterizing photospheric horizontal magnetic field enhancement is provided. For the first time, such magnetic field changes have been observed even for C-class flares.

- The rapid formation of sunspot penumbra at the PIL associated with a C-class flare is reported. It is accompanied with an enhancement in the photospheric horizontal magnetic field. Together with related papers (Liu et al. 2005; Deng et al. 2005; Wang et al. 2005; Jing et al. 2008), a clear profile of photospheric intensity change associated with flares is provided: significant magnetic field enhancement associated flare can cause decrease of intensity, and penubral formation / umbral formation / umbral darkening are possible. On the contrary, the region with decreased photospheric horizontal magnetic field may be brighter than before in white light, and a penumral decay could be observed. These intensity changes not only corroborate the photospheric magnetic field change, but also are capable of providing temporal information of the field change.

- The relationship between the vertical component of Lorentz-force change and CMEs is studied. A new practical way of estimating the CME mass is demonstrated based on the conservation of momentum.
- Sudden rotation of sunspots associated with flares is found through studies of flow field and vorticity. The corresponding change of the horizontal component of Lorentz force and its induced torque applied on spots are studied as well. The Lorentz-force change is proposed to be a possible driving force of sudden sunspot rotations. In the region with a photospheric horizontal magnetic field enhancement, a sudden change of the behavior of shear flows and the corresponding change of the horizontal comonent of Lorentz force are found.
- Magnetic field evolution before solar eruptive events is studied in chapter 7 to further understand the triggering mechanism. In this case study, a fast rotating sunspot may inject helicity and energy into the coronal flux rope system. The gradual decrease of photospheric horizontal magnetic field accompanied with the gradual rising filament rooted in the rotating sunspot before the flare provide a dynamic link to the eruption. This case study shows another side of the interaction between photospheric flows and solar eruptive events.
- Free magnetic energy (FME) was compared with ARs flare index (FI) in a statistical study of 6261 vector magnetograms in 61 ARs. There is a weak correlation ($< 60\%$) between FME and FI. FME shows slightly improved flare predictability relative to the total unsigned magnetic flux of ARs in the following two aspects: (1) the flare productivity predicted by FME is higher than that predicted by magnetic flux and (2) the correlation between FI and FME is higher than that between FI and magnetic flux.

As massive solar observational data are accumulating, physical variables related to space weather prediction may be under investigation for both statistical relationships and unusual cases. With tools such as automated feature detection,

anomaly detection, support vector machine, online machine learning algorithm, and artificial neural networks, we expect better understanding of the physical mechanisms of flare and CME. This can then be used to refine the numerical modeling and simulation, and finally improve our space weather forecasting results. Several prospective topics related to this dissertation for future research are outlined below.

- Circular flares are a rare type of flare (Wang & Liu 2012; Deng et al. 2013; Liu et al. 2013b). This type of flare requires fan-spine magnetic topology and only occur at the null point which is at higher altitude than most flares with sigmoid configuration. We expect that the impact of this kind of flare to the photosphere should be significantly less than common cases if there is any. The photospheric magnetic field evolution associated with circular flares may worth a careful examination; in particular, the result should be compared with that of the well-studied sigmoid eruption.
- The 1.6 m NST at Big Bear Solar Observatory provides solar observational data with highest spatial resolution so far. Another major observational facility is the 1.5 m GREGOR solar telescope at the Teide Observatory. The 4 m Daniel K. Inouye Solar Telescope (DKIST) is under construction by the National Solar Observatory. These new telescopes are expected to provide unprecedented high-spatial resolution data. Features with small scales can be detected and tracked with these data. The flow tracking of solar eruption events with NST data may provide us more details of known phenomenon such as sudden rotation discussed in chapter 4 and new discoveries.
- Numerical simulations of theoretic models make it possible to scrutinize the proposed models and predict phenomena that have not been discovered yet possibly due to noise or limits of current observing instruments. Recently, data-driven magnetohydrodynamics (MHD) models successfully reproduced many solar activities (Jiang & Feng 2013; Jiang et al. 2013, 2014; Inoue et al.

2014). Jiang et al. (2013) studied the formation and eruption of AR 11283 with a sigmoidal configuration by implementing their numerical model with a time series of observational data as constraint. Their simulation produced some interesting results such as the implosion effect, which is consistent with our observational results described in Chapter 2. Furthermore, Inoue et al. (2014) performed an MHD simulation for AR 11158. Their results match the tether-cutting reconnection model and are consistent with the observational results in Chapter 2 as well. Collaborations with numerical simulation teams by making comparisons between observations and theoretic modeling (especially the data driven modeling) has promise to provide further insights into mechanisms of solar eruptions.

APPENDIX

NLFFF EXTRAPOLATION METHOD OF THE CORONAL MAGNETIC FIELD

The coronal magnetic field was reconstructed using the extrapolation method developed by Wiegelmann (2004). The code of the method was provided by Thomas Wiegelmann. The HMI magnetograms were preprocessed to remove most of the net Lorentz force and torque from the data so as to be more consistent with the force-free assumption (Wiegelmann et al. 2006). The extrapolation was performed using 2×2 rebinned magnetograms within a box of 217×185×145 Mm^3 at the 12 minute cadence. The corresponding grid number is taken to be 300×256×200 with a uniform spacing of $1.0''$.

The method employs a weighted optimization approach which minimizes a joint measure for the Lorentz force density and the divergence of the field throughout the computational domain (Wheatland et al. 2000), which is represented by the optimization integral L. The performance of the method is further evaluated by calculating the average dimensionless field divergence f and the current-weighted average of $\sin\theta$ (CWsin) where θ is the angle between the vector magnetic field $\boldsymbol{B}$ and the current density $\boldsymbol{J}$ ($0^\circ \leq \theta \leq 180^\circ$) (c.f., Schrijver et al. 2006, 2008; Metcalf et al. 2008; DeRosa et al. 2009). The optimization measure L is defined as

$$L = < \omega_f(\boldsymbol{r}) B^{-2} |(\nabla \times \boldsymbol{B}) \times \boldsymbol{B}|^2 > + < \omega_d(\boldsymbol{r}) |\nabla \cdot \boldsymbol{B}|^2 > \qquad (A1)$$

where the angle bracket denotes the mean value within the domain, the first and second parts of L represent a measure of the mean Lorentz force density (L_f) and the mean field divergence (L_d), respectively. Both ω_f and ω_d are position dependent to reduce the effect of boundary conditions. They are fixed to be 1.0 in the center of the computational domain and drop to 0 monotonically with a cosine profile in a buffer

boundary region that consists of 32 grid points toward the side and top boundaries. It is found that the optimization measure L decreases from an initial value of 109.6 to a final value of 11.5, while the field divergence measure L_d decreases from ∼47.4 to 4.0, and the Lorentz force measure L_f decreases from ∼62.2 to 7.5, in units of G^2 $arcsec^{-2}$. These values of the optimization measure are comparable to previously reported values for other events (e.g., Schrijver et al., 2008; Sun et al., 2012).

The code checks whether $L(t+dt) < L(t)$ after each time step. If the condition is not fulfilled, the time step dt is reduced by a factor of 2 and the iteration step is repeated. After each successful iteration step, dt is increased by a factor of 1.01. This allows dt to become as large as possible while satisfying the stability condition. The iteration stops if the condition $|\frac{\triangle L_w}{\triangle t}|/L_w < 10^{-4}$ is satisfied for 100 consecutive iteration steps.

The current weighted average of $\sin\theta$ is defined as

$$\texttt{CWsin} = \frac{\sum_i |J_i|\sigma_i}{\sum_i |J_i|}, \sigma_i = \frac{|J_i \times B_i|}{|J_i||B_i|} = |sin\theta_i|, \quad (A2)$$

and the pointwise average of the divergence f is defined by

$$f =< |f_i| >=< \frac{|(\nabla \cdot \mathbf{B})_i|}{(6|\mathbf{B}|_i/\triangle x)} >, \quad (A3)$$

where i represents the grid point and Δx is the grid spacing (c.f., Schrijver et al. 2006, 2008; Metcalf et al. 2008; DeRosa et al. 2009). For the final reconstruction results, we find that the mean CWsin varies in a range of 0.33 - 0.41 with an average of 0.36, and the average field divergence $|f|$ varies in between 0.00072 and 0.00091 with a mean value of 0.00082.

We acknowledge that there exist other parallel NLFFF codes that have been broadly used or evaluated by solar physics researchers (e.g., Schrijver et al. 2006; Metcalf et al. 2008; Schrijver et al. 2008; DeRosa et al. 2009). Given the limitation

of both the NLFFF algorithm and the vector magnetic field measurements, the reconstruction results should be assessed with caution.

BIBLIOGRAPHY

Ahmad, Q. R., Allen, R. C., Andersen, T. C., et al. 2001, Physical Review Letters, 87, 071301

Amari, T., Luciani, J. F., Aly, J. J., & Tagger, M. 1996, ApJ, 466, L39

Ambastha, A., Hagyard, M. J., & West, E. A. 1993, Sol. Phys., 148, 277

Antiochos, S. K., DeVore, C. R., & Klimchuk, J. A. 1999, ApJ, 510, 485

Anwar, B., Acton, L. W., Hudson, H. S., et al. 1993, Sol. Phys., 147, 287

Barnes, C. W., & Sturrock, P. A. 1972, ApJ, 174, 659

Beauregard, L., Verma, M., & Denker, C. 2012, Astronomische Nachrichten, 333, 125

Bonanno, A., Schlattl, H., & Paternò, L. 2002, A&A, 390, 1115

Borrero, J. M., Tomczyk, S., Kubo, M., et al. 2011, Sol. Phys., 273, 267

Brickhouse, N. S., & Labonte, B. J. 1988, Sol. Phys., 115, 43

Brown, D. S., Nightingale, R. W., Alexander, D., et al. 2003, Sol. Phys., 216, 79

Brueckner, G. E., Howard, R. A., Koomen, M. J., et al. 1995, Sol. Phys., 162, 357

Burtseva, O., & Petrie, G. 2013, Sol. Phys., 283, 429

Calabretta, M. R., & Greisen, E. W. 2002, A&A, 395, 1077

Cao, W., Gorceix, N., Coulter, R., et al. 2010, Astronomische Nachrichten, 331, 636

Carley, E. P., McAteer, R. T. J., & Gallagher, P. T. 2012, ApJ, 752, 36

Chen, J., Wang, H., Zirin, H., & Ai, G. 1994, Sol. Phys., 154, 261

Chen, W.-Z., Liu, C., Song, H., et al. 2007, Chinese J. Astron. Astrophys., 7, 733

Deng, N., Liu, C., Yang, G., Wang, H., & Denker, C. 2005, ApJ, 623, 1195

Deng, N., Tritschler, A., Jing, J., et al. 2013, ApJ, 769, 112

Ding, Y. J., Wang, H. Z., & Hong, Q. F. 1981, Acta Astrophysica Sinica, 1, 264

Ding, Y.-j., Zhang, B.-r., Li, W.-b., Hong, Q.-f., & Li, Z.-k. 1977, Chinese Astronomy, 1, 131

Donea, A., & Lindsey, C. 2012, in American Astronomical Society Meeting Abstracts, Vol. 220, American Astronomical Society Meeting Abstracts #220, #516.03

Emilio, M., Kuhn, J. R., Bush, R. I., & Scholl, I. F. 2012, ApJ, 750, 135

Evershed, J. 1910, MNRAS, 70, 217

Fan, Y. 2009, ApJ, 697, 1529

Feng, L., Wiegelmann, T., Su, Y., et al. 2013, ApJ, 765, 37

Fisher, G. H., Bercik, D. J., Welsch, B. T., & Hudson, H. S. 2012, Sol. Phys., 277, 59

Fisher, G. H., & Welsch, B. T. 2008, in Astronomical Society of the Pacific Conference Series, Vol. 383, Subsurface and Atmospheric Influences on Solar Activity, ed. R. Howe, R. W. Komm, K. S. Balasubramaniam, & G. J. D. Petrie, 373

Forbes, T. G. 2000, J. Geophys. Res., 105, 23153

Gary, G. A., & Hagyard, M. J. 1990, Sol. Phys., 126, 21

Goode, P. R., Yurchyshyn, V., Cao, W., et al. 2010, ApJ, 714, L31

Green, L. M., Kliem, B., & Wallace, A. J. 2011, A&A, 526, A2

Hagenaar, H. J., & Shine, R. A. 2005, ApJ, 635, 659

Hagyard, M. J., Stark, B. A., & Venkatakrishnan, P. 1999, Sol. Phys., 184, 133

Hale, G. E., Ellerman, F., Nicholson, S. B., & Joy, A. H. 1919, ApJ, 49, 153

Harvey, K. L., & Harvey, J. W. 1976, Sol. Phys., 47, 233

Howard, R. A., Moses, J. D., Vourlidas, A., et al. 2008, Space Sci. Rev., 136, 67

Hudson, H. S. 2000, ApJ, 531, L75

—. 2011, Space Sci. Rev., 158, 5

Hudson, H. S., Fisher, G. H., & Welsch, B. T. 2008, in Astronomical Society of the Pacific Conference Series, Vol. 383, Subsurface and Atmospheric Influences on Solar Activity, ed. R. Howe, R. W. Komm, K. S. Balasubramaniam, & G. J. D. Petrie, 221

Hudson, H. S., Fletcher, L., Fisher, G. H., Abbett, W. P., & Russell, A. 2012, Sol. Phys., 277, 77

Hurford, G. J., Schmahl, E. J., Schwartz, R. A., et al. 2002, Sol. Phys., 210, 61

Inoue, S., Hayashi, K., Magara, T., Choe, G. S., & Park, Y. D. 2014, ApJ, 788, 182

Ji, H., Wang, H., Liu, C., & Dennis, B. R. 2008, ApJ, 680, 734

Jiang, C., & Feng, X. 2013, ApJ, 769, 144

Jiang, C., Feng, X., Wu, S. T., & Hu, Q. 2013, ApJ, 771, L30

Jiang, C., Wu, S. T., Feng, X., & Hu, Q. 2014, ApJ, 780, 55

Jiang, Y., Zheng, R., Yang, J., et al. 2012, ApJ, 744, 50

Jing, J., Wiegelmann, T., Suematsu, Y., Kubo, M., & Wang, H. 2008, ApJ, 676, L81

Kazachenko, M. D., Canfield, R. C., Longcope, D. W., et al. 2009, ApJ, 704, 1146

Kopp, R. A., & Pneuman, G. W. 1976, Sol. Phys., 50, 85

Kosovichev, A. G., & Zharkova, V. V. 2001, ApJ, 550, L105

Kosugi, T., Matsuzaki, K., Sakao, T., et al. 2007, Sol. Phys., 243, 3

Leka, K. D., Barnes, G., Crouch, A. D., et al. 2009, Sol. Phys., 260, 83

Lemen, J. R., Title, A. M., Akin, D. J., et al. 2012, Sol. Phys., 275, 17

Li, H., Sakurai, T., Ichimoto, K., & UeNo, S. 2000a, PASJ, 52, 465

—. 2000b, PASJ, 52, 483

Li, Y., Jing, J., Fan, Y., & Wang, H. 2011, ApJ, 727, L19

Li, Y., Jing, J., Tan, C., & Wang, H. 2009, Science in China: Physics, Mechanics and Astronomy, 52, 1702

Lin, R. P., Dennis, B. R., Hurford, G. J., et al. 2002, Sol. Phys., 210, 3

Liu, C., Deng, N., Lee, J., et al. 2013a, ApJ, 778, L36

Liu, C., Deng, N., Liu, R., et al. 2011, ApJ, 735, L18

Liu, C., Deng, N., Liu, Y., et al. 2005, ApJ, 622, 722

Liu, C., Xu, Y., Deng, N., et al. 2013b, ApJ, 774, 60

Liu, C., Deng, N., Liu, R., et al. 2012, ApJ, 745, L4

Liu, Y., Zhao, J., & Schuck, P. W. 2013c, Sol. Phys., 287, 279

Lodders, K. 2003, ApJ, 591, 1220

Low, B. C. 2001, J. Geophys. Res., 106, 25141

Lynch, B. J., Antiochos, S. K., MacNeice, P. J., Zurbuchen, T. H., & Fisk, L. A. 2004, ApJ, 617, 589

Martres, M. J., Rayrole, J., Semel, M., et al. 1982, PASJ, 34, 299

Martres, M.-J., Soru-Escaut, I., & Rayrole, J. 1973, Sol. Phys., 32, 365

Masson, S., Pariat, E., Aulanier, G., & Schrijver, C. J. 2009, ApJ, 700, 559

McClymont, A. N., & Fisher, G. H. 1989, Washington DC American Geophysical Union Geophysical Monograph Series, 54, 219

Melrose, D. B. 1997, ApJ, 486, 521

—. 2012, ApJ, 749, 59

Metcalf, T. R. 1994, Sol. Phys., 155, 235

Moore, R. L., Larosa, T. N., & Orwig, L. E. 1995, ApJ, 438, 985

Moore, R. L., & Sterling, A. C. 2006, Washington DC American Geophysical Union Geophysical Monograph Series, 165, 43

Moore, R. L., Sterling, A. C., Hudson, H. S., & Lemen, J. R. 2001, ApJ, 552, 833

Patterson, A., & Zirin, H. 1981, ApJ, 243, L99

Petrie, G. J. D. 2013, Sol. Phys., 287, 415

Petrie, G. J. D., & Sudol, J. J. 2010, ApJ, 724, 1218

Priest, E. R., & Forbes, T. G. 2002, A&A Rev., 10, 313

Qiu, J., & Gary, D. E. 2003, ApJ, 599, 615

Régnier, S., & Canfield, R. C. 2006, A&A, 451, 319

Reid, H. A. S., Vilmer, N., Aulanier, G., & Pariat, E. 2012, A&A, 547, A52

Ribas, I., Porto de Mello, G. F., Ferreira, L. D., et al. 2010, ApJ, 714, 384

Schou, J., Scherrer, P. H., Bush, R. I., et al. 2012, Sol. Phys., 275, 229

Schrijver, C. J., Aulanier, G., Title, A. M., Pariat, E., & Delannée, C. 2011, ApJ, 738, 167

Schuck, P. W. 2006, ApJ, 646, 1358

—. 2008, ApJ, 683, 1134

Spirock, T. J., Yurchyshyn, V. B., & Wang, H. 2002, ApJ, 572, 1072

Stenflo, J. O. 1969, Sol. Phys., 8, 115

Sterling, A. C., & Moore, R. L. 2004, ApJ, 602, 1024

Su, J., Liu, Y., Zhang, H., et al. 2010, ApJ, 710, 170

Sudol, J. J., & Harvey, J. W. 2005, ApJ, 635, 647

Sun, X., Hoeksema, J. T., Liu, Y., et al. 2012, ApJ, 748, 77

Tan, C., Chen, P. F., Abramenko, V., & Wang, H. 2009, ApJ, 690, 1820

Temmer, M., Veronig, A. M., Vršnak, B., et al. 2008, ApJ, 673, L95

Thompson, W. T. 2006, A&A, 449, 791

Tokman, M., & Bellan, P. M. 2002, ApJ, 567, 1202

Török, T., & Kliem, B. 2003, A&A, 406, 1043

Török, T., Temmer, M., Valori, G., et al. 2013, Sol. Phys., 286, 453

Tsuneta, S., Ichimoto, K., Katsukawa, Y., et al. 2008, Sol. Phys., 249, 167

Vemareddy, P., Ambastha, A., & Maurya, R. A. 2012, ApJ, 761, 60

Vourlidas, A., Buzasi, D., Howard, R. A., & Esfandiari, E. 2002, in ESA Special Publication, Vol. 506, Solar Variability: From Core to Outer Frontiers, ed. A. Wilson, 91–94

Vourlidas, A., Howard, R. A., Esfandiari, E., et al. 2010, ApJ, 722, 1522

Wang, H. 1992, Sol. Phys., 140, 85

—. 2006, ApJ, 649, 490

Wang, H., Deng, N., & Liu, C. 2012a, ApJ, 748, 76

Wang, H., Ewell, Jr., M. W., Zirin, H., & Ai, G. 1994, ApJ, 424, 436

Wang, H., & Liu, C. 2010, ApJ, 716, L195

—. 2012, ApJ, 760, 101

Wang, H., Liu, C., Deng, Y., & Zhang, H. 2005, ApJ, 627, 1031

Wang, H., Liu, C., Jing, J., & Yurchyshyn, V. 2007, ApJ, 671, 973

Wang, H., Liu, C., Qiu, J., et al. 2004a, ApJ, 601, L195

Wang, H., Liu, C., Wang, S., et al. 2013, ApJ, 774, L24

Wang, H., Qiu, J., Jing, J., et al. 2004b, ApJ, 605, 931

Wang, H., Spirock, T. J., Qiu, J., et al. 2002, ApJ, 576, 497

Wang, S., Liu, C., Liu, R., et al. 2012b, ApJ, 745, L17

Wang, S., Liu, C., & Wang, H. 2012c, ApJ, 757, L5

Webb, D. F., & Howard, T. A. 2012, Living Reviews in Solar Physics, 9, 3

Welsch, B. T., Fisher, G. H., Abbett, W. P., & Regnier, S. 2004, ApJ, 610, 1148

Wiegelmann, T. 2004, Sol. Phys., 219, 87

Wiegelmann, T., Inhester, B., & Sakurai, T. 2006, Sol. Phys., 233, 215

Yan, X. L., & Qu, Z. Q. 2007, A&A, 468, 1083

Yan, X.-L., Qu, Z.-Q., & Kong, D.-F. 2008a, MNRAS, 391, 1887

Yan, X. L., Qu, Z. Q., & Xu, C. L. 2008b, ApJ, 682, L65

Yan, X.-L., Qu, Z.-Q., Xu, C.-L., Xue, Z.-K., & Kong, D.-F. 2009, Research in Astronomy and Astrophysics, 9, 596

Yang, G., Xu, Y., Cao, W., et al. 2004, ApJ, 617, L151

Yurchyshyn, V., Wang, H., Abramenko, V., Spirock, T. J., & Krucker, S. 2004, ApJ, 605, 546

Zhang, J., & Dere, K. P. 2006, ApJ, 649, 1100

Zhang, J., Dere, K. P., Howard, R. A., & Vourlidas, A. 2004, ApJ, 604, 420

Zhang, J., Li, L., & Song, Q. 2007, ApJ, 662, L35

Zhang, Y., Liu, J., & Zhang, H. 2008, Sol. Phys., 247, 39

Zharkov, S., Green, L. M., Matthews, S. A., & Zharkova, V. V. 2011, ApJ, 741, L35

—. 2013, Sol. Phys., 284, 315